Impulsive Interactions of Half Cycle Pulse Radiation with Rydberg Atoms

Impulsive Interactions of Half Cycle Pulse Radiation with Rydberg Atoms

EEN WETENSCHAPPELIJKE PROEVE OP HET GEBIED VAN
DE NATUURWETENSCHAPPEN, WISKUNDE EN INFORMATICA

PROEFSCHRIFT

Ter verkrijging van de graad van doctor
aan de katholieke universiteit van Nijmegen
op gezag van de Rector Magnificus Prof. dr. C.W.P.M. Blom,
volgens besluit van het College van Decanen
in het openbaar te verdedigen op dinsdag 1 juli 2003
des morgens om 10.30 uur precies
door

Anouk Agnes Renier Wetzels

geboren op 11 oktober 1975
te Sittard

Promotiecommissie

Promotor:	Prof. Dr. W.J. van der Zande
Manuscript Commissie:	Dr. W.L. Meerts Prof. Dr. F. Robicheaux, Auburn University Dr. P.C.M. Planken, Technische Universiteit Delft

ISBN: 90-9016831-1
NUR: 926

The experiments described in this thesis were performed at the following institutes:

FOM Institute for Atomic and Molecular Physics
Kruislaan 407
1098 SJ Amsterdam, The Netherlands
http://www.amolf.nl

FOM Institute for Plasma Physics
Edisonbaan 14
3439 MN Nieuwegein, The Netherlands
http://www.rijnh.nl

This work is part of the research program of the Stichting voor Fundamenteel Onderzoek der Materie (Foundation for Fundamental Research on Matter) and was made possible by financial support from the Nederlandse Organisatie voor Wetenschappelijk Onderzoek (Netherlands Organization for the Advancement of Research).

This thesis is based on the following publications:

Chapter 2	*Reduction of electronic noise in THz generation* A. Wetzels, A. Gürtler, A. Buijserd, T. Vijftigschild, H. ter Horst, W.J. van der Zande Rev. Sci. Inst. **74**, (2003)
Chapter 3	*The dynamics of a THz wavepacket* A. Wetzels, A. Gürtler, H.G. Muller, L.D. Noordam Eur. Phys. J. D. **14**, 157 (2001)
Chapter 4	*Rydberg State Ionization by Half-Cycle Pulse Excitation: Strong Kicks Create Slow Electrons* A. Wetzels, A. Gürtler, L.D. Noordam, F. Robicheaux, C. Dinu, H.G. Muller, M.J.J. Vrakking, W.J. van der Zande Phys. Rev. Lett. **89**, 273003 (2002) Virtual Journal of Ultrafast Science **2**, (2003)
Chapter 5	*Two-Dimensional Momentum Imaging of Rydberg States using Half-Cycle Pulse Ionization and Velocity-Map Imaging* A. Wetzels, A. Gürtler, F. Roşca-Prună, S. Zamith, M.J.J. Vrakking, F. Robicheaux, W.J. van der Zande submitted to PRL *Characteristics of Half-Cycle-Pulse Ionization of Rydberg States using Velocity Map Imaging* A. Wetzels, A. Gürtler, F. Roşca-Prună, S. Zamith, C. Dinu, M.J.J. Vrakking, H.G. Muller, F. Robicheaux, W.J. van der Zande submitted to PRA

Contents

1 Introduction to Rydberg Atoms and Half-Cycle Pulses 9
  1.1 Impulsive Interaction between Half-Cycle Pulse and Rydberg Atom . . 10
    1.1.1 Interaction between Radiation and Matter: ‘Photon’ Picture versus Impulsive Kick 10
    1.1.2 Few-Cycle Radiation 12
    1.1.3 Creating and Manipulating Wavepackets with Half-Cycle Pulses 13
    1.1.4 Momentum Distribution of Electrons Ionized with Half-Cycle Pulses 15
  1.2 Rydberg Atoms 16
    1.2.1 Rydberg Atoms in an Electric Field 19
    1.2.2 State-Selective Field Ionization 24
    1.2.3 Wavepackets 24
  1.3 Half-Cycle Pulses 26
    1.3.1 Impulsive approximation 27
    1.3.2 Limits of the Impulsive Regime 29
    1.3.3 Momentum Retrieval 30
    1.3.4 Velocity Imaging Detector 31

2 Aspects of Picosecond THz Generation and Detection 33
  2.1 Introduction 34
  2.2 Half-Cycle Pulse 34
    2.2.1 Introduction 34
    2.2.2 Generation of Half-Cycle Pulses 35
    2.2.3 Detection of Half-Cycle Pulse 37
    2.2.4 Results 39
  2.3 Reduction of Electronic Noise in THz Generation 41
  2.4 Few Cycle Radiation 44
    2.4.1 Introduction 44
    2.4.2 Generation of few cycle radiation: ‘Pulse slicing’ 44
    2.4.3 Experimental Setup 46

2.4.4 Detection of few cycle radiation 49
2.4.5 Results and Discussion 53

3 The Dynamics of a THz Rydberg Wavepacket 63
3.1 Introduction 64
3.2 Experimental Setup 67
3.3 Results and Discussion 70
3.3.1 Experimental Results 70
3.3.2 Theoretical Description 72
3.4 Semi-Classical Interpretation 75
3.4.1 Semi-Classical Picture 75
3.4.2 Calculation 77
3.5 Summary 79

4 Rydberg State Ionization by Half-Cycle Pulse Excitation: Strong Kicks Create Slow Electrons 83
4.1 Introduction 84
4.2 Experimental Method and Theoretical Description 85
4.2.1 Experimental Setup 85
4.2.2 Classical Calculations 87
4.3 Results 87
4.4 Summary 91

5 Two-Dimensional Momentum Imaging of Rydberg States Using Half-Cycle Pulse Ionization and Velocity-Map Imaging 93
5.1 Introduction 94
5.2 Experimental Setup and Rydberg state properties 96
5.3 Classical and Quantum Mechanical Calculations 98
5.4 Results 101
5.5 Discussion and Conclusion 107

Bibliography 111

Summary 117

Samenvatting 121

Acknowledgment 125

Curriculum Vitae 127

Chapter 1

Introduction to Rydberg Atoms and Half-Cycle Pulses

The main subject of this thesis is the interaction of ultrashort electromagnetic radiation and Rydberg atoms to investigate the boundaries of the interaction between light and matter. In contrast with the commonly used 'photon picture' of light, the interaction of short electromagnetic radiation in the form of a single half cycle with a Rydberg atom, an atom with the outer electron in a highly excited state, can be described as an impulsive kick. The electric field strength, and not the photon energy, is very important here. In the first part of this chapter our experiments are described and compared with the current status of atomic physics. In the remainder of this chapter an introduction to Rydberg atoms and half-cycle pulses is given.

1.1 Impulsive Interaction between Half-Cycle Pulse and Rydberg Atom

1.1.1 Interaction between Radiation and Matter: 'Photon' Picture versus Impulsive Kick

The interaction between electromagnetic radiation and matter dominates most of the processes that surround us, and has concerned physicists for many centuries. Maxwell's equations (1873) give rise to the phenomenon of electromagnetic waves in empty space [1]. James Clerk Maxwell found that electromagnetic waves consist of dynamic electric and magnetic fields that mutually induce each other and form self-supporting electromagnetic oscillations, which propagate with the speed of light. The works of Max Planck and Albert Einstein introduced the quantum notion in physics. In 1905, Albert Einstein proposed that electromagnetic radiation consists of particle-like packets of energy, each carrying a quantum of energy related to the frequency of the radiation. The particle-like energy packets in light are called photons. Nowadays it is accepted that light has both wave properties and particle properties. Interference and diffraction of light establish the wave properties of light, whereas, for example, the Compton effect reveals the particle properties of light. Also in the beginning of the twentieth century the quantum nature entered in our description of the behavior of material particles. In 1913, Niels Bohr made the radical proposal that at the atomic level the laws of classical mechanics must be replaced or supplemented by other laws. Niels Bohr expressed these new laws in the form of several postulates:

1) The orbits and the energies of the electrons in an atom are quantized, only certain discrete orbits and energies are permitted. The permitted orbits are characterized by quantized values of the orbital angular momentum L. This angular momentum is always an integral multiple of $h/2\pi$. The electron does not radiate continuously in a classical manner.

2) When an electron is in one of the quantized orbits, i.e. the electron is in a stationary state, it does not emit any electromagnetic radiation;

3) Electrons can make discontinuous transitions from one stationary state to another and the excess energy ΔE is released or absorbed as a single photon of frequency, where h is Planck's constant

$$\nu = \Delta E/h. \tag{1.1}$$

The 'photon picture' is most commonly used when discussing the interaction between electromagnetic radiation and matter. This thesis deals with radiation for which an interaction with matter in terms of photons does not provide a very useful description. Our model matter is the Rydberg atom and the radiation is an ultra-short half-cycle pulse. The characteristic feature of a Rydberg atom is that at least

Table 1.1: Properties of a Rydberg atom

Property	n dependence	example: $n = 40$
Binding energy	n^{-2}	8.5 meV
Classical roundtrip time	n^{3}	9.7 ps
Orbital radius	n^{2}	0.085 μm
Radiative lifetime	n^{3}	64 μs
Field ionization	n^{-4}	126 Vcm^{-1}

one electron of the atom is loosely bound in a highly excited state. Some properties of a Rydberg atom are shown in Table 1.1, where n is the principal quantum number (see section 1.2). The weak interaction of the excited electron with its parent ion makes the Rydberg atom an excellent playground for experiments. Due to the large average distance between the Rydberg electron and the nucleus, electrons are sensitive to small laboratory fields, which allows us to manipulate the dynamics of Rydberg electrons significantly. On the other hand, Rydberg atoms are remarkably stable against radiative decay but are unstable to absorption of blackbody radiation. The number of experimental studies of atoms in these states had a large increase in the 1970s with the advances in laser technology, especially with the development of the tunable dye laser [2]. With the tunable dye laser it became possible to excite large numbers of atoms to a single, well defined Rydberg state. In the interaction between these long, low intensity, pulses of electromagnetic radiation with matter the frequency ν of the radiation field, i.e. the photon energy, is considered to be crucial. The energy absorbed during the interaction is given by the photon energy

$$\Delta E = h\nu. \tag{1.2}$$

In our experiment the electric field oscillation of the radiation consists of half a cycle and the duration of the pulse is much shorter than one classical electron orbit time. The bandwidth of the pulse ($\sim$ 15 cm^{-1}) is relatively large compared with the mean energy ($\sim$ 33 cm^{-1}). As a consequence, the description of the interaction in terms of photons is not very appropriate, rather it is more like an impulsive interaction. The energy transfer does not depend on the photon energy but on the strength and direction of the kick, which is determined by the strength and direction of the electric field of the half-cycle pulse. This impulsive character often makes a classical description possible of the interaction of a half-cycle pulse with an electron. The effect of this kick can be calculated by Newton's laws, inserting a classical force

$$F(t) = qE(t), \tag{1.3}$$

where $E(t)$ is the temporal electric field of the half-cycle pulse.

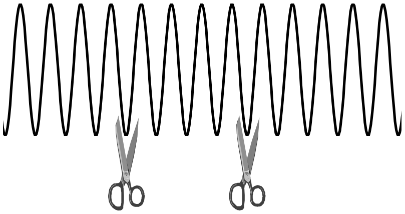

Figure 1.1: *A few cycle pulse is generated by cutting the front and back part out of a many-cycle pulse.*

1.1.2 Few-Cycle Radiation

As mentioned before in the process of photoionization of gas-phase atoms or molecules with long, low intensity, pulses of electromagnetic radiation, the frequency ν of the applied radiation field is considered to be crucial. If we define the radiation field as

$$E(t) = E_0(t)\cos(2\pi\nu t), \tag{1.4}$$

where $E_0(t)$ is a slowly varying envelope, photoionization will only occur when the photon energy ($h\nu$) exceeds the electron binding energy. The rate of ionization is then given by Fermi's Golden rule and proportional to the radiation intensity and thus to $|E_0(t)|^2$.[1] A tremendous amount of experiments in the last century has verified that Fermi's Golden Rule is applicable for long, low intensity, pulses of electromagnetic radiation, i.e. with many cycles ($2\pi\nu t$) of the radiation field during the pulse. Very short, intense, pulses can be made in which the radiation field makes essentially only half a cycle. In that case ionization depends on the amplitude $E_0(t)$ of the field rather than the frequency of the half-cycle pulse. The ionization probability is essentially zero for low field and increases rapidly when the field of the half-cycle pulse exceeds a critical value $E_{ionization}$. The ionization curve has an s-like shape. The field required to obtain substantial ionization by such short pulses is very high. For these strong fields, pertubation theory no longer applies and hence Fermi's Golden Rule fails. In fact for ionization by half-cycle pulses Einstein's frequency condition

$$h\nu > E_{binding} \tag{1.5}$$

does not need to be fulfilled. The ionization behavior in the regime between 'many-cycle' optical pulse ionization and half-cycle pulse ionization would be interesting to investigate. In this thesis, a report is given of a technique to bridge the gap between many-cycle optical pulse to a single half-cycle pulse, using an ultra fast switchable

---

[1] In this comparison we do not take into account the possibility of a coherent interaction leading to Rabi oscillations.

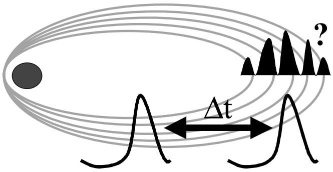

Figure 1.2: *The wavepacket, generated by exciting a stationary Rydberg state with a weak half-cycle pulse, is manipulated by a second, time-delayed weak half-cycle pulse. The half-cycle pulses are so weak as to remain in the pertubative regime and only neighbouring states of the initial Rydberg state are populated. We were interested in the final population distribution over the eigenstates of the wavepacket after the interaction of the two half-cycle pulses. The population depended on the time delay between the two half-cycle pulses.*

mirror to slice many-cycle light from a free electron laser (Fig. 1.1). This technique has been mostly used in the near infrared regime. We wanted to try this technique in the far infrared regime, the THz regime. The results are not yet definitive but promising. A detailed description of the generation methods for half-cycle pulses and few-cycle radiation in the THz regime is given in Chapter 2. Generation of half-cycle pulses involves strong electronic noise. We found a method to reduce this electronic noise significantly by mounting an RC circuit over the wafer, also described in Chapter 2. The temporal shape of the electric field of the half-cycle pulse is often measured with an electro-optical sampling technique. A single shot setup of this electro-optical sampling technique was used to detect the temporal shape of the few-cycle pulse.

1.1.3 Creating and Manipulating Wavepackets with Half-Cycle Pulses

In the 1920s Bohr's semiclassical theory was replaced by quantum mechanics by Erwin Schrödinger [3] and Werner Heisenberg. The basis for the development of the quantum theory was laid by de Broglie's hypothesis that electrons do not have only particle properties but also wave properties. The wave properties are described by a wave equation, the Schrödinger equation

$$\hbar \frac{\partial}{\partial t}\Psi(t) = -iH\Psi(t). \tag{1.6}$$

The solutions of the time independent Schrödinger equation

$$H\psi(\mathbf{r}) = E\psi(\mathbf{r}) \tag{1.7}$$

are stationary with a fixed energy, which implies that they are energy eigenfunctions of the Hamiltonian operator. The total solution then is

$$\Psi(\mathbf{r}, t) = \psi(\mathbf{r}) e^{-iEt/\hbar}. \tag{1.8}$$

The amplitude of the eigenfunction at some point determines the probability that there is an electron particle at that point. Ever since the development of quantum mechanics and the notion of the wavefunction, its relation with classical mechanics has been a subject of interest. It was clear from the start of quantum mechanics that at some point the quantum and classical description approach each other, formulated in the correspondence principle. Somewhere in the 1930, the notion dawned that atoms do not necessarily exist in stationary eigenstates. It was realized that a coherent superposition of eigenstates could be formed, which describes the time dependent behavior of certain observables of a particle. This provides a bridge between quantum and classical mechanics. Today, thanks to the development of ultrafast lasers, even the time dependence of electrons in their orbit has been observed by coherently exciting Rydberg eigenstates using ultrashort laser pulses in which the bandwidth exceeds the level spacing in the final Rydberg manifold [4, 5]. In most experiments a many-cycle short optical pulse is used to create a wavepacket in a Rydberg atom [6, 7]. The large bandwidth of this short pulses makes coherent excitation of several eigenstates possible. Optical pulses interact with the electron when the electron is near the core, as in other parts of the orbit the energy transfer is equal to zero. Therefore the wavepacket is initially strongly localized. An alternative approach to generate Rydberg wavepackets is excitation with a half-cycle pulse [8–10]. In Chapter 3 we will show that a wavepacket created by a half-cycle pulse is initially delocalized, because a half-cycle pulse can interact with an electron over the whole orbit. A half-cycle pulse can be used also to manipulate wavepackets in a Rydberg atom. Dunning and coworkers [11, 12] investigated the behavior of a Rydberg atom subjected to a train of up to 50 equally spaced unidirectional half-cycle pulses. The survival probability has a maximum at pulse repetition frequencies near the classical orbit roundtrip time. Each time that the electron arrives near the core, its velocity is turned by the half-cycle pulse kick, but no energy is added. In Chapter 3 a wavepacket is generated by exciting a stationary Rydberg state with a weak half-cycle pulse. We are still in the pertubative regime and only neighbouring states of the initial Rydberg state are excited. The wavepacket evolves in time. Initially the wavepacket is delocalized and becomes localized after half a revival time. A second weak half-cycle pulse will interact with the wavepacket and change the population distribution over its eigenstates. The final population in each eigenstate varies as the time delay between the half-cycle pulses is changed. The population in each eigenstate after the interaction with two half-cycle pulses is measured as a function of the delay between the two half-cycle pulses. In Fig. 1.2 an illustration of the experiment is shown. The population change as a function of the time delay between the two half-cycle pulses can be understood with a classical picture. We support our experimental data with quantum mechanical

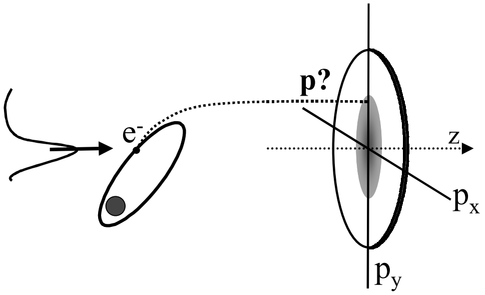

Figure 1.3: *Illustration of the experiments performed in Chapters 4 and 5. An electron in a Rydberg state is ionized with a half-cycle pulse. The momentum of the ejected electron is measured with a velocity imaging detector.*

calculations.

1.1.4 Momentum Distribution of Electrons Ionized with Half-Cycle Pulses

In Chapters 4 and 5 a velocity imaging technique [5] is used to measure the momentum distribution of electrons ionized by a half-cycle pulse, see Fig. 1.3. In velocity imaging all particles with the same velocity vector after ejection are mapped onto the same point on the detector. In Chapter 4 the influence of the 'tail' of the half-cycle pulse is discussed. The exact shape of the half-cycle pulse is a strong, short half cycle followed by a weak, long half-cycle with opposite polarity (the tail) due to diffraction of the low frequency components. The total area of the pulse is zero. Often the tail is ignored, because its time duration is longer than the roundtrip time of the electron and has therefore no influence on a bound electron. Only Tielking *et al.* [13] and Wesdorp *et al.* [14] studied the effect on the half-cycle pulse ionization on Rydberg atoms. We will show that the tail of the half-cycle pulse has no influence on the ionization efficiency of a Rydberg atom in the limit that the main half-cycle pulse is short compared to the orbit time of the electron (between $n = 25$ and $n = 50$). However the tail of the half-cycle pulse has a large influence on the final momentum distribution of the ejected electrons. Measured momentum images together with semi-classical calculations showed that the tail takes away nearly all of the energy that the electron gains by the interaction with the main half-cycle pulse.

A very interesting technique would be to detect directly the momentum distribution of a Rydberg state. Jones [9,15] developed a technique to measure indirectly the momentum distribution of a Rydberg state in the direction of a half-cycle pulse kick.

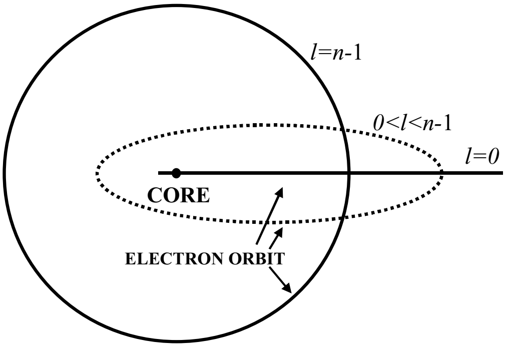

Figure 1.4: *Drawing of the electron orbit for different angular momenta, respectively maximum* $l = n - 1$*, minimum* $l = 0$ *and an intermediate* l *state. When* $l = 0$ *the orbit has a 'cigar'-like shape and when* $l = n - 1$ *the orbit is circular. The size of the major axis is determined by the principal quantum number* n *and scales as* n^2*.*

The derivative of the ionization curve as a function of the kick strength gives the initial momentum distribution of the Rydberg state. In our method we use the property of a half-cycle pulse that it only changes the momentum of the electron in the polarization direction of the half-cycle pulse. By kicking the electron towards the detector of our velocity-imaging detector, the initial momenta of the electron perpendicular to the detector are not changed and the momentum distribution of the initial Rydberg state is measured. We will illustrate the potential of half-cycle pulse ionization as a direct method for looking at wavefunctions by empirically comparing the measured momentum images obtained with different half-cycle pulse polarizations. Theoretical support is obtained by the use of classical trajectory simulations of our Rydberg state and of the half-cycle ionization process.

1.2 Rydberg Atoms

A comprehensive overview of experimental and theoretical studies of Rydberg atoms has been given by [16] and [17]. Hydrogen is, as a one electron atom, the 'most simple' Rydberg atom. Rydberg [18] found that the wavenumber k, given in cm^{-1}, of all the observed lines in the spectrum of atomic hydrogen can be represented up to high accuracy by

$$k = \frac{2\pi}{\lambda} = R(\frac{1}{n'^2} - \frac{1}{n^2}), \tag{1.9}$$

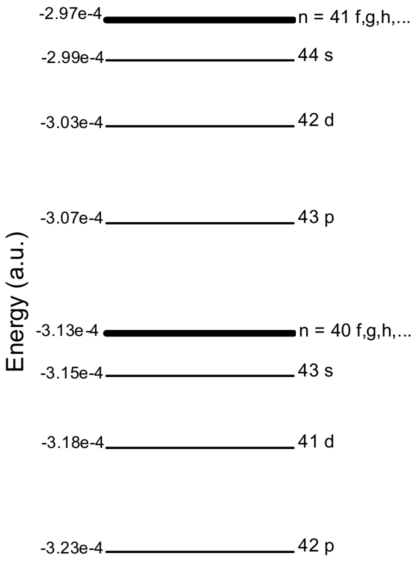

Figure 1.5: *Energy diagram of Rubidium around* $n = 40$*. The quantum defects of the* s*,* p *and* d *states are* $3.1, 2.7$ *and* 1.3, *respectively.*

with R called the Rydberg constant and n and n' ($n' > n$) are integers, which we now call the principal quantum numbers. Rydberg assigned R the value 109721.6 cm^{-1}. Since one can not measure energy levels in experiments but only transition energies between pairs of levels, the question of what state to use as zero energy is a matter of convention. Often the ionization threshold is chosen to have zero energy, in which case the binding energy is negative and a free electron has positive energy. The binding energy of the electron in a stationary orbit in hydrogen can be calculated by (atomic units are used unless stated otherwise)

$$E = -\frac{1}{2n^2}. \tag{1.10}$$

The principal quantum number n runs from 1 for the ground state to infinity for the ionic state. Quantum mechanics gives the most exact description of nature, but in the limiting case of large quantum numbers, the results obtained from quantum theory must agree with those obtained from classical theory. Most quantum numbers are related to a conserved quantity. In Rydberg atoms, the principal quantum number n determines the size of the electron orbit. The mean radius scales as n^2. The ellipticity of the orbit is a function of the angular momentum

$$\mathbf{l} = \mathbf{r} \times \mathbf{p}. \tag{1.11}$$

The angular momentum quantum number l runs from 0 to $n-1$. When $l=0$ the orbit is extremely elliptic. When $l=n-1$ the orbit is circular. See Fig. 1.4 where these two extreme orbits and an intermediate one are drawn. The energy levels with the same binding energy, i.e. with the same principal quantum number n, are n^2-fold degenerate in field free conditions. Both n and l are quantized. Finally there is one more quantum number m which is related to the projection of l on the quantization axes, for example the laser polarization direction or the direction of the electric field. The magnetic quantum number m runs from $-l$ to l in integer steps. Both the principal quantum number n and the magnetic quantum number m are conserved in a static electric field, whereas the angular quantum number l is only conserved in field free conditions.

Until now we have described only the situation for hydrogen, but many other atoms behave similarly when their outer electron is in a highly excited Rydberg state. The binding energy of these electrons is given by

$$E = -\frac{1}{2(n-\delta_l)^2}, \tag{1.12}$$

where δ is the quantum defect of the angular momentum state l. The quantum defect δ describes the energy shift of the excited state with respect to hydrogen. This energy shift is caused by the interaction of the excited electron with the nucleus and the other tightly bound core electrons. At small distance from the core, where the outer electron can penetrate the electron cloud around the core, the potential of a non-hydrogenic core is deeper than the Coulomb potential of a hydrogen core. This results in a more deeply bound energy. At a large distance from the ionic core the potential experienced by the outer electron is equal to the Coulomb potential. So at large distance the difference between a non-hydrogen atom and hydrogen are minimal and many properties at the outer turning point of the electron orbit of all Rydberg atoms are similar. The quantum defect depends on the specific atom and on the angular momentum. An electron in a state of high orbital angular momentum never comes close enough to the core to detect that the core is anything other than a point charge. In this case the quantum defect will be almost equal to zero. If the electron is in a highly elliptic low l orbit, the Rydberg electron comes on each roundtrip close to the core. The quantum defect will be large for low l states and will break the degeneracy of these low l states. In Fig 1.5 the energy diagram of Rubidium around $n=40$ is drawn, illustrating these effects for states with $l=0(s)$, $l=1(p)$ and $l=2(d)$.

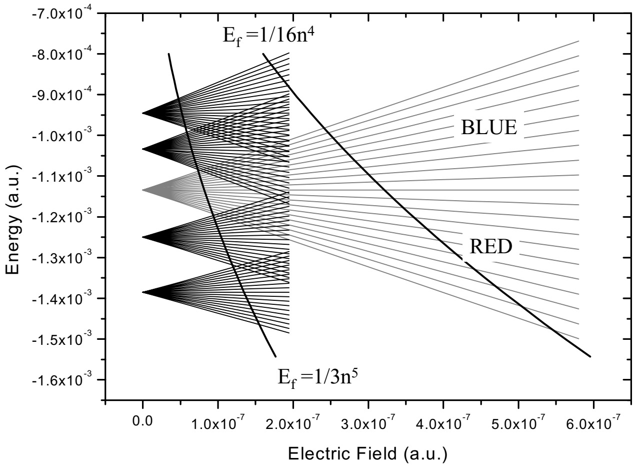

Figure 1.6: *Stark map of Hydrogen. The degenerate angular momentum states belonging to a certain n fan out with increasing field strength. Also the classical field ionization limit (thick solid line) and the start of the n-mixing regime (thin solid line) are included .*

1.2.1 Rydberg Atoms in an Electric Field

Rydberg states are highly susceptible to external electric fields since the electric field of the Coulomb potential is strongly reduced at large distances from the core. For highly excited Rydberg states an externally applied electric field can become comparable to the Coulomb field of the ionic core, allowing significant modification of the atomic potential. Relatively modest electric fields not only perturb the Rydberg energy levels, but can even ionize Rydberg atoms. In zero field, all the angular momentum states l (except the low l states in a non-hydrogenic atom), belonging to a state with a certain principal quantum number n are degenerate. When a Rydberg atom is placed in a static electric field F, the degeneracy of the angular momentum states is lifted. The angular momentum number is no longer a conserved quantity in the field. The degenerate angular momentum states belonging to a certain n fan out with increasing field strength. These non degenerate states are called Stark states and are labelled by the new quantum number k. In an electric field the quantity that k describes is the dipole moment of the state. The quantum number k ranges from $-n+1+|m|, ...n-1-|m|$ in steps of 2. The energy of the Stark states is given to

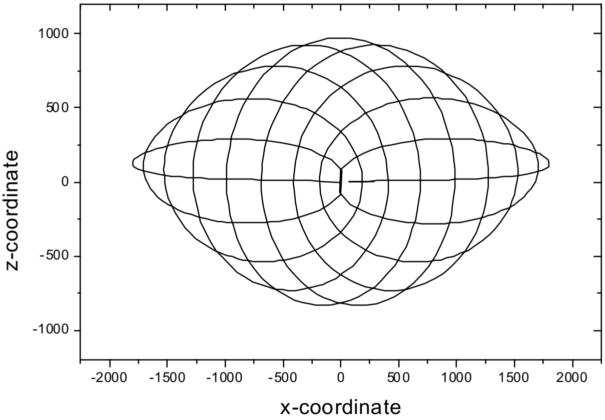

Figure 1.7: *Classical trajectory of an orbit in an electric field (z-direction). The angular momentum oscillates between l = 0 and l = n-1.*

first order by

$$E = -\frac{1}{2n^2} + \frac{3}{2}nkF. \tag{1.13}$$

From equation 1.13 we see that the energy of the Stark state depends linearly on the electric field strength. In Fig. 1.6 a Stark map of hydrogen is shown. The states increasing in energy as a function of the electric field ($k > 0$) are called "blue" states and the states decreasing in energy ($k < 0$), "red" states. At a certain electric field strength the Stark states of n and $n + 1$ start to cross. This n-mixing regime starts at

$$F = \frac{1}{3n^5}. \tag{1.14}$$

The Stark states are linear combinations of zero-field l states. Classically, the angular momentum l oscillates between $l = 0$ and $l = n - 1$. In Fig. 1.7 the classical trajectory is drawn for a state perpendicular to the electric field. In non-hydrogenic atoms low l states with a significant quantum defect do not immediately mix in with the other k states in the manifold. These low l states keep initially their l character until they mix in the manifold, then the l character is slowly spread over all k states. In non-hydrogenic atoms the blue and red Stark states of adjacent n do not cross as they do in hydrogen, but at the field where the energies of two levels are equal the degeneracy is lifted and the energy levels are split as a result of them being coupled. This avoided crossing is shown in Fig. 1.8. The coupling is due to the presence of the

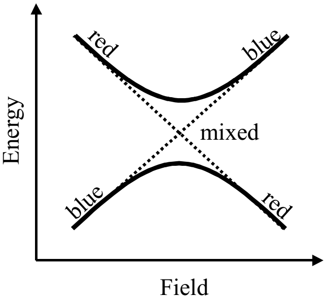

Figure 1.8: *The dotted lines illustrated the crossing of two hydrogen levels. The solid lines show the avoided crossing of two non-hydrogenic levels.*

inner electrons in the ion core, which change the potential from a pure Coulomb form. This change in potential from a pure Coulomb form cause the Runge-Lenz vector to precess. The Runge-Lenz vector is the classical representation of the orientation of the dipole moment. The Runge-Lenz vector lies along the major axis of the classical orbit. In a pure hydrogen atom the classical orbit does not precess, and the quantum eigenstates have permanent dipole moments. In non-hydrogenic atoms Rydberg states have elliptical orbits that can precess rapidly between the uphill to the downhill sides of the ion. The precession is not gradual or regular. During parts of the classical orbit when the angular momentum of the electron is large, the trajectory does not get near to the core electrons, and so there is essentially no precession. When the angular momentum is low, the trajectory may dive into the core and emerge in a different direction. This process is called core scattering.

When an atom is placed in a static electric field the potential experienced by a Rydberg electron is given by

$$V(r,z) = -\frac{1}{r} - Fz, \tag{1.15}$$

where F is the electric field strength in the -z direction. In the $+z$ direction the potential is lowered by the external electric field, giving rise to a local maximum, a saddle point in the potential surface at

$$z = \frac{1}{\sqrt{F}}. \tag{1.16}$$

In Fig. 1.9 an illustration is given of a Coulomb field with and without an external electric field. The blue Stark states are located on the ‘uphill’ side of the potential and the red Stark states correspond to states located on the ‘downhill’ side of the potential near the saddle point. In three dimensions the saddle point is a hole in the spherical Coulomb potential through which the electron can escape, which means that the electron can follow a fully classical allowed path to ionization. The size of this hole depends on the difference between the binding energy of the electron and the saddle point energy. The higher the excess energy of the electron above the saddle point energy, the larger the hole in the saddle point. The classical threshold energy above which the electron can escape over the saddle point of the potential is given by

$$E = -2\sqrt{F}. \tag{1.17}$$

Classical ionization occurs when the binding energy of a Rydberg electron exceeds this saddle point energy. The threshold field above which classical ionization is possible, is then given by

$$F = \frac{E^2}{4}. \tag{1.18}$$

If we ignore the Stark shift of a Rydberg state with principal quantum number n and write the binding energy in terms of n (see Eq. 1.10) we obtain the classical field for ionization in terms of principal quantum number,

$$F = \frac{1}{16n^4}. \tag{1.19}$$

The classical field ionization limit is included in Fig. 1.6. Equation 1.19 is only valid for $m = 0$ states. In higher m states there is a centrifugal potential keeping the electron away from the z axis, and the centrifugal barrier raises the threshold field. For $m \neq 0$ states the fractional increase in the field required for ionization, compared to an $m = 0$ state of the same energy, is

$$\frac{\Delta F}{F} = \frac{|m|}{2n}. \tag{1.20}$$

The classical picture outlined above ignores the Stark shifts and the spatial distribution. For the extreme red Stark state the Stark shift increases the binding energy,

$$E_b = -\frac{1}{2n^2} - \frac{3n^2F}{2}. \tag{1.21}$$

Using this energy we find a threshold field

$$F = \frac{1}{9n^4}. \tag{1.22}$$

The numerical factor of 1/9 instead of 1/16 is due to the Stark shift . The blue Stark states require higher fields to ionize than the red Stark states, because the electron in a blue Stark state is located on the side of the atom away from the saddle point in the

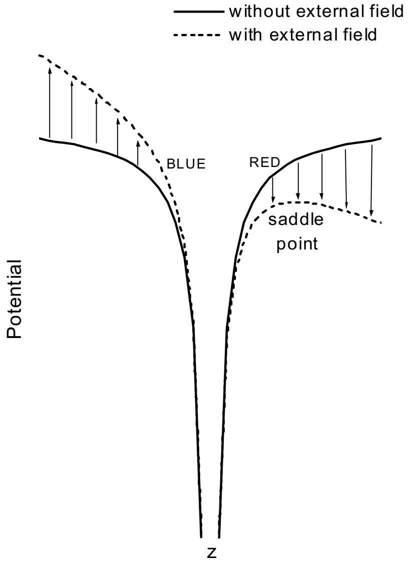

Figure 1.9: *Coulomb field with and without an external electric field. The electric field gives rise to a local maximum, a saddle point in the surface potential. Blue Stark states are located on the 'uphill' side of the potential and red Stark states on the 'downhill' side of the potential near the saddle point.*

potential, whereas the electron in a red Stark state is adjacent to the saddle point. For the blue states it is not possible to estimate simply the threshold field. However, blue and red Stark states of the same n often have threshold fields differing by a factor of 2. In a non-hydrogenic atom blue states ionize as well as red states at the classical ionization field, as they are coupled due to the presence of the core electrons. An electron in a blue orbit has a finite probability of being scattered from the stable blue orbit into the degenerate red continuum, when its angular momentum is low and the electron comes near the core. Above the classical ionization limit blue states, which would be perfectly stable in hydrogen, are coupled due to core scattering to degenerate red states, which are unbound, and ionization occurs rapidly. It can be viewed as an auto-ionization process, in which the blue Stark state is coupled to the red continuum state at the ionic core. However, Lankhuijzen *et al.* [19] observed long-lived states around the saddle point in Rubidium with lifetimes up to several microseconds. It appears in their experiment that for a non-hydrogenic Rydberg atom, where all the Stark states are strongly coupled, the character of the blue Stark states of hydrogen is still localized in a few Stark states. They observed that in a static electric field the blue Stark states just above the ionization threshold have lifetimes up to a few microseconds and that the red Stark states ionize directly after excitation. Just above the saddle point, the hole in the three dimensional Coulomb potential is very small, electrons in a blue Stark state will have small probabilities to scatter on the core in the direction of the saddle point. The higher the electron energy above the saddle point, the larger the hole in the Coulomb potential will be and the higher the probability that the electron initially was moving in the direction of the saddle point.

1.2.2 State-Selective Field Ionization

One method to ionize a Rydberg atom is photon excitation of the electron above the ionization threshold or saddle point. Another method is the application of an electric field. This electric field will lower the saddle point and the electron ionizes if its energy is above the saddle point energy. This latter method is a widely used tool to determine the population in specific Rydberg states. In this state-selective field ionization (SSFI) a field ramp is used with rise times of few hundred nanoseconds. Each state ionizes at a specific electric field and can therefore be distinguished from each other. In hydrogen, the Stark states of different manifolds do not couple, i.e. core scattering cannot take place. Therefore the Stark states cross diabatically, maintaining their blue or red character. A hydrogen atom in a specific Stark state remains in the same Stark state and ionization always occurs at the same field independent of the rise time. For the red Stark states the ionizing field is to a reasonable approximation near the classical field defined by Eq. 1.22. The fields for other Stark states are higher. Non hydrogenic atoms cross other Stark states adiabatically or diabatically depending on the rise time of the electric field ramp. In the case of a fast rising pulse the electron does not have time to couple to other Stark states via core scattering. The level crossings are diabatic, just like in hydrogen. In the case of a slowly rising field the level crossings are traversed adiabatically. Every time the electron comes near the core it can change its orbit orientation via core scattering and the electron can couple to other Stark states. At each avoided crossing the electron passes smoothly from one Stark state into another and remains in the same adiabatic energy level as the field increases. Finally, when the field reaches the classical ionization limit (Eq. 1.19), ionization occurs by coupling to the underlying red Stark continua.

1.2.3 Wavepackets

Wavepackets, i.e., quantum-mechanical states well localized in space, play a fundamental role in our concepts and understanding of quantum mechanics. They reflect the time evolution of a (localized) coherent superposition of a system, and thus provide the bridge between quantum mechanics and the classical concept of the trajectory (orbit) of a particle. Several theoretical and experimental articles have been written about wavepackets in Rydberg atoms [4, 5]. A localized wavepacket is formed by the coherent excitation of Rydberg states by a short, optical pulse. Coherent excitation can take place if the frequency bandwidth of the exciting pulse is larger than the spacing between the eigenstates. When several n states are coherently excited a radial wavepacket is formed [7] and when several k states are excited an angular wavepacket is generated [6, 21]. A radially-localized wavepacket has the appearance of a shell oscillating between the nucleus and the outer turning point. The radial wavepacket does not represent the ideal classical limit of a single particle orbiting in a ellipse, because the localization is in the radial coordinate only and not in the angular coordinates. The radial wavepacket corresponds to an ensemble of different classical particles each traveling in a classical orbit, each with exactly the same phase in its orbital motion but with the directions of the ellipses distributed about all of the different possible angular orientations in space. Each particle approaches the nucleus at the same time and each reaches the outer turning point at the same time. The oscillations are at the classical orbit period, which is given by the inverse of the energy spacing between the excited Rydberg levels

$$\tau_K = \frac{2\pi}{\Delta E} = 2\pi n^3. \tag{1.23}$$

The long term evolution of the wavepacket is more complex. If the Rydberg states, which compose the superposition were equally spaced in energy, the localization and motion of the wavepacket would continue unchanged. But the energy levels are nearly equally spaced. The remaining variation in the spacing between the levels ($\frac{3}{n^4}$) causes the wavepacket to spread slowly and after a time the wavepacket is no longer localized. The spreading is smooth along the orbit until the tail of the wavepacket meets with its head. At this point a new interference pattern begins to form and small wavepackets emerge. This fractional periodicity is called fractional revival. After a period of

$$\tau_r = \frac{3}{2}\pi n^4, \tag{1.24}$$

the wavepacket becomes fully localized again. As mentioned before angular wavepackets are created by coherent superposition of several Stark states of one Stark manifold. The spacing between subsequent energy levels is

$$\Delta E = 3Fn, \tag{1.25}$$

giving a wavepacket oscillation time of

$$\tau_s = \frac{2\pi}{3Fn}. \tag{1.26}$$

Since the spacing is k independent there is in principle no dispersion. Since Stark states are linear combinations of zero field l states, in time an angular wavepacket oscillates between $l = 0$ and $l = n - 1$. Once a coherent superposition of states in the n-mixing regime is excited, a combination of a radial and angular wavepacket

Table 1.2: Characteristics of a half-cycle pulse

	Half-Cycle Pulse
pulse duration	0.5 - 1 ps
frequency range	100 GHz - 3 THz
mean wavelength	300 μm
mean photon energy	33 cm^{-1} / 4 meV

is excited, with both radial and Stark oscillations. A wavepacket can be created by using either a short many-cycle optical pulse [6, 21] or a half-cycle pulse [9, 10]. Experimentally the motion of the Rydberg wavepacket can be probed by a short laser pulse. Often a short many-cycle optical pulse is used, but also a half-cycle pulse can be used to follow the motion of the wavepacket [10,22,23]. Using an optical pulse, the electron can absorb a photon and ionize only when the electron is close to the core. Therefore an optical pulse probes when the electron is near the core. An advantage of a half-cycle pulse is that it can probe the electron over the whole orbit.

1.3 Half-Cycle Pulses

The work in this thesis has explored the dynamics of Rydberg atoms, which are subjected to a kick from a half-cycle pulse (HCP). In this case the atom is not subjected to an oscillating field at all but to a half cycle, linearly-polarized electromagnetic field, confined to a very short time interval with a frequency spectrum in the THz regime. The pulse duration of such HCP is much shorter then the roundtrip time of high Rydberg states. The characteristics of such HCP are shown in Table 1.2. These half-cycle pulses are generated by illuminating a semiconductor wafer by ultrashort optical pulses with photon energy above the band gap. The created electron-hole pairs are accelerated by a bias. The change in carrier density and therefore the change in surface current density generates the HCP. The low-frequency components of the HCP will begin to diffract more rapidly than the high-frequency components. This produces a filtering effect that will change the shape of the electric field in the far field and will produce a single half-cycle followed by a much longer and much weaker half cycle of opposite polarity, often called the tail of the HCP (Fig. 1.10). The integral of both half-cycle parts is equal. Frey *et al.* [10, 24] used another experimental method to generate HCP pulses with a pulse duration shorter than the roundtrip time of an electron, and used them to explore extremely high n-states ($n \sim 400$). These high Rydberg states could be ionized by a nanosecond long HCP created by applying a voltage pulse, produced by a pulse generator to an electrode. This HCP was not followed by a tail. The difficult part is to generate an environment, with stray electric fields smaller then 50 μVcm^{-1} to be able to create very high, stable Rydberg states.

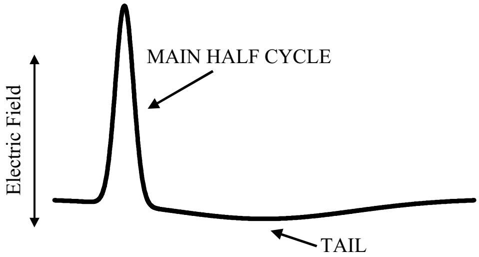

Figure 1.10: *Electromagnetic radiation in the form of a single half-cycle followed by a much longer and much weaker tail of opposite polarity. The integral of both half-cycle parts is equal. The frequency of this electromagnetic radiation is in the THz regime.*

1.3.1 Impulsive approximation

In the regime where the half-cycle pulse duration is much shorter than the classical round-trip time of the Rydberg electron the ionization can be described using the impulsive kick model. In this impulsive approximation the HCP transfers a momentum kick to the Rydberg electron at any point of its orbit. The change in momentum is given by

$$\Delta\mathbf{p} = -\int_{-\infty}^{\infty} \mathbf{E}_{HCP}(t)dt, \tag{1.27}$$

where $\mathbf{E}_{HCP}$(t) is the (time varying) electric field of the HCP. The change in total energy of the Rydberg electron after excitation with the HCP is given by

$$\Delta E = \mathbf{p}_0 \cdot \Delta\mathbf{p} + \frac{1}{2}\Delta p^2, \tag{1.28}$$

where $\mathbf{p}_0$ is the initial momentum of the Rydberg electron in the kick direction. In general the energy transfer to the electron depends on its initial momentum $\mathbf{p}_0$ and therefore varies over the orbit. If the energy change is greater than the binding energy of the Rydberg electron the atom can ionize. Hence, a HCP interacts with Rydberg states in a different way than 'many-cycle' optical pulses do. Optical pulses only interact with the electron if the electron is near the core, as for other parts of the orbit $\Delta\mathbf{p} = 0$ for an optical pulse. The energy gained by a particle from an optical field is given by

$$E = -\int \mathbf{E}_{optical}(t) \cdot \mathbf{v}dt, \tag{1.29}$$

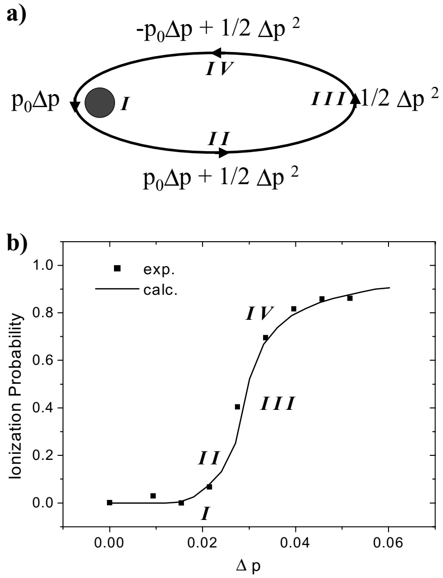

Figure 1.11: *HCP ionization behavior. At small kick strength the HCP will first ionize the fast electrons near the core. When the kick strength increases also the electrons near the outer turning point will be ionized, and finally the electrons which are moving opposite to the HCP kick will ionize. The ionization probability curve has an 's-shape'. In b) a measured and calculated ionization 's-curve' of* $n = 35$ *in Xenon is shown. The origin of the ionization is illustrated in a).*

where $\mathbf{v}$ is the velocity of the particle and $\mathbf{E}_{optical}$ is the electric field. The electrons will not absorb energy from a 'many-cycle' optical pulse when they are near the outer turning point of the orbit moving slowly, but will absorb energy from an optical pulse when they are near the nucleus moving rapidly and the velocity changes direction during one monocycle. For optical pulses the photon energy is most essential for ionization, while for HCP the field amplitude determines the ionization probability. The ionization yield when ionizing with an optical pulse changes linearly with the intensity of the pulse for a one photon process, whereas the HCP ionization curve has a s-like shape. This can be understood as follows (shown schematically in Fig. 1.11a): When the electron is close to the nucleus, its initial momentum is very large. In that case during the interaction with the HCP

$$\Delta E = \frac{1}{2n^2} = \mathbf{p}_0 \cdot \Delta \mathbf{p} \tag{1.30}$$

will be the dominant term. When the electron is at the outer turning point of the orbit where $\mathbf{p}_0$ is zero,

$$\Delta E = \frac{1}{2n^2} = \frac{1}{2}\Delta p^2. \tag{1.31}$$

With increasing kick strength the HCP will first ionize the fast electrons near the core, when the kick strength increases also the electrons near the outer turning point will be ionized and finally the electrons which are moving opposite to the HCP kick. Because the electron density is not distributed equally around the orbit, i.e. the highest density is near the outer turning point, the ionization probability curve has a s-shape. This ionization probability 's-curve' is observed both experimentally [25,26] and theoretically [15,27,28]. See Fig. 1.11b where both a measured and calculated ionization probability curve are drawn of the ionization of $n = 35$ in xenon in a field free surrounding. The s-shape is clearly visible. As mentioned before at low fields the ionization happens near the core and the field required to ionize is

$$E_{HCP} \sim \Delta p = \frac{1}{n^2}. \tag{1.32}$$

To ionize all the electrons with initial velocity parallel to the kick up to zero velocity, i.e. up to the outer turning point, the probability scales as

$$E_{HCP} \sim \Delta p = \frac{1}{n}. \tag{1.33}$$

The n^{-2} dependence was observed experimentally by Jones *et al.* [25] for 10% ionization. For 50% ionization they observed a $n^{-3/2}$ dependence. Reinhold *et al.* [26] predicted $E_{HCP} \propto n^{-1}$ in the limit of ultrashort pulses.

1.3.2 Limits of the Impulsive Regime

Going towards the regime where the HCP is not infinitely short with respect to the roundtrip time of the electron ($n < 25$), Jones *et al.* [29] and Bugacov *et al.* [30] obtained respectively some experimental and theoretical difference in ionization probability for opposite kick directions. When ionizing oriented states in an electric field (blue and red Stark states), they found that it is easier to ionize the atom if the electron is kicked away from the nucleus, than if it is kicked towards the nucleus. If the electrons are kicked towards the nucleus, some of the faster electrons will turn around the nucleus during the HCP interaction. After turning, the electrons move opposite to their original direction and if the field of the HCP is still present, this means that energy is returned to the field, and the total energy transfer is lower. If the electrons are kicked away from the nucleus their direction can not be changed. As mentioned before, the exact shape of the HCP is a main peak followed by a tail with opposite polarity. The effect of this negative tail following the HCP can alter the ionization probability, according to Tielking *et al.* [13] and Wesdorp *et al.* [14]. Tielking *et al.* studied the effect of HCP imperfections on the ionization of Rydberg atoms. An optical gating technique was used to attenuate substantially unwanted components in the HCP which appear after the main half cycle. They showed that the tail of the HCP decreased the ionization probability. During the tail electrons which had been promoted to the continuum by the main peak are recombined with the ion. Approximately 11 ps after the main pulse, a second increase in the ionization signal occurs. This increase is caused by a reflection of the main pulse due to imperfect transmission of the pulse through the radiating wafer. Wesdorp *et al.* showed that for very high Rydberg states ($n > 70$), when the orbit time is much longer than the duration of the full asymmetric monocycle, the ionization is suppressed enormously. The orbiting time of a Rydberg state scales as $\tau \sim n^3$ and for $n = 80$ the orbit time is equal to $\tau = 77ps$. Beyond this principal quantum number, the duration of the full monocycle is short compared to the orbiting period of the Rydberg electron and the change in momentum (see Eq. 1.27) is equal to zero. This would result in very little energy change of the Rydberg electron. Nevertheless Wesdorp *et al.* noticed that such an asymmetric monocycle does not leave the Rydberg state completely unaffected since the first unipolar feature kicks an electron in the direction of the polarization of the main HCP, while the second delayed tail stops the electron again. Therefore, a displacement of the electron is introduced and redistribution to higher Rydberg states is observed.

1.3.3 Momentum Retrieval

HCP can be used to retrieve the momentum-space probability distribution in the direction of the kick of essentially any wavepacket [9, 15, 31]. This method for measuring a component of the momentum distribution of a Rydberg electron is based on the idea that within the impulsive approximation, the energy change is given by Eq. 1.28. If the energy change is greater than the binding energy, the electron will leave the atom. This means that the percentage of the atoms ionized equals the percentage of the electrons with

$$\mathbf{p}_0 > \frac{\frac{1}{n^2} - \Delta p^2}{2\Delta \mathbf{p}}. \tag{1.34}$$

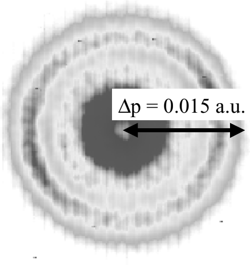

Figure 1.12: *Velocity map image of photoionization of metastable Xenon just above the saddle point. The kinetic energy of the ejected elecrons was 3 meV.*

The experiment measures

$$\int_{\mathbf{p}_0}^{\infty} D(\mathbf{p}) d\mathbf{p}, \tag{1.35}$$

where $D(\mathbf{p})$ is the probability density for the electron to have momentum $\mathbf{p}$. So by measuring the ionization probability as a function of field, the momentum distribution can be obtained using Eq. 1.35. Zobay and Alber [32] calculated angle- and energy resolved spectra resulting from the ionization of Rydberg atoms by HCP in a field-free condition. Their spectra showed that the final direction into which the electron is emitted is strongly correlated with the momentum in the orbit before application of the pulse. The initial momentum distribution in the direction perpendicular to the kick did not change during the ionization by a HCP. So if there exists a technique which could measure the momentum distribution of HCP ionized electrons, we would have a new tool for momentum spectroscopy. The velocity imaging detector [33] seems to be very useful for this idea.

1.3.4 Velocity Imaging Detector

In this velocity imaging technique [33], electrons with the same velocity vector are mapped onto the same point on the detector. The electrons or ions produced in the interaction region are extracted by an electrostatic lens which can be operated such that particles with the same initial velocity vector are mapped on the same point on the detector, irrespective of their initial position. The 3D velocity distribution is projected to a 2D distribution on the detector. A second electrostatic lens was installed to magnify the image of the low energy electrons on the detector [34]. If there is an axis of symmetry in the interaction region parallel to the plane of the detector, then the original 3D distribution can be calculated from the 2D image using an inverse Abel transformation [35] or an iterative procedure with forward transformation [36].

In most experiments the electric field in the interaction region does not play any role in the experiment, except from transporting the electrons towards the detector. In our experiment such a symmetry axis does not exist since in the experiments described in this thesis the static electric field has a significant effect on the Rydberg atom as witnessed by the Stark structure. As a consequence the velocity distribution of the component parallel to the electric field can not be reconstructed. Only the velocity components of the electrons perpendicular to the static electric field reveal the effects of the HCP excitation, in a displacement on the detector. Usually the interaction of the electron with the Coulomb field is neglected and electrons follow simple ballistic trajectories. The coordinates of the impact on the detector can be derived using very simple algebra. Electrons emitted at a given position with a kinetic energy W in a static electric field F detected at a distance L from the origin give rise to a circular image of radius

$$R \approx 2L\sqrt{\frac{W}{qFL}} \tag{1.36}$$

with a filling pattern that reveals the original angular distribution of the electrons. This is realistic for the case of electrons with kinetic energy large enough so that the Coulomb interaction which prevails on typical distances of a few micrometers is low compared to the kinetic energy (typically $W > 10$ meV). However, the Coulomb attraction between the electron and the ionic core can not be neglected when slow electrons are concerned. The combined Coulomb and electric field exhibit a focusing effect depending on the ejection angle of the low energy electrons. The problem of an electron in the combination of a Coulomb and an electric field has exact analytical solutions in classical mechanics [37]. Comparing these exact analytical solutions with calculated ballistic trajectories for slow electrons we noticed that the exact radius was 70% of the expected ballistic radius. In the case of our HCP ionization experiments this focusing effect of the combined Coulomb field and electric field cannot be neglected for low kick strengths. The measured momentum distribution tells us something about the momentum distribution as far as several micrometers away from the ionic core, when the influence of the Coulomb field can be neglected. For high kick strengths the kinetic energy of ejected electrons is much higher than 10 meV and the Coulomb field does not change the initial momentum of the electrons. We performed near-threshold photoionization experiments [38,39] to express the observed displacements, Δx and Δy, of the electrons on the detector in momentum, p_x and p_y. Analytical calculations describe the electron trajectories and provide the relation between displacement of the photoionized electrons and their final momentum. In Fig. 1.12 a velocity map image, used for calibration of near-threshold photoionization of metastable xenon is shown. The kinetic energy of the ejected electrons is 3 meV.

Chapter 2

Aspects of Picosecond THz Generation and Detection

We discuss two ways of generating (sub)picosecond pulses in the THz regime. a) Ultra-short so-called half-cycle pulses (HCP) with frequencies in the THz regime have been generated by photoconduction in a semiconductor (GaAs). In the case of biased photoconductors, the acceleration of photogenerated carriers results in the emission of a half-cycle pulse with FWHM of 0.55 ps in the far field and 0.83 ps in the near field. Generation of HCP induces electronic noise. We developed a simple method to reduce this electronic noise significantly. b) An alternative source of high intensity, picosecond far infrared few-cycle pulses has been tested at the Free Electron Laser for Infrared eXperiments (FELIX) facility. The 20 ps long far infrared output of the free electron laser is sliced into shorter pulses with variable length using laser activated semiconductor reflection switches. We have demonstrated that with this so-called pulse slicing technique it should be possible to create pulses, which exist out of one or two optical cycles. In both cases the time varying electric field of both the half-cycle pulse and the few-cycle pulse is measured by electro optical sampling. In the latter case, a single shot set-up is necessary and has been developed.

2.1 Introduction

The generation of ultrashort electromagnetic pulses has been a challenge for a few decades. At present, pulses of a few femtosecond have been generated in the optical and VUV regime. A very special broadband pulse would consist of a single full cycle pulse or even only half an optical cycle. This has not yet been achieved in the visible or VUV regime. The highest frequency for which half an optical cycle has been generated is the THz regime. This chapter describes two techniques to generate a) single half-cycle pulses and b) variable few-cycle pulses, which can be used to manipulate Rydberg atoms. Several experiments show that the ionization of a Rydberg atom by a half-cycle pulse, which is shorter than the classical orbit time, can be described by the so-called impulsive kick model [25–27]. Ionization takes place if the energy transfer during the interaction of the HCP with the Rydberg atom is larger than the binding energy, i.e. if the electric field is strong enough. The ionization probability versus the electric field strength is shaped as an S-curve. In contrast, in the case of many-cycle optical pulses ionization only takes place if the photon energy is larger than the binding energy. In the one-photon regime the ionization probability increases linearly with the intensity. In going from many cycles to a single half cycle a transition is expected for ionization depending on the photon energy to ionization depending on the electric field of the optical pulse. From this point of view it would be advantageous to generate pulses, with a tunable amount of cycles. We will describe the generation and detection of a half-cycle pulse in section 2.2. The generation of such half-cycle pulses causes strong electronic noise. We will show a method to reduce this electronic noise significantly in section 2.3. Finally in section 2.4, we will describe the generation and detection of few-cycle radiation starting from a many-cycle, so called micropulse from a free electronlaser.

2.2 Half-Cycle Pulse

2.2.1 Introduction

There are two distinct approaches for generating subpicosecond electromagnetic half-cycle pulses (HCP) with frequencies in the THz regime ($\nu = 1$ THz, $\lambda = 300\ \mu$m, energy in cm^{-1}(ν/c) $= 33.3$ cm^{-1}); photoconduction [40–42] and optical rectification [43–45]. In the case of biased photoconductors, the acceleration of photogenerated carriers results in emission of the THz pulse. In the case of optical rectification near degenerate difference-frequency generation in electro-optic crystals results in the generation of THz pulses. The advantage of photoconduction over optical rectification is that, in practice, very high electric field strengths can be reached. The field strength of the generated HCP depends on the applied bias. In the case of optical rectification the field strength can only be changed by altering the intensity of the incident light. Another advantage of photoconduction is the ability to control the polarity of the electric field of the HCP by altering the bias over the photoconductor. In our group we generated half cycle electromagnetic radiation from photoconducting antennas with pulse lengths near 0.55 ps (FWHM) in the far field and 0.83 ps in the near field region. These pulse durations are associated with THz radiation. The time measurement of the electric field was performed using electro optical sampling. Electro optical sampling is commonly used to detect the temporal shape of electromagnetic pulses [46–48] and is based on the Pockels effect: The applied electric THz field induces birefringence in a crystal, which affects the polarization of an optical probe. Two alternative techniques may be mentioned here. a) One sampling method uses photoconductive antennas [41, 49, 50]. The electric field of the HCP generates a current in the photoconductive antenna. The photoconductivity is switched with a ultrashort femtosecond pulse. The current through the photoconductive antenna is detected as a function of delay time between the arrival of the HCP and the switching femtosecond pulse. The spectral bandwidth of the antenna is determined by the semiconductor material and the wafer size. The smaller the wafer, the broader the spectral bandwidth. This is expected as the transition time from negative to positive peaks is faster and allows higher frequencies [48–50]. b) Another technique commonly used is an interferometric measurement [42, 51], i.e. an autocorrelation measurement of THz pulses. The THz pulse is directed into a polarizing Michelson interferometer. The interferometer consists of a polarizing beam-splitter rotated 45° relative to the polarization of the incident THz pulse. The reflected and transmitted light pulses are of equal intensity and orthogonally polarized. Retroreflectors in each arm rotate the polarization of the incident light 90°. The transmitted and reflected pulses are recombined at the beamsplitter. The output energy of an interferometer is measured with a bolometer while scanning one arm of the interferometer. In practice, this technique is limited by the thermal noise of the bolometer.

2.2.2 Generation of Half-Cycle Pulses

The generation of THz pulses using a photoconducting wafer is based on the following concept: When the surface of a semiconductor wafer is illuminated by ultrashort optical pulses with photon energy above the band gap, electron-hole pairs are created. These carriers are accelerated by a bias electric field, that is applied across the surface. The change in carrier density and therefore the change in surface current density $\mathbf{j}(t)$ is proportional to the incident optical intensity $I(t)$, in the absence of electron recombination and saturation, and to the applied bias ($\mathbf{E}_b$)

$$\frac{d\mathbf{j}(t)}{dt} \propto I(t) \cdot \mathbf{E}_b. \tag{2.1}$$

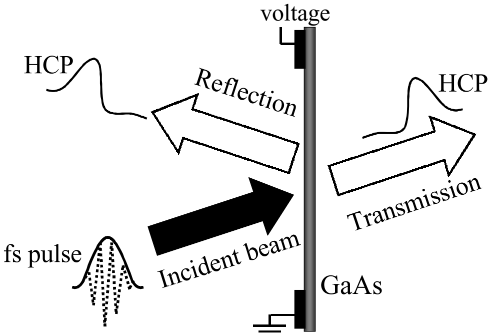

Figure 2.1: *Experimental setup for generation of half cycle pulse radiation.*

The radiated electric field is proportional to the acceleration of the carriers, which is again equal to the time derivative of the surface current density

$$E(t) \propto -\frac{d\mathbf{j}(t)}{dt} \propto -I(t) \cdot \mathbf{E}_b \tag{2.2}$$

so that the radiated field follows the intensity profile of the incident optical radiation. The minus sign in Eq. 2.2 reflects that the generated electric field opposes the carrier current, because the generated electric field wants to compensate for the carrier current. The response function of the charge carriers in the GaAs surface slows down the pulse. In the near field, the time profile of the electric field has the shape of a single half cycle with a maximum field strength that scales linearly with the applied bias. As the distance from the wafer increases, the low frequency components will diffract more rapidly than the high frequency components. This produces a filtering effect that changes the shape of the electric field pulse in the far field and produces a main half-cycle pulse followed by a long tail with opposite polarity [41], resulting in a far field situation, in which the time integral of the electric field equals zero. The direction of the radiated pulse can be controlled by varying the angle of incidence of the optical pulse.

The generation of HCP radiation is shown in Fig. 2.1. A (100)-oriented undoped semi-insulating GaAs wafer (high-resistivity crystalline wafer, 0.5 mm thickness, one side polished and one side etched) was soldered on electrodes evaporated on an epoxy board with a 1 cm gap between the electrodes. If the photoconductor aperture is much larger than the wavelength of the radiated pulses, the radiated beam will be collimated. A pulsed electric field (a few kV) was applied across the surface provided by an automotive spark coil such that a higher voltage could be applied before electric breakdown occurred. With a pulsed electric field, a voltage up to 7 kV/cm can

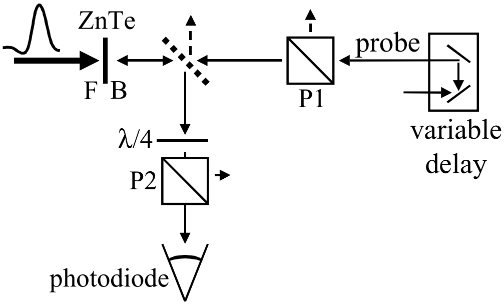

Figure 2.2: *Electro-optical sampling setup to detect the HCP temporal profile. See text for details.*

be applied without sparking. Sparks, appearing between electrode and wafer edge, damage the GaAs wafer. The polished side of the wafer was illuminated at normal incidence by pulses from a Ti:sapphire laser, producing 75 fs pulses at 795 nm, with a repetition rate of 1 kHz. THz radiation was generated in both transmitted and reflected directions, but we used only the transmitted radiation. The temporal shape of the HCP was detected by electro optical sampling.

2.2.3 Detection of Half-Cycle Pulse

The temporal shape of the THz pulse can be detected by free-space electro-optic sampling, a method based on the Pockels effect. In the presence of an electric field the birefringence of an electro-optic crystal will be modulated. The electric field of a THz pulse, aligned along an optical axis, introduces phase retardation between the two propagation axes in an electro-optic crystal. The induced phase retardation affects a light pulse, which is linearly polarized at 45°with respect to the optical axis and HCP polarization. Although this angle of 45° is commonly used, it is not the most efficient angle [78]. Linearly polarized light becomes elliptically polarized due to the induced phase retardation. The elliptic modulation of the beam can then be polarization-analyzed to provide information on the amplitude of the applied electric field. The light transmitted through the polarizer is described by:

$$I = I_0(\eta + \sin^2(\frac{\Gamma_0 + \Gamma}{2})), \tag{2.3}$$

where I_0 is the intensity of the incident light, η represents the background due to the scattering of the electro-optic crystal and the imperfection of the polarizers and other optics between the polarizers, Γ_0 is the phase retardation caused by the natural birefringence of the electro-optic crystal and Γ is the phase retardation which depends on the electric field strength of the HCP and of the thickness of the electro-optic crystal. Ignoring the velocity mismatch between HCP and probe and the absorption of the HCP in the ZnTe crystal, the induced birefringence, the induced birefringence Γ by the electric field of the HCP F_{HCP} is [52, 53]

$$\Gamma = \frac{\pi d n^3 r_{41}}{\lambda} E_{HCP}, \tag{2.4}$$

where d is the crystal thickness, n is the refractive index, r_{41} is the electro-optic coefficient, and λ is the wavelength of the probe beam. For ZnTe, $r_{41} = 3.9$ pm/V and $n = 2.85$ at 800 nm, and we use $d = 1.0$ mm, $\lambda = 800$ nm. In fact, the electric field of the HCP induces very small Γ changes [53, 54]. The magnitude of Γ is about 0.035 at 1 kV/cm. When Γ is small, Eq. 2.3 can be approximated as

$$I \approx I_0 \left(\eta + \left(\frac{\Gamma_0 + \Gamma}{2} \right)^2 \right) = I_0 \left(\eta + \frac{1}{4}\Gamma_0^2 \right) + I_0 \left(\frac{1}{2}\Gamma_0 \Gamma + \frac{1}{4}\Gamma^2 \right), \tag{2.5}$$

where $I_0\left(\eta + \frac{1}{4}\Gamma_0^2\right)$ describes the constant small background and $I_0\left(\frac{1}{2}\Gamma_0\Gamma + \frac{1}{4}\Gamma^2\right)$ represents the signal which depends of the electric field of the HCP. To increase the signal-to-background ratio, one should use polarizers and an electro optic crystal with good quality, which decreases η. In principle $|2\Gamma_0| > |\Gamma|$, so the intensity is linear with Γ, i.e. the electric field [53]. In principle, a quarter wave plate can be used to enhance the detection sensitivity through an increase of the phase retardation with $\frac{1}{2}\pi$. Developing Eq. 2.3 in a Taylor series around Γ is zero gives

$$I \approx I_0(\eta + \frac{1}{2}(1 + \Gamma + \Gamma_0)), \tag{2.6}$$

The detection will take place in the linear response part of the $\sin^2$ function and the sensitivity is greatly enhanced. The disadvantage is that the measurement detects a change on a rather large background.

The electro-optical-sampling setup to detect the HCP pulse is shown in Fig. 2.2. We used a 1 mm thick (110)-oriented Zinc Telluride (ZnTe) crystal with the optical axis parallel to the electric field polarization of the HCP pulse. A thin crystal was chosen to reduce the influence of velocity mismatch between the femtosecond probe pulse (groupindex of refraction $n_g = 3.24$ [55]) and the HCP pulse (refractive index $n = 3.17$ [56]). In principle, a linearly polarized femtosecond pulse propagates collinearly with the HCP pulse inside the electro-optic crystal and probes the field-induced change in the index of refraction. The probe pulse is split off from the femtosecond beam by a pellicle beamsplitter and linearly polarized at ~ 45° with respect to the HCP by polarizer P1. The duration of the probe pulse is shorter than the duration of the HCP pulse; therefore the temporal shape of the HCP pulse could be measured by changing the relative delay between the HCP pulse and the probe pulse while monitoring the phase retardation of the probe beam. In practice, the probe pulse was sent into the electro-optic crystal from the back surface, indicated by a B in Fig. 2.2, with respect to the direction of the incoming HCP pulse, indicated by an F. The reflection of the probe beam on the front side of the crystal propagates collinearly with the HCP and probes the field-induced change in the index of refraction. As a consequence, the reflection of the probe beam on the front side of the ZnTe crystal, the phase retarded part, overlaps in space with the reflection on the backside of the ZnTe crystal, when the beam enters the crystal. In practice the front and back side of the ZnTe crystal are not parallel and the two reflections separate at longer distance from the crystal. The phase retardation was converted into an intensity modulation by passing the light through a polarizer P2 and detecting the transmission with a photodiode. As mentioned before a quarter waveplate placed between crystal and the polarizer, enhances the detection sensitivity and generates a linear response over a broad intensity range. The induced phase shift increased the background. To compensate for this effect a baseline subtraction method was used. The photodiode signal was integrated with a boxcar. The boxcar and femtosecond laser system worked at 1 kHz. The GaAs wafer was only biased at 500 Hz, making baseline subtraction by the boxcar possible. The boxcar averaged one thousand times. The response was very weak. So first the overlap point between pump and probe was determined within a few mm by an autocorrelation measurement of the femtosecond probe pulse and the femtosecond pulse, which illuminates the GaAs wafer, using second harmonic generation in a BBO crystal.

2.2.4 Results

The temporal shape of a half-cycle pulse was measured with electro optical sampling in the near field (1cm) and far field (35 cm), shown respectively in Figs. 2.3a and 2.3b. To get a decent signal-to-noise ratio the results were averaged over several scans. The measurement of the electric field strength at the end of the HCP is influenced by the first part of the HCP which counterpropagates with the probe pulse before the probe pulse is reflected on the front side of the crystal. Although the field strength in the counterpropagating part is stronger than at the end of the HCP, the effect is weak, because the overlapping time with the counterpropagating part is much shorter ($\sim$ 0.5 ps) than with the copropagating part ($\sim$ 10 ps). In Fig. 2.3 we see two peaks appearing. The second peak delayed by 20 ps with respect to the first peak, was caused by overlap of an internal reflection of the HCP pulse with the principal femtosecond probe beam on the back side of the crystal. The THz pulse and femtosecond probe beam have an index of refraction inside the ZnTe of respectively$n_g = 3.17$ and $n = 3.24$, which causes a delay of 21.4 ps. The reflection of the HCP copropagates with the femtosecond probe beam towards the front side of the crystal. A part (30%-50%) of both beams is reflected on the front side and detected

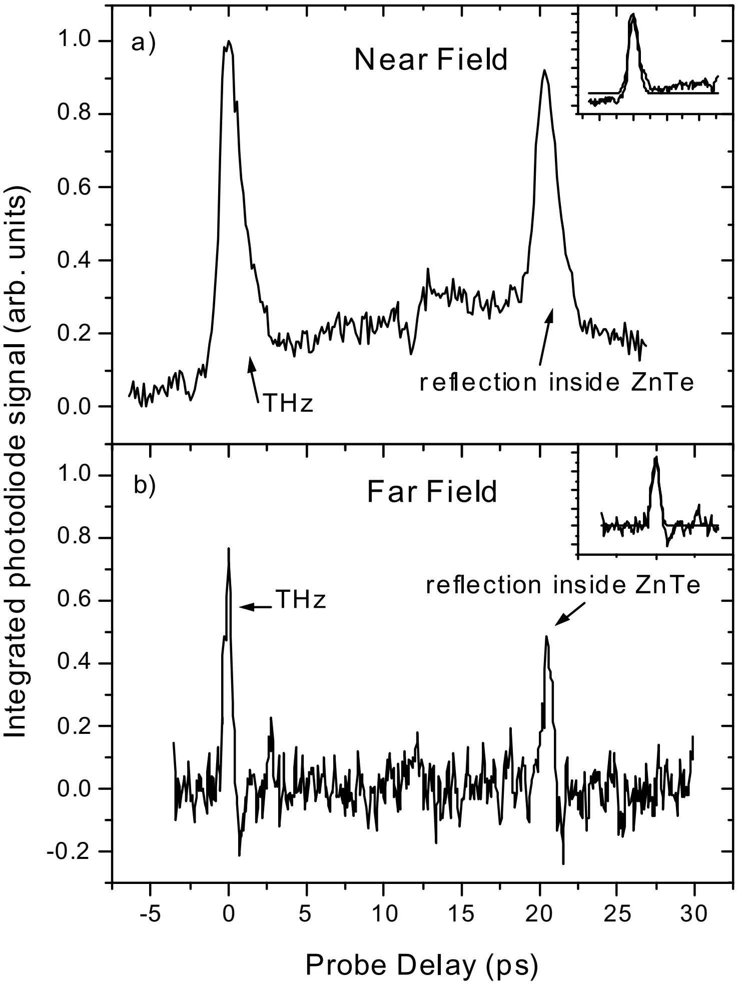

Figure 2.3: *The measured temporal shape of a HCP in a) the near field and b) the far field. The temporal shape of the HCP could be fitted with a gaussian beam profile, see insets. The FWHM of the HCP was 0.83 ps in the near field and 0.55 ps in the far field.*

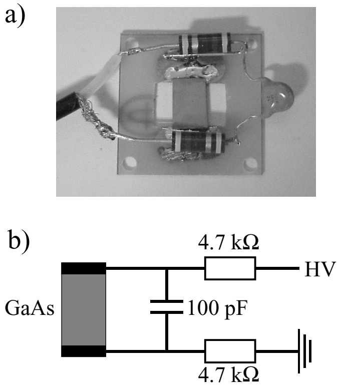

Figure 2.4: *a) Photograph of the back side of the GaAs wafer with the RC circuit. The GaAs wafer was soldered on an epoxy print board. The RC circuit was mounted parallel to the wafer. b) Schematic illustration of the wafer with the RC circuit*

by the photodiode. The signal of the reflection is strong because of the relatively large reflections on the crystal faces, and because the HCP copropagates with the probe beam two times over the crystal length. The HCP could be fitted with a Gaussian beamprofile, see insets in Fig. 2.3, resulting in a full width at half maximum (FWHM) of 0.83 ps in the near field regime and 0.55 ps in the far field regime. In the near field the HCP is longer, because radiation at the edge of the wafer had to travel about 10 mm extra (3 ps) then the radiation generated at the middle of the wafer before reaching the ZnTe crystal. The long weak tail of the HCP pulse disappears in the noise.

2.3 Reduction of Electronic Noise in THz Generation

In recent years, it has become possible to generate ultrashort freely propagating electrical pulses, which approximate a half cycle, and which have a frequency spectrum in the THz regime. These pulses are referred to as half-cycle pulses (HCP) [41–43]. HCP have been applied in THz time domain spectroscopy [57, 58] and in the manipulation of Rydberg atoms [8, 11], see Chapters 3, 4 and 5. HCP are generated by illuminating a biased semiconductor wafer with a femtosecond laser with a photon energy larger than the band gap. Unfortunately, the process of HCP formation generates significant electronic noise during approximately 200 ns which disturbs many experiments. We present a simple method to reduce this electronic noise significantly. We will demonstrate this method of noise reduction in an experiment in which HCP are used to ionize highly excited Rydberg atoms.

In our experiment, a biased GaAs wafer is illuminated with 100 fs 800 nm pulses from a Ti:Sapphire laser. The resulting electron-hole pairs are accelerated by the bias electric field (1-8 kV) across the wafer surface. The acceleration of these carriers is the source of a short ($\leq$ 1ps) half-cycle electromagnetic pulse. As the femtosecond pulse hits the wafer, the resistance steeply drops and a strong current is drawn. As a results, the cables between the power supply and the wafer generate strong perturbing electromagnetic fields. This problem can be solved by mounting an RC circuit directly on the wafer, thereby creating a local power supply. The RC circuit can be used in combination with both continuous and pulsed electric supplies. Pulsed electric supplies are employed when the bias voltage is close to the breakdown voltage of the wafer. When using a pulsed bias field, the RC time needs to be commensurate with the current limitations of the electric supply. The RC circuit used in our experiment is illustrated in Fig. 2.4. Ignoring the capacity of the GaAs wafer, the RC time of this RC circuit was chosen to be about 1 μs.

To demonstrate the effect of the RC circuit on the electronic noise, we ionized a highly excited state in an atom, a so-called Rydberg atom, by a HCP generated by a wafer with and without the RC circuit. We checked that the voltage with and without the RC circuit was the same in our experiment ($\sim$ 7.5 kV). Highly excited Rydberg atoms ($n = 44$) were created in a vacuum setup ($p = 10^{-7}$ mbar) in a static electric field (80 Vcm^{-1}) by photon excitation of rubidium atoms evaporated from an oven by a standard dye-laser system. Hereafter, the atoms were subjected to the HCP, generated outside the vacuum chamber, causing ionization. By changing the sign of the static electric field, we accelerated either the electrons or the ions toward a microchannel plate detector, equipped with a fast circuit to obtain a time resolved signal. In Figs. 2.5a and 2.5b the ionization signal is shown that is generated by a HCP without the RC circuit. During the first 200 ns, the ionization signal is clearly disturbed by electronic noise. The flight time for ions toward the detector ($\sim$ 5 cm) is in the microsecond regime. The ions will arrive at the detector after the electronic noise, and the signal can be separated in time. However, electrons that have a flight time of only a few ns will arrive within the time period of the electronic noise. In this case, the RC circuit on the wafer has to be used to reduce the electronic noise, see Figs. 2.5c and 2.5d. In conclusion, we showed that electronic noise induced by the generation of HCP can be reduced significantly.

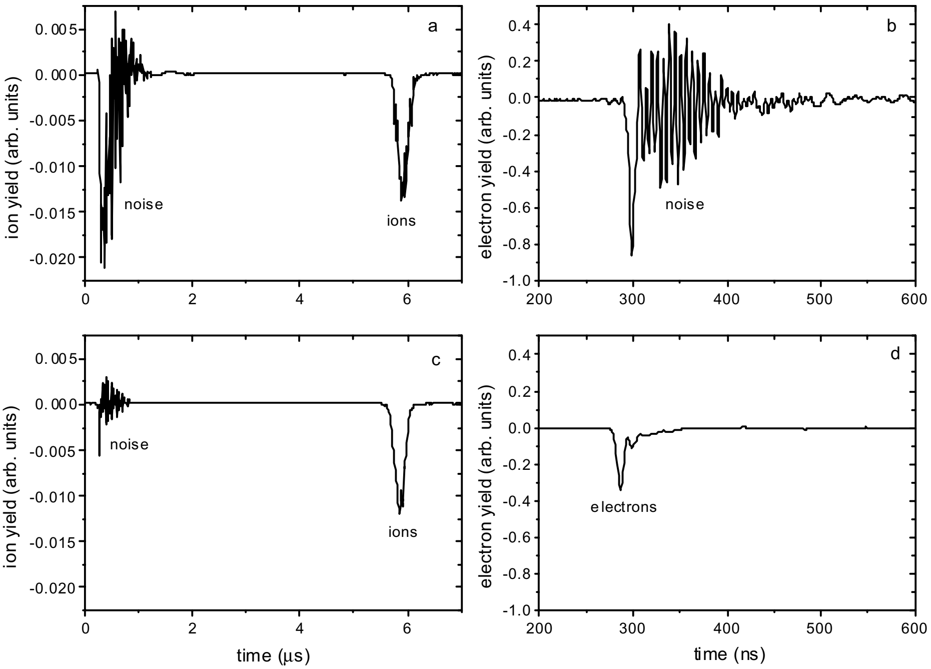

Figure 2.5: *In a) and b), respectively, the ion and electron signals are shown of ionization of a Rydberg atom by a HCP. The electron signal is hardly visible through the electronic noise. In c) and d), the same signals are shown, but now the HCP is generated by a wafer with an RC circuit. Note that both the time and sensitivity scales are different for ions and electrons, because the electrons arrive in a smaller time window. The integrals of the ion and electron signal are equal. The electronic noise is reduced significantly. The difference in the noise characteristics of the ion signal in a) and c) at 6 μs is due to a different number of averages.*

2.4 Few Cycle Radiation

2.4.1 Introduction

Since the 1970s laser activated switching has been of interest to create short pulses. Some of the first experiments on laser activated switching were performed by Alcock, Corkum and coworkers [59,60] and Jamison et al. [61]. These authors observed nanosecond and picosecond long mid IR radiation (10 μm). More recently, the sliced pulses became shorter and their signal to noise ratio has improved [62,63]. All pulses contain still many optical cycles. Although most work has been done in the near and mid infrared, also results have been obtained in the far infrared. Salzmann et al. [64], Vogel et al. [65] and Hegmann et al. [67] investigated pulse slicing in the far infrared regime (120 μm) creating pulse durations longer than 20 ps. The pulse-slicing system uses laser activated semiconductor reflection switches to cut the front and back part of a longer multi cycle pulse. We show that it should be possible to use this pulse slicing technique to generate far infrared radiation of a few cycles. The temporal profile of the electric field was measured using a single-shot electro-optical detection-technique.

2.4.2 Generation of few cycle radiation: 'Pulse slicing'

We have developed a pulse slicer system which extracts variable duration, picosecond wide terahertz pulses from many-cycle free electron laser (FEL) pulses. The pulse slicer uses a technique known as laser activated semiconductor switching. Semiconductors such as Si, Ge or GaAs are transparent in the far infrared region. In this experiment we use GaAs as switch. The reflectance R, i.e. the fraction of reflected light of radiation with frequency ω incident on the surface of a semiconductor wafer as a function of incident angle ϑ is determined by

$$R_{s,p}\left(\omega,\vartheta\right)=\left|r_{s,p}\left(\omega,\vartheta\right)\right|^{2}, \tag{2.7}$$

where r_s and r_p are the Fresnel reflection coefficients for s and p polarized light respectively, which are given by

$$\begin{aligned} r_s\left[\omega,\vartheta\right] &= \frac{\beta_1\left(\omega,\vartheta\right)-\beta_2\left(\omega,\vartheta\right)}{\beta_1\left(\omega,\vartheta\right)+\beta_2\left(\omega,\vartheta\right)}, && (2.8)\\ r_p\left[\omega,\vartheta\right] &= \frac{\frac{1}{\epsilon_1(\omega)}\beta_1\left(\omega,\vartheta\right)-\frac{1}{\epsilon_2(\omega)}\beta_2\left(\omega,\vartheta\right)}{\frac{1}{\epsilon_1(\omega)}\beta_1\left(\omega,\vartheta\right)+\frac{1}{\epsilon_2(\omega)}\beta_2\left(\omega,\vartheta\right)}, && (2.9)\end{aligned}$$

where ϵ_1 and ϵ_2 are the dielectric constants of respectively medium 1 (air) and 2 (semiconductor), β_1 and β_2 are the components of the wavevector perpendicular to the surface, respectively for medium 1 and 2

$$\beta_1(\omega,\vartheta) = \frac{\omega}{c}\sqrt{\epsilon_1(\omega) - \epsilon_1(\omega)\sin(\vartheta)^2}, \tag{2.10}$$

$$\beta_2(\omega,\vartheta) = \frac{\omega}{c}\sqrt{\epsilon_2(\omega) - \epsilon_1(\omega)\sin(\vartheta)^2}. \tag{2.11}$$

If a laser pulse with photon energy above the energy gap illuminates the semiconductor, an electron-hole plasma is formed. This dense free-carrier plasma will change the optical properties of the semiconductor and the semiconductor can become reflective for the FEL radiation. In particular, the free-carrier plasma will change the dielectric function $\epsilon(\omega)$. For a given optical frequency ω the dielectric function $\epsilon(\omega)$ for any semiconductor contains a contribution from the atomic polarizability, from phonons, and a possible free carrier component. The latter contribution to the dielectric constant is given by Drude's theory [65,68]:

$$\epsilon(\omega) = 1 - \frac{\omega_p^2}{\omega^2 + i\omega/\tau}, \tag{2.12}$$

where ω_p is the plasma frequency and τ is the free carrier scattering time. The plasma frequency is given by

$$\omega_p = \sqrt{\frac{e^2 N_c}{m_c^* \epsilon_0}}. \tag{2.13}$$

The scattering time obeys:

$$\tau = m_c^* \mu / e, \tag{2.14}$$

where e is the electron charge, N_c is the free carrier density, m_c^* is the effective mass of the carriers, ϵ_0 is the permittivity of free space and μ the mobility, which is low immediately after illumination. In GaAs, the electron mobility rises to a higher equilibrium value in about 4 ps, depending on carrier density [66]. Some properties of GaAs are given in table 1.2. The mobility is derived from doped GaAs [69]. If $\omega\tau >> 1$ then to a first approximation Eq. 2.12 gives

$$\epsilon(\omega) = 1 - \frac{\omega_p^2}{\omega^2}. \tag{2.15}$$

The role of the plasma frequency is as follows: when $\omega < \omega_p$, ϵ is real and negative and the solutions to Maxwell's equations decay exponentially in the medium; i.e., no radiation can propagate, the radiation is reflected. However, when $\omega > \omega_p$, ϵ is real and positive, the solutions to Maxwell's equations become oscillatory, i.e. radiation can propagate and the semiconductor becomes transparent. Normally for a frequency below the plasma frequency or for a wavelength longer than the plasma wavelength

$$\nu_p = \frac{\omega_p}{2\pi}, \tag{2.16}$$

Table 2.1: Properties of GaAs

Effective Mass, m_c^*/m_e	
electrons	0.067
holes	0.082, 0.45
mobility [cm^2/Vs]	
electrons	500-2400
Carrier density [cm^{-3}]	
0.5 mJ incident light	10^{20}

$$\lambda_p = \frac{c}{\nu_p}, \tag{2.17}$$

the material is a very good reflector; the reflection coefficient is equal to one for all possible angles of incidence. In the case of $\omega < \omega_p$, Eq. 2.12 results in a reflectance that is almost equal to one for all possible angles of incidence, except for p polarization near 90°, see Fig. 2.6. The change in mobility does not have much influence on the reflection, except for p polarization near 90°. Irradiation of semiconductors with short pulses leads to a rapid change of the free-carrier density. Two semiconductor elements are needed for slicing, one to switch on the reflection followed by a second to turn off the transmission of the pulse. Without the second switch the duration of the reflectivity depends on the carrier concentration in time. Two mechanisms decrease the carrier density. First, there is carrier diffusion. The second mechanism, (linear) recombination, is a process, in which electrons and holes recombine, emitting phonons or giving up their energy to a third carrier. In practice these times are of the order of nanoseconds [67].

2.4.3 Experimental Setup

An experimental arrangement for pulse slicing is illustrated in Fig. 2.7. The free electron laser, FELIX, produces megawatt-level picosecond long far infrared pulses at wavelengths ranging from 3 μm to 250 μm. The infrared beam consists of short micropulses, 6-100 optical cycles, which have at 130 μm a nominal duration of 2.5-40 ps and are separated by intervals of either 1 ns or 40 ns. The micropulses form a train, the macropulse, with a length up to 10 μs. The macropulses have a maximum repetition rate of 10 Hz. The pulse slicing system cuts a few cycles out of one micropulse in a macropulse. The FEL, operated at 130 μm, is focused by a parabolic mirror onto a GaAs wafer (0.5 mm). The wafer is set at near Brewster's angle, 73° for GaAs, to minimize background reflection from the incoming FEL radiation. In this configuration the wafer normally reflects very little of p polarized light. However, if the switch is illuminated with above band gap radiation from a laser source, the resulting free carriers make the surface of the wafer highly reflective to terahertz radi-

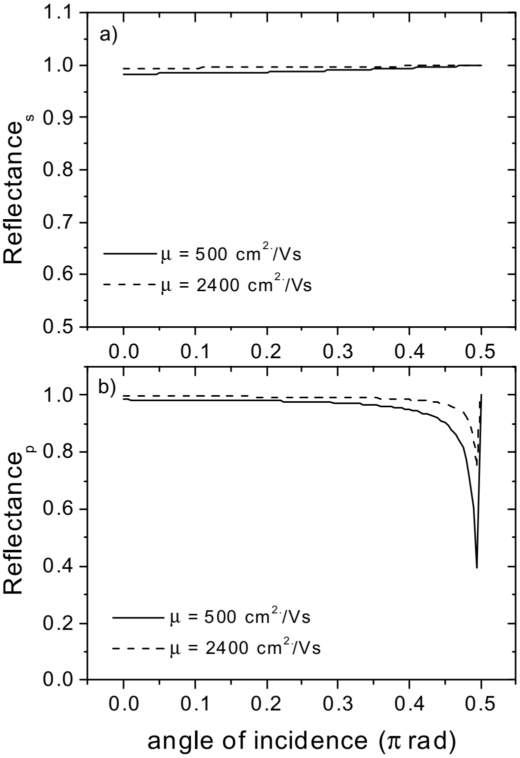

Figure 2.6: *The reflectance plotted as a function of the angle of incidence for* $\omega < \omega_p$ *for a) s-polarization and b) p-polarization. The mobility* μ *is low (500 cm*^{2}*/Vs) immediately after illumination. After a few picoseconds the mobility* μ *rises to a higher equilibrium value (2400 cm*^{2}*/Vs).*

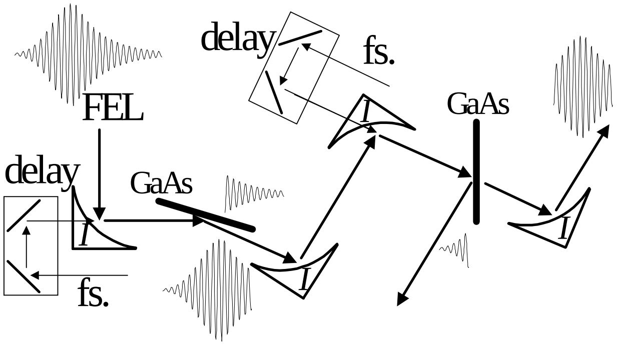

Figure 2.7: *Illustration of a 'slicing' setup. The FEL is focused by a parabolic mirror (I) onto a GaAs wafer. The switching pulse is sent through a small hole of the parabolic mirror. The front part of the FEL pulse is sliced on the first wafer and the back part on the second wafer.*

ation. We use a Ti:sapphire laser system with a multipass amplifier, which generates 25 femtosecond pulses at 791 nm with energies up to 1 mJ per pulse at a maximum repetition rate of 1 kHz. The photon energy is 1.57 eV, which is larger than the band gap of the semiconductor (GaAs 1.42 eV) . If the switching pulse illuminates the switch at normal incidence to the wafer but the FEL beam comes in at Brewster angle then the reflected FEL will not have a sharp rise time. The switching pulse must be brought in as close to collinear with the FEL beam as possible. Therefore we send the switching pulse through a small hole through the surface of the parabolic mirror, which was used to focus the FEL beam. After the first wafer the FEL light was recollimated by a parabolic mirror. The FEL radiation was focused on a second GaAs wafer with a parabolic mirror. The transmission switch was activated by a second femtosecond infrared pulse split off from the Ti:sapphire laser source. Only in the illuminated part of the wafer a plasma is formed, therefore the femtosecond beam has to overlap with the full FEL beam. Else still a part of the FEL radiation will be transmitted. By varying the time delay between the infrared pulses activating the reflection and transmission switch, the width of the pulse that gets sliced out of the FEL pulse can be varied. Up to 450 μJ was incident on both the reflection switch and the transmission switch. The optical penetration depth of the switching femtosecond pulse (radius $\sim$ 2 mm) is 0.7 μm in GaAs [67]. Assuming that one photon would generate one pair of free-carriers, the generated carrier density will be in the order of 10^{20} carriers/cm^3. Equations 2.13, 2.16 and 2.17 suggest that at this carrier density light with a wavelength longer than 500 nm will be reflected.

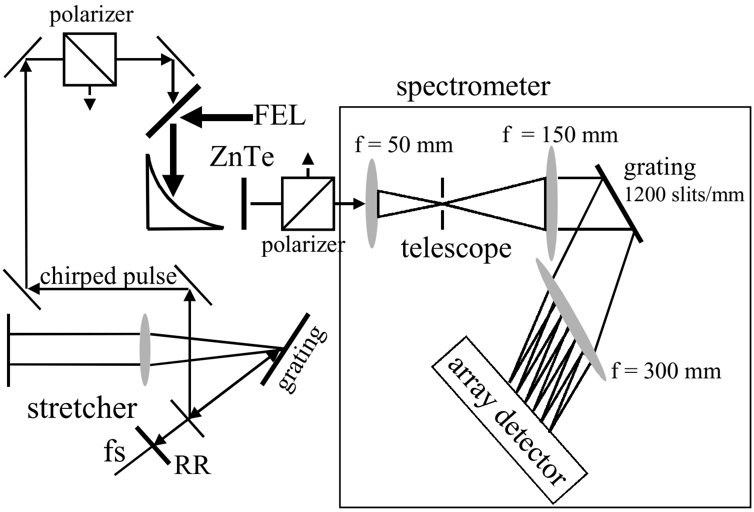

Figure 2.8: *Single shot electro-optical sampling technique to measure the temporal profile of the few cycle optical pulse. See text for details.*

2.4.4 Detection of few cycle radiation

The temporal shape of the FEL pulse can be detected like the temporal shape of the HCP by free-space electro-optic sampling. In the case of the electro-optic sampling technique described in section 2.2.3 the temporal waveform is constructed by a sequential plot of the signal versus the time delay. The femtosecond probe pulse and the femtosecond pulse, used to generate the HCP were split off from the same femtosecond laser. Therefore no jitter existed between the probe pulse and HCP pulse. However in the case of the FEL laser, the probe pulse originates from a different laser. The jitter between the FEL laser and femtosecond probe pulse is $\sim$ 400 fs, one optical FEL cycle [70]. A single shot measurement is necessary. Instead of using a mechanical translation stage to scan the timeprofile of the pulse, a linearly chirped probe beam is used [71–73]. The temporal waveform of a copropagating FEL pulse is recorded on the spectrum profile of the optical probe beam. In this setup we can not use a quarter waveplate to increase Γ_0 because the background induced by the phase shift, will damage our array detector. Since $\Gamma << 1$ and $\Gamma_0 << 1$ [53,54], the light transmitted through the polarizer can be described by Eq. 2.5. In principle $|2\Gamma_0| > |\Gamma|$, so the intensity is linear with Γ, i.e. the electric field of the FEL pulse [53]. When Γ would be comparable to Γ_0, I is no longer linear with the electric field of the FEL pulse anymore.

In Figure 2.8 the single shot electro optical sampling technique is shown. We used a 5 mm thick ZincTelluride (ZnTe) crystal as a compromise between signal intensity and time-resolution. The FEL pulse was focused by a parabolic mirror and polarized parallel to an optical axis of the crystal. The probe pulse was frequency chirped in time by a stretcher. The stretcher is an optical setup where the optical pathlength (and hence, the transition time) depends on the wavelength. The probe beam is sent onto the grating, which disperses the laser beam. The dispersed beam propagates towards the lens and is then focused onto a mirror. After reflecting of the mirror the beam is collimated and diffracted again on the grating. This completes the first pass through the stretcher. The retroreflector (RR) changes the height of the probe beam and sends the probe beam back for the second pass through the stretcher to compensate for spatial chirp.

The probe pulse, polarized on an angle of $\sim 45^\circ$ with respect to the optical axis of the crystal, was brought in collinear with the FEL pulse by passing the probe pulse through a small hole drilled in the surface of the mirror. Both the probe pulse and the FEL pulse were focussed on the ZnTe crystal. When the chirped probe pulse and the few cycle pulse copropagate in the ZnTe crystal, the polarization of different wavelength components of the chirped pulse is rotated by a different magnitude depending on the electric field of the FEL pulse through the Pockels effect. The degree and direction of rotation is proportional to the FEL field strength and polarity. After the crystal the polarization modulation is converted to an amplitude modulation by passing a polarizer which is crossed with the initial polarization of the probe beam. In [54] Jiang and coworkers showed that there is an optimal value for Γ_0 in a crossed polarizer electro-optical sampling geometry. At this position electro-optic sampling has the largest modulation depth. We noticed that the same effect could be reached by putting the polarizers not perfectly crossed.

A home built spectrometer was used to disperse and focus the probe beam on an array detector. By measuring the spectrum of the chirped probe beam the temporal shape of the few cycle pulse is determined. The temporal resolution is determined by the chirp rate of the femtosecond probe pulse, i.e. chirped pulse length and spectrum of the chirped probe beam, and the spectral resolution of the detection system, i.e. the resolution of the home built spectrometer [73]. A larger chirp rate provides a better temporal resolution. The chirp rate is limited by the laser bandwidth and the duration of the detected part of the FEL pulse, i.e. the time window of the measurement. A better temporal resolution, requires a larger chirp rate. In principle, a wider bandwidth can support a larger chirp rate for the same time window. However, the trade-off is that a probe beam with a larger bandwidth could have a large group velocity mismatch, which reduces the temporal resolution. In Fig. 2.9a the group velocity of the probe pulse in GaAs is drawn as a function of the wavelength. The dotted line shows the phase velocity for radiation of 130 μm in GaAs ($n = 3.262$). The duration of one FEL electric field oscillation is 0.43 ps for 130 μm. The mean wavelength of the probe pulse was ~ 791 nm with a bandwidth of 30-35 nm, see solid

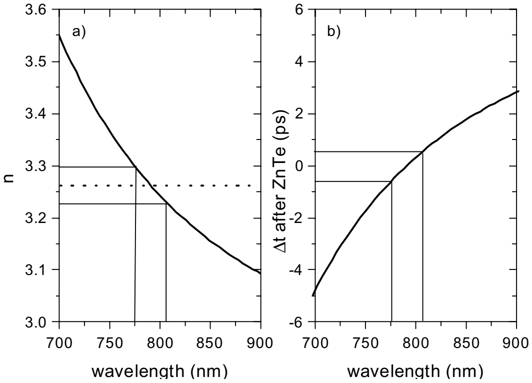

Figure 2.9: *In Fig. a) the group velocity for wavelengths in the near infrared regime is shown. The dotted line indicates the phase velocity of the FEL pulse. The velocity mismatch between the femtosecond probe pulse and the FEL pulse induces a time difference after the 0.5 cm thick ZnTe crystal. This time difference is shown in b) as a function of the wavelength. The solid lines mark the spectrum of the femtosecond oscillator. Notice that the duration of one FEL electric field oscillation is 0.43 ps for 130 μm.*

lines. The phase velocity of the FEL pulse matches exactly with the group velocity of the probe pulse near 793 nm. At smaller and larger wavelengths the difference in travelling time between the pump and probe beam through a 5 mm thick ZnTe increases. Therefore, the response of the probe pulse will be averaged over a part of the electric field. When the time difference becomes equal to the duration of one electric field oscillation the response of the probe pulse will be zero. The time difference taking into account the length of the ZnTe crystal is shown in Fig. 2.9b. When the time difference becomes equal to the duration of one electric field oscillation the response of the probe pulse will be zero. In our case the response will be maximum near the centre of the probe spectrum and minimal at the edges. This effect is, however, less pronounced than one might conclude from Fig. 2.9b. Cai *et al.* [74] already stated that the effective interaction length is determined by the corresponding depth of focus of the modulation beam, the FEL beam. Assuming a Gaussian beamprofile, we estimated the depth of focus of the FEL beam, taken as two times the Rayleigh length, to be 8 mm. Due to multi modes in the FEL beam, the depth of focus can become shorter. The FEL beam and probe beam enter the crystal under a small angle, which can also reduce the effective interaction length. We estimated that the overlap region between the two foci was approximately 3 mm.

The detection of the modulated chirped laser pulse is performed with a home built spectrometer and a CCD camera. The resolving power of the CCD array was the limiting factor of the resolution of the home built spectrometer. The lens before the CCD array was chosen such that the CCD array was covered completely by the bandwidth of the laser. The resolving power of the grating was matched with the resolving power of the CCD array detector. The resolving power of the CCD array detector is defined as

$$R \equiv \lambda/\Delta\lambda, \tag{2.18}$$

with λ the central wavelength of the probe beam and $\Delta\lambda$ the difference in wavelength that can be distinguished. The difference in wavelength that can be distinguished by the CCD array detector was limited by the number of pixels of the array detector (385 pixels). The resolving power of the grating operated in the first order is given by

$$R = N, \tag{2.19}$$

with N the amount of illuminated grooves. The amount of illuminated slits N was determined by the telescope in the beginning of the home built spectrometer. Another limiting factor for the resolution of the home built spectrometer is the entrance slit in the telescope. The size of the entrance slit determines the number of pixels illuminated by a laser beam with a very narrow spectrum. The pixel size was 22 μm. Measurements with a Helium-Neon laser showed that a single wavelength covered 5 pixels of our CCD array for the smallest possible entrance slit (~ 100 μm).

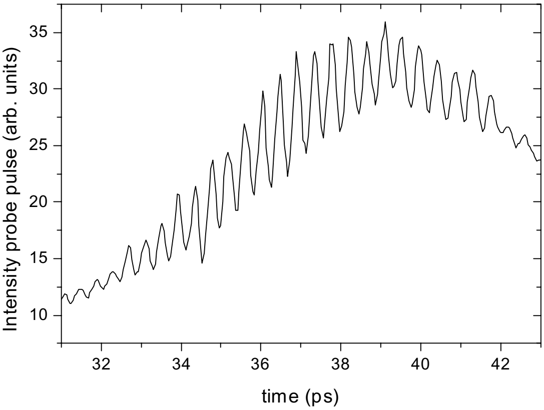

Figure 2.10: *Raw data of a single shot electro-optical measurement of a part of the FEL micropulse. The temporal profile of the FEL micropulse was recorded on the spectrum profile of the chirped femtosecond pulse. The frequency axis has been converted to a time axis.*

2.4.5 Results and Discussion

In Fig. 2.10 the raw data of a single shot electro-optical measurement are shown. A part of the temporal profile of an unsliced FEL micropulse was recorded on the frequency profile of the probe pulse. The background was caused by imperfections of the polarizers and femtosecond light scattered in the ZnTe crystal. The frequency axis has been converted into a time axis. The FWHM of the chirped pulse was about 10 ps, which corresponds with 23 oscillations in the detected spectrum. The duration of one FEL electric field oscillation is 0.43 ps for 130 μm. Fig. 2.10 shows that one oscillation in the detected spectrum corresponds with one electric field oscillation of the FEL micropulse. Measuring the signal height as function of the FEL electric field strength showed that the signal changes linearly with the electric field strength, which means that in Eq. 2.5 $\Gamma_0 > \Gamma$. The sensitivity at the edges of the frequency spectrum of the probe pulse is weak. The response of the detection system scales linearly with the intensity of the probe beam, which is low at the edges of the spectrum. The phase velocity of the FEL pulse and the group velocity of the femtosecond pulse ($\lambda = 791$ nm and $\Delta\lambda = 30$-35 nm) differ, see Fig. 2.9. When the time difference becomes equal to duration of one electric field oscillation the response of the probe pulse will be zero. A sudden decrease in signal is observed near $\sim$ 32.5 ps and $\sim$ 42 ps in Fig. 2.10. This corresponds with an effective interaction length of roughly 2 - 4 mm. To reconstruct the real FEL time profile, the oscillations have to be extracted from the

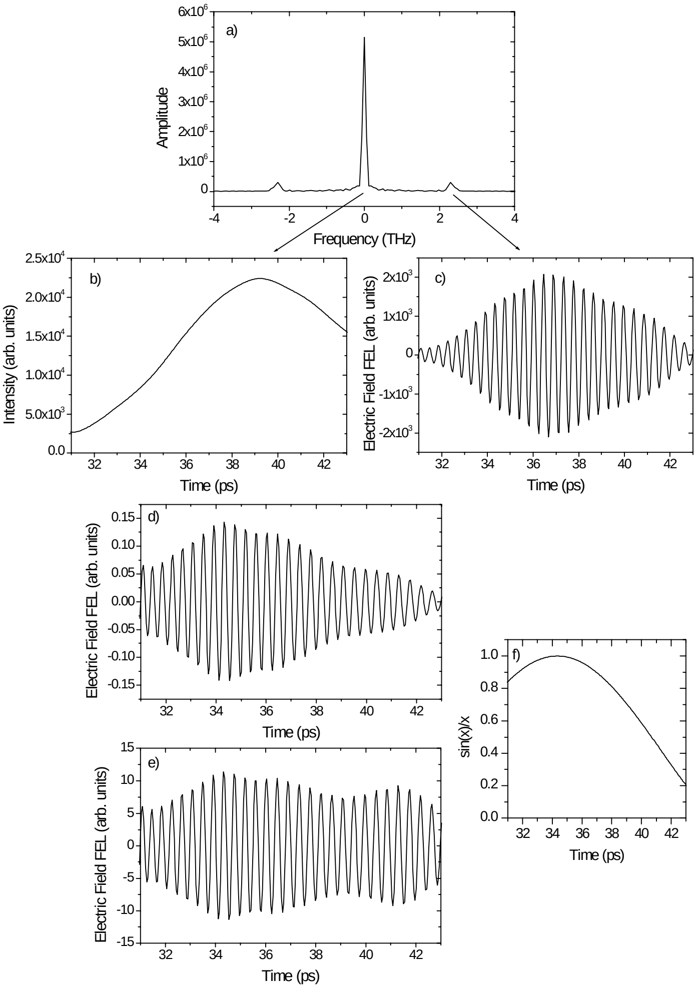

Figure 2.11: *In this plot the succesive steps are shown to derive the timeprofile of the electric field of the FEL micropulse from the raw data. a) The raw data in Fig. 8 are first Fourier transformed. b) The slow component gives, after inverse Fourier transformation, the timeprofile of the femtosecond pulse and c) the fast component the timeprofile of the FEL pulse. The time is set to zero at the beginning of the micropulse. d) The amplitude is corrected for the intensity dependence of the detecion system by dividing plot c) by b). e) The amplitude is further corrected for the velocity mismatch between pumb and probe beam in the crystal by dividing plot d) by f).*

background and the amplitude of the oscillations has to be corrected for the intensity distribution in the femtosecond spectrum and the velocity mismatch in the ZnTe crystal. First a constant background is substracted which is measured when both the probe beam and the FEL laser are blocked. To separate the background from the FEL oscillations and at the same time determine the intensity of the femtosecond spectrum, the data are Fourier transformed. Fig. 2.11a shows the amplitude of the Fourier transform of the raw data in Fig. 2.10 as a function of the frequency. The Fourier spectrum exists out of a slow component near zero frequency from the background femtosecond spectrum and a fast component near 2.3 THz from the time profile of the FEL micropulse. By inverse Fourier transformation of the slow and fast component the timeprofile of the probe beam (Fig. 2.11b) and the FEL micropulse, respectively, (Fig. 2.11c) are reconstructed. The slow or fast component can be selected for example by multiplication with a Gaussian function. With this method fast changes in the electric field signal are smeared out. A simulation with a sine function which has a sudden decrease in amplitude of 80% (within one oscillation), shows that this way of data processing smooths the signal over two oscillations. To compensate for the detection sensitivity on the intensity modulation of the probe beam the FEL time profile is divided by the intensity profile of the femtosecond spectrum, i.e. the inverse Fourier transform of the slow component (Fig. 2.11d). Finally to compensate for the velocity mismatch between the probe and pump pulse in the ZnTe crystal the FEL time profile is divided by

$$\frac{\sin(\pi\frac{t-t_0}{\Delta t})}{\pi\frac{t-t_0}{\Delta t}}, \tag{2.20}$$

where t_0 corresponds with the time where the groupvelocity of the femtosecond probe pulse is equal to the phase velocity of the FEL pulse and Δt corresponds with the time range where the time difference after the ZnTe crystal is equal to the duration of one electric field oscillation (0.43 ps). This function, shown in Fig. 2.11f, illustrates the influence of the velocity mismatch between pump and probe. If the travelling time between pump and probe is equal to one oscillation then the detection response will be zero. The larger the velocity mismatch the lower the averaged signal. Due to geometric characteristics of the FEL beam the focus length, i.e. the effective interaction length of the detection system, is hard to determine. Also the spectrum of the chirped probe beam was not well known. Therefore the variables t_0 and Δt, were fitted to give the best reliable FEL time profile, which is assumed to be constant since the FEL pulse is much longer than the time window. Notice that Eq. 2.20 is an approximation to describe the influence of the velocity mismatch. The exact groupvelocity per frequency is not taken into account. The best fits were found for an effective interaction length between 1.7 mm and 2.4 mm. In Fig. 2.12 the measured time profile of the electric field of the entire FEL micropulse is shown. The full micropulse could be recorded by moving the measurable time window, i.e. the chirped femtosecond pulse, over the FEL micropulse. The overlap of the time windows

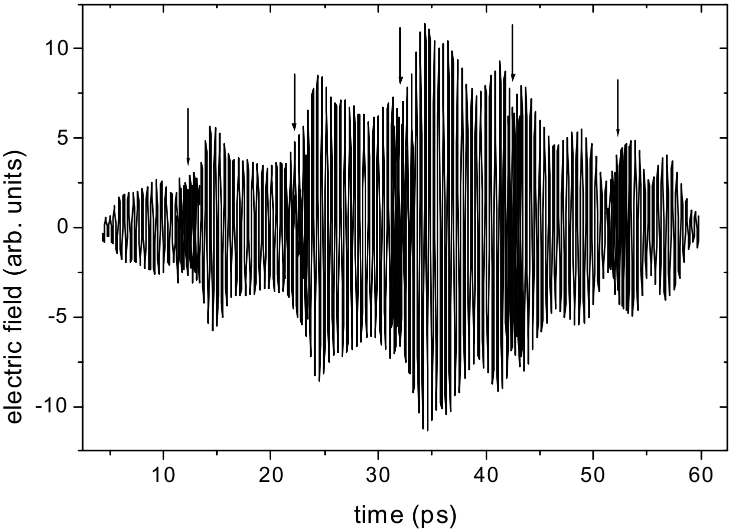

Figure 2.12: *Time profile of the electric field of the entire FEL micropulse. The arrows show the overlap of the individual measurable time windows.*

is shown by the arrows. We expected a smooth exponential rising pulse [75, 76], but Fig. 2.12 shows some oscillations on top of the electric field time profile. This oscillation pattern is repeated in every time window. Probably there are some other minor influences on the sensitivity of the detection method, which depend on the frequency of the probe pulse, i.e. Γ_0 can be wavelength dependent.

In a first attempt to create few cycle pulses we only sliced the back side of the FEL micropulse, i.e. we only used the transmission (second) wafer in Fig. 2.7. The reflection (first) wafer was replaced by a mirror. The raw data (divided by the femtosecond intensity spectrum) are shown in Fig. 2.13. The upper plot is the plot of an entire unsliced FEL, which is repeated below the sliced pulses. The slicing place is changed by varying the delay between the FEL pulse and the femtosecond slice pulse. The arrows indicate the place were the femtosecond beam sliced the FEL micropulse, i.e. the first oscillation after the slicing, which has a lower amplitude then the same oscillation in the main FEL micropulse. The decrease in amplitude at the moment of slicing is clearly visible. Although the amplitude of the oscillations after the slicing point fluctuates, no oscillations regain the value of the unsliced pulse.

In Figs. 2.14a and 2.14b reconstructions of the temporal oscillating electric field of sliced FEL beams together with the fundamental FEL pulse are shown for two different datasets. The oscillating electric field was reconstructed according to the

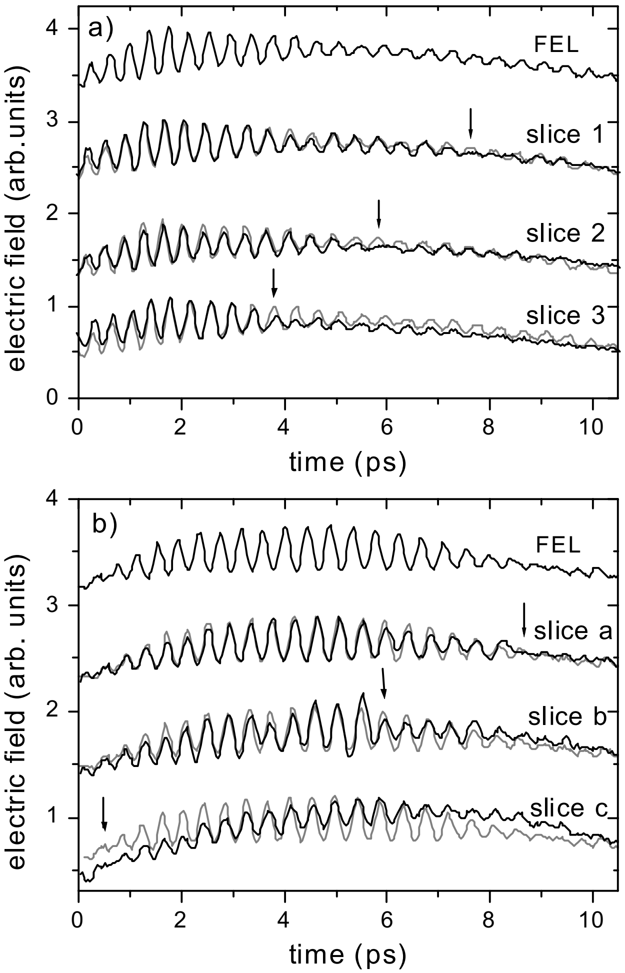

Figure 2.13: *In this figure the raw data of sliced FEL micropulses are shown for two different datasets. The upper plot shows the original FEL pulse. For reference this curve is repeated below the sliced pulses (grey). The data has been divided by the femtosecond intensity spectrum to compensate for the detection sensitivity on the intensity modulation of the probe beam. The arrows indicate the place were the femtosecond beam sliced the FEL micropulse.*

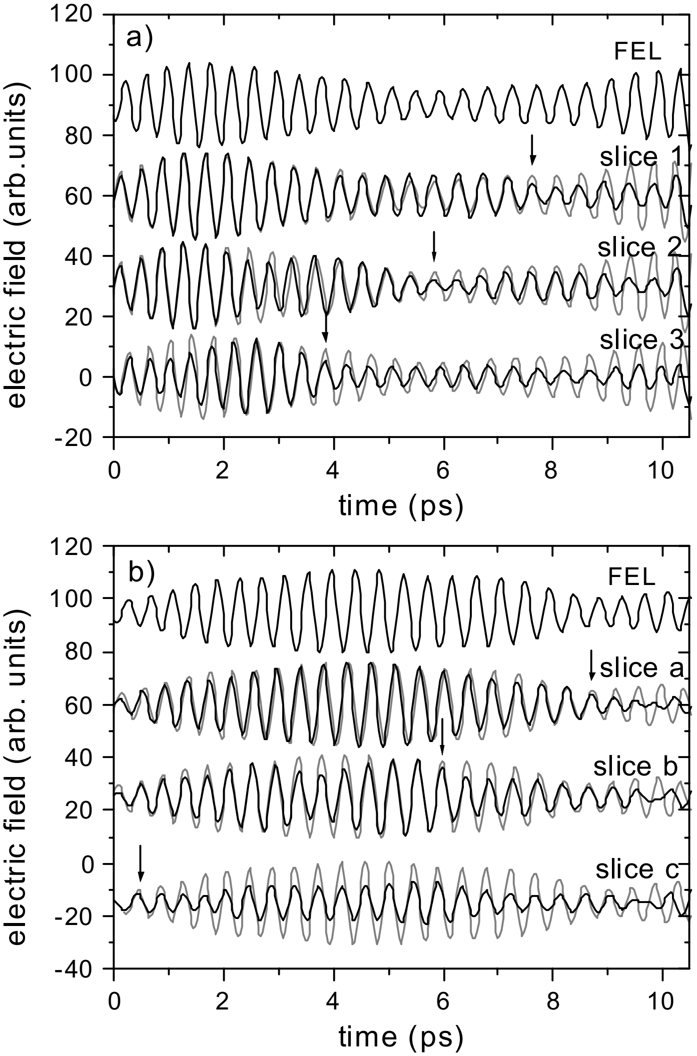

Figure 2.14: *Measured time profile of the electric field of sliced FEL micropulses for two different datasets. The arrows indicate the place of slicing. The data shown were treated as described in Fig. 2.11.*

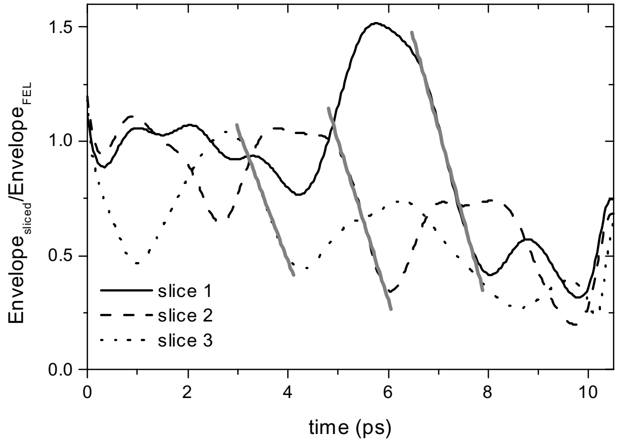

Figure 2.15: *The envelope of the sliced FEL pulse is divided by the envelope of the FEL micropulse to determine the rise/decay time of the sliced pulse. The decay could be fitted by a linear function (gray solid lines).*

method described in Fig. 2.11. The upper plot in both graphs is the plot of an entire unsliced FEL micropulse. The arrows indicate the place were the femtosecond beam sliced the FEL micropulse. In Fig. 2.14b the change in delay between the corresponding data was measured experimentally; between slice a and b 2.7 ps, and between slice b and c 5.3 ps. Taking into account an oscillation time of 0.43 ps, this corresponds with respectively 6 and 12 electric field oscillations. These number of oscillations we observe between slice a and b, and slice b and c in Fig. 2.14b. To determine the decay time of the sliced FEL pulse, we divided the envelope of the electric field of the FEL micropulse by the envelope of the electric field of the sliced FEL pulse, see Fig. 2.15. This figure shows that the amplitude of the FEL pulse drops significantly immediately after the slicing point. As was already obvious from the raw data of Fig. 2.13 and the analyzed data of Fig. 2.14, the amplitude does not drop to zero as in the case of an ideal switch. We only reduce the electric field to 50%, thus a factor of four reduction in intensity. The steep decrease in Fig. 2.15 can be fitted with a linear decrease from 100% to 50% in 0.72 ps, in two electric field oscillations. It should be realized that this time is close to the minimum switching time that can result from our acquisition method that is based on making selections in frequency space during the analysis. Hence slicing can take place faster than two oscillations. A qualitative look at the results in Figs. 2.13 and 2.14 suggest that the switching time is more or less instantaneous on the time scale of the 0.43 ps FEL oscillation time.

The analysis given earlier suggested that upon illumination of the GaAs wafer with the femtosecond pulse the reflection coefficient should have risen to almost unity. In the experiment the electric field is reduced to 50% instead of near zero. An explanation may be that the overlap between the FEL beam and the femtosecond pulse is not optimized. If the focus of the FEL laser is larger then the beam of the slicing laser the outer part of the FEL pulse would not be sliced, but still transmitted through the wafer, increasing the background. Increasing the overlap between the two beams would decrease the background.

The data contains also further structure. A weak oscillation pattern of about 3 ps on the envelope is observed. Figures 2.13-2.15 show the result of the analysis of a single shot. The method is accompanied by shot-to-shot fluctuations of 20% in each trace, which however do not provide an explanation of the very regular behavior. Below several possible explanations for this regular oscillation pattern are described.

The first reason for these oscillations maybe experimental in nature. In the present method a chirped pulse is used to map instantaneous frequency onto a time axis. As has been explained by Fletcher [77], this method may result in spurious signals when changes in the signal are too fast in relation to the chirp rate.

A second reason maybe the dynamics and properties of the photo-excited electrons and holes. The dynamics and properties of the photo-excited electrons and holes determines the reflection and transmission characteristics of the GaAs wafer. It is known that upon the initial excitation, hot charge carriers are formed that subsequently relax by inelastic processes to the bottom of the conduction band. On a much longer time scale, the electrons relax back to the valence band, transforming the conductor into an insulator again. Other dynamic properties excited by the slicing pulse in the wafer are excitation of phonon modes. It is tempting to attribute the oscillation pattern on top of the FEL pulse to the dynamics of electron relaxation or phonon excitation processes. Phonon excitation would lead to the emission or absorption of light, which should be visible in the Fourier transform of the sliced FEL pulse. Emission would lead to an extra peak in the Fourier spectrum and absorption to a dip, i.e. a missing frequency, in the Fourier spectrum. Comparing the Fourier spectra of the unsliced FEL micropulse with the sliced FEL pulse no clear peak or dip is observed.

The switching of the mirror is performed via the illumination of the unbiased GaAs wafer. Most semiconductor surfaces have occupied surface states. These surface states bend both the conduction band and valence band near the surface forming a charge depletion layer and thus a built-in surface electric field. The built-in static field drives the two kinds of carriers, electrons and holes, in opposite directions. This mechanism may turn our switchable mirror into a source of fast HCP generation. This half-cycle pulse would interfere with the FEL micropulse. But the observed oscillation pattern is not easy to explain with this mechanism.

The occurrence of weak pre- and post-pulses out of the femtosecond laser may have result in the modulation of the charge carriers and hence the reflection characteristics. But this oscillation pattern could only be explained as the reflection of hot electrons is higher than cold electrons. The prepulse generates hot electrons and the wafer becomes reflective. As the electrons cool down the reflectivity decreases back to zero. When the main pulse comes enough free carriers are created that even cold electrons make the wafer reflective. But Nuss *et al.* [66] showed that the mobility of the electrons (and hence the reflectivity of the wafer) increases when the electrons cool towards the bottom of the conduction band.

In the far field the electric field of the emitted radiation has to average out to zero. Suppose that not an integer number of cycles is cut, than the pulse has to change its shape to full fill the condition of zero energy in the far field. But we would expect a kind of ringing at the end of the sliced pulse, just like the tail of a HCP.

In conclusion, GaAs is a good candidate to be a very fast and efficient switchable mirror in the far infrared regime. In our experiment, we have found a very fast response, faster than 0.8 ps. It was found that the reflectivity was not switched to unity, finite transmission was observed under all conditions. A more serious drawback for a general application of this method for the generation of few cycle radiation is the apparent of an oscillation pattern on top of the sliced FEL pulse. At this point it is not known wether this signal is due to signal generated by the wafer or that it is a consequence of dynamics inherent to the GaAs material properties.

Chapter 3

The Dynamics of a THz Rydberg Wavepacket

An optically excited Rydberg wavepacket can be generated by exciting the electron from a low-lying state to a coherent superposition of high-lying states with a short broadband optical pulse. A special kind of Rydberg wavepacket is generated in the case of an interaction of a weak THz half-cycle pulse with a stationary Rydberg State, called the THz wavepacket . This THz wavepacket is a coherent superposition of the initial Rydberg state and its neighbouring states. We have investigated the time evolution of THz wavepackets by measuring the impact of two in time delayed half-cycle pulses ($\sim 200\ Vcm^{-1}$) *on the population of a stationary* ($n = 40$) *Rydberg state in rubidium. The first half-cycle pulse creates the THz wavepacket and the second half-cycle pulse probes the dynamics of the THz wavepacket. We support our experimental data by numerically solving the Schrödinger equation and with a semi-classical picture. Whereas an optically excited wavepacket is initially localized, a THz wavepacket is initially delocalized and becomes localized after half a revival time.*

3.1 Introduction

In recent years it has become possible to generate very short freely propagating electrical pulses of half a cycle with a frequency spectrum in the THz regime, often referred to as THz half-cycle pulses (HCP) [41–43]. In several experiments the influence of such a HCP on ionization of Rydberg atoms has been investigated [15, 25, 29, 79]. If the pulse duration of these HCP is very short compared to the Kepler roundtrip time of a Rydberg electron, the impact of a HCP can be described as a momentum kick

$$\Delta\mathbf{p} = -\int \mathbf{E}_{HCP}(t)dt \tag{3.1}$$

to the Rydberg electron where $\mathbf{E}_{HCP}(t)$ is the electric field of the HCP [15,79]. In the limit that the pulse is much shorter than the orbit time the resulting energy transfer is given by

$$\Delta E = \mathbf{p}_0 \cdot \Delta\mathbf{p} + \Delta p^2/2, \tag{3.2}$$

where $\mathbf{p}_0$ is the initial momentum of the electron. The net energy change will thus depend on the initial momentum of the electron and the direction of the kick.

HCP have been used to probe the dynamics of a Rydberg wavepacket [22,23,80,81]. An optically excited Rydberg wavepacket can be generated by exciting the electron from a low-lying atomic state to a coherent superposition of n states with a short optical pulse [5, 7, 82, 83]. In order to conserve momentum, optical excitation takes place only near the nucleus; a radially localized Rydberg wavepacket is created [7]. The localized Rydberg wavepacket oscillates in and out about the nucleus with an oscillation period matching the classical period of an electron in a Kepler orbit. The Kepler period is given by the inverse of the energy spacing between the excited n-manifolds ($\tau_{Kepler} = 2\pi\overline{n}^3$). The long-term evolution of the wavepacket is more complex. The Rydberg states are nearly equally spaced. The deviation from the harmonic spacing causes the wavepacket to spread slowly and in course of time the wavepacket is no longer localized. The spreading is smooth along the orbit until the tail of the wavepacket meets with its head. At this point a new interference pattern begins to form and small wavepackets emerge. This fractional periodicity is called fractional revival. The quadratic regularity of the spacing difference results in a rephasing of the states and the wavepacket becomes localized at $\tau_{revival} = \frac{\overline{n}}{3}\tau_{Kepler}$. At $\frac{1}{2}\tau_{revival}$ the odd and even states are in phase and the wavepacket is broken up into two discrete wavepacket parts. Only a small fraction of the population is excited from the initial state ($n = i$) towards higher lying Rydberg states (n), where n is the principal quantum number

$$\Psi = a_i\psi_i + \sum_n b_n\psi_n; \qquad \sum_n |b_n|^2 << 1. \tag{3.3}$$

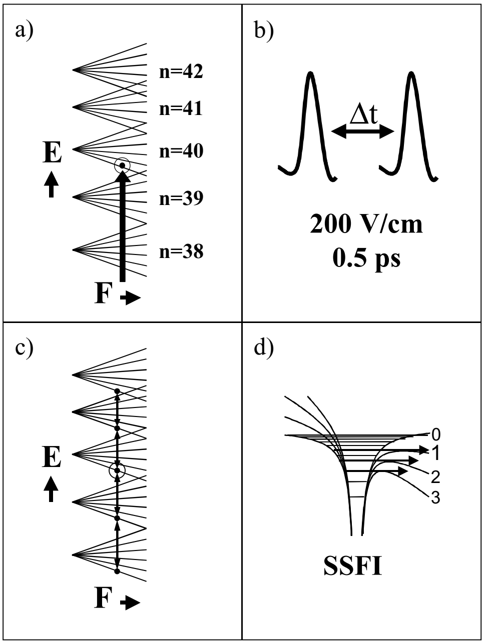

Figure 3.1: *Schematic illustration of the experiment. a) Rubidium atoms are laser excited in a static electric field from the ground state to the lower, red, Stark states of the* $n = 40$ *manifold; the initial Rydberg state. b) Two HCP kick against the Rydberg electron and change the energy of the electron. The first HCP creates the THz wavepacket and the second probes the dynamics. The delay between the HCP is varied in the experiment. c) The electron population is redistributed over neighbouring manifolds by the HCP. d) After the exposure to the THz radiation the final state distribution of the Rydberg atoms was measured by state selective field ionization.*

After the excitation the remaining initial state amplitude ($a_i \psi_i$) is ignored.

A coherent superposition of Rydberg states can also be generated with a HCP [9,10,84]. In the case of a strong HCP, where the term Δp^2 in equation 3.2 dominates, the Rydberg wavepacket is generated by exciting the electron population from a initial low lying state to a superposition of high-lying n states. For small momentum kicks, i.e. weak HCP, the second term $\Delta p^2/2$ in equation 3.2 can be neglected. Starting from the initial Rydberg state n$_i$ the net energy transfer (ΔE) can be both positive ($n > n_i$) and negative ($n < n_i$), and the electron population will be spread over neighbouring manifolds, generating a special kind of Rydberg wavepacket, which we will call THz wavepacket. This THz Rydberg wavepacket is a superposition of the initial state and its neighbouring states

$$\Psi = \sum_n a_n \psi_n; \qquad \sum_n |a_n|^2 = 1. \tag{3.4}$$

Unlike a short optical pulse, the HCP changes the energy of a free electron. Therefore, the electron can increase (or decrease) its energy at any distance from the nucleus, except close to the core. Close to the core the electron changes its direction while the pulse is on. However, this is a small fraction of the wave function. Excitation happens over the full orbit; a delocalized Rydberg Wavepacket is created.

We want to investigate the dynamics of this THz wavepackets by comparing the time evolution of the population transferred in the lower-lying neighbouring manifolds ($\Delta E < 0$) with the time evolution of the population in the higher-lying neighbouring manifolds ($\Delta E > 0$) after exposure to a probe HCP. We describe the time evolution of a THz Rydberg wavepacket with a semi-classical picture. A schematic representation of the experiment is given in Fig. 3.1. Rubidium atoms are excited in a static electric field from the ground state to the lower, red, Stark states of manifold $n = 40$ with a nanosecond dye laser. Two HCP are generated by illuminating biased GaAs wafers with a femtosecond Ti:sapphire laser. The first HCP creates a wavepacket and the second HCP is used to probe the dynamics of the wavepacket. The two pulses are delayed in time by a variable delay line in the optical beam. The interaction with the two HCP will change the energy of the electron hence the electron population will redistribute over the neighbouring manifolds. The final state distribution of the Rydberg atoms as a function of the delay between the two HCP is measured by state selective field ionization. The experimental setup is described in section 3.2. The final state distribution is also calculated by numerical integration of the Schrödinger equation. The theoretical and experimental data are presented and compared in section 3.3. The results are explained with a semi-classical interpretation in section 3.4.

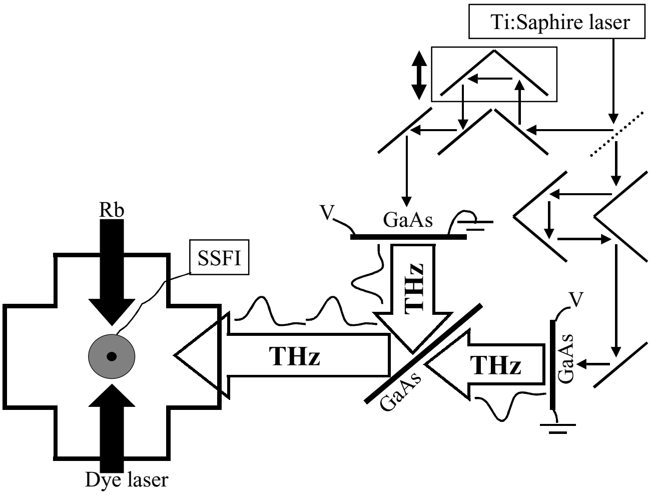

Figure 3.2: *Schematic representation of the experimental setup (for details see text).*

3.2 Experimental Setup

The dynamics of a THz wavepacket are investigated by measuring the influence of two HCP on highly excited Rydberg atoms is investigated as a function of the delay between the two HCP. In Fig. 3.2 the experimental setup is shown. Inside a vacuum chamber rubidium was evaporated in a resistively heated oven. Highly excited Rydberg atoms ($n = 40$) were created in a static electric field of 10 Vcm^{-1} by two photon excitation ($\lambda = 594.870$ nm) of ground-state rubidium atoms using a Nd:YAG pumped dye laser. The static electric field was strong enough to mix the 41d state with the lower, red, Stark states of the $n = 40$ manifold, but too weak to reach the n-mixing regime. Two HCP were created by illuminating biased ($\sim$ 1 kV) GaAs wafers with $\sim$ 75 fs, 795 nm pulses ($\sim$ 0.1 mJ) from a Ti:sapphire laser. The electric field of the two HCP in the interaction region, separated by 50 cm from the GaAs wafers, was estimated to be $100 - 300$ Vcm^{-1}. The polarization of the HCP was chosen parallel to the static electric field. The polarity of the HCP (either in the $+z$-direction or $-z$-direction) could be altered by changing the polarity of the bias over the wafers. The two pulses were delayed in time by a variable delay line in the optical beam. A third, unbiased, GaAs wafer was used as a beamsplitter to overlap the two HCP in space. The HCP were polarized perpendicular to the plane of incidence (s polarization). The point of overlap of the two HCP in time was determined within 0.5 mm exactly by colinear overlap of the two optical femtosecond beams. Fringes in the

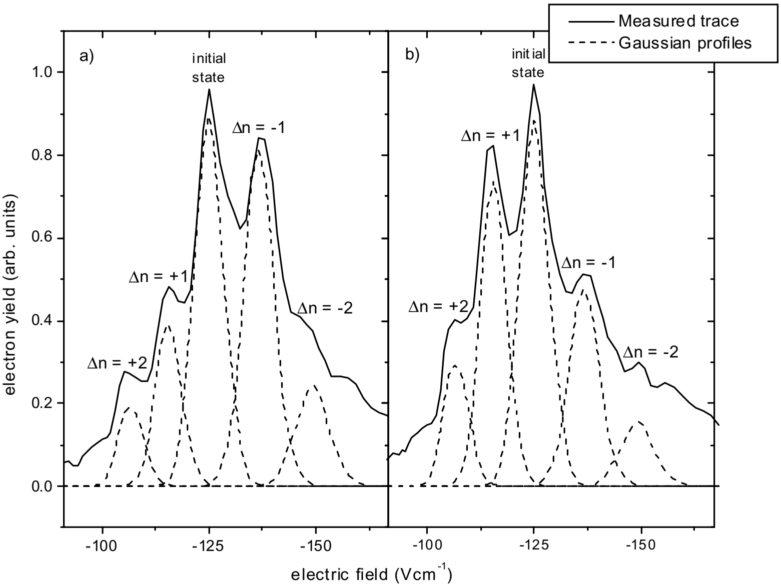

Figure 3.3: *Measured SSFI traces (straight line) at two different delays between the HCP. In figure a) the initial population is transferred to higher-lying, neighbouring Rydberg states, and in figure b) to lower-lying, neighbouring Rydberg states. The dashed lines are the Gaussian profiles fitted to the relevant states involved in the wavepacket.*

optical beams indicated the overlap in time. After the exposure to the THz radiation the final state distribution of the Rydberg atoms was measured by state selective field ionization (SSFI) [16]. In time the electric field was ramped $\sim$ 200 Vcm^{-1} in 3 μs, such that the higher Rydberg states would ionize earlier in time than the lower Rydberg states. With state selective field ionization the population in every state could be measured separately. In the SSFI trace the peaks, representing single manifolds, overlapped somewhat, see Fig. 3.3. In this Fig. 3.3 the SSFI traces are shown for two different delays between the HCP. In Fig. 3.3a the initial population is transferred to higher-lying, neighbouring Rydberg states, and in Fig. 3.3b the initial population is transferred to lower-lying, neighbouring Rydberg states. The population of each state was determined by fitting a superposition of Gaussian profiles to the measured SSFI trace, see the dashed lines in Fig. 3.3.

The pulse shape of the two HCP after the GaAs beamsplitter was measured by an electro-optical sampling method, (see Fig. 3.4). The electro-optical sampling method has been described in [46–48]. Briefly, a linearly polarized femtosecond probe pulse,

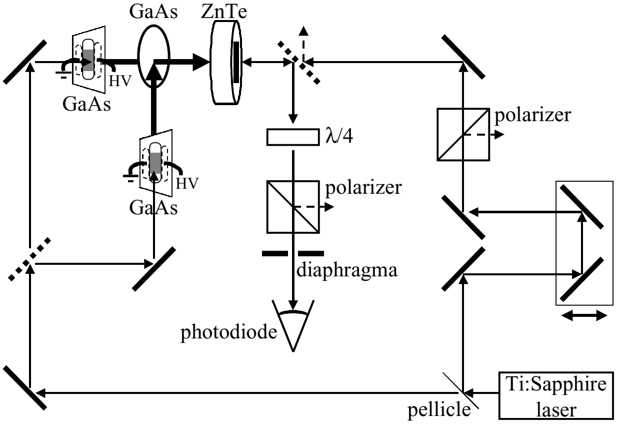
GaAs
ZnTe
HV
GaAs
λ/4
polarizer
HV
GaAs
polarizer
diaphragma
photodiode
pellicle
Ti:Sapphire laser

Figure 3.4: *Illustration of the electro-optical sampling method. The reflected and transmitted beam were detected separately.*

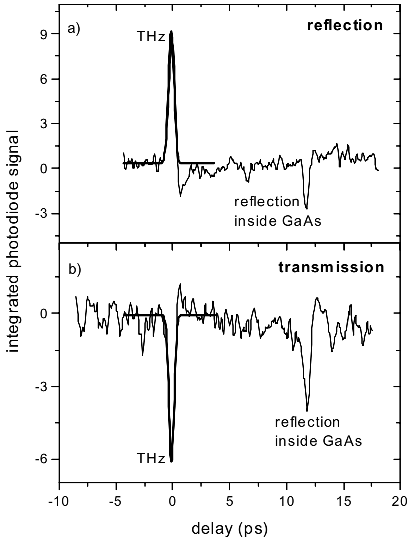

Figure 3.5: *HCP shape, measured after the GaAs beamsplitter, both a) the reflected and b) the transmitted HCP. A Gaussian pulse shape could be nicely fitted to both HCP (thick lines).*

derived from the femtosecond laser propagated collinear with the HCP pulse inside a electro-optic crystal (ZnTe) and probed the change in the index of refraction induced by the electric field of the HCP. In our experiment, the probe pulse was send into the electro-optic crystal from the back surface with respect to the direction of the incoming HCP. The duration of the probe pulse was shorter than the duration of the HCP pulse; therefore the temporal shape of the THz pulse could be measured by changing the relative delay between the THz pulse and the probe pulse while monitoring the phase retardation of the probe beam. The phase retardation was converted into an intensity modulation by passing the probe beam through a polarizer and detecting the transmission with a photodiode. The photodiode signal was integrated and averaged with a boxcar. To get a decent signal-to-noise ratio the data were averaged over ten scans. In Fig. 3.5 the HCP shapes after the GaAs beamsplitter are shown for both the transmitted HCP (Fig. 3.5a) and the reflected HCP (Fig. 3.5b). Two peaks appeared, instead of one HCP. The small peak delayed by 11.8 ps with respect to the main peak, was caused by internal reflection of the HCP in the GaAs beamsplitter. The index of refraction at THz frequencies in GaAs is 3.54 and the wafer thickness was 0.5 mm, predicting a delay of 11.9 ps. The polarity of the bias over the GaAs wafers, which generate the HCP were equal for both HCP. So the polarity of the two pulses before the GaAs beamsplitter were equal. But the polarity of the external reflection of the main HCP after the GaAs wafer was opposite to the polarity of the other three pulses. The external reflection of the HCP had flipped polarity on the GaAs beamsplitter as the Fresnel equations predict for s polarized light. A Gaussian pulse could be nicely fitted to both the main reflected and transmitted HCP. The FWHM of the reflected and transmitted HCP were respectively 0.59 ps and 0.54 ps.

3.3 Results and Discussion

3.3.1 Experimental Results

We first discuss the population remaining in the initial state after exposure to THz radiation as a function of the delay between the two HCP. The experiment was done in a static electric field of 10 Vcm^{-1}, with as initial state a red Stark state of the $n = 40$ manifold and in zero field, with the 41d state as initial state. The results of both experiments are compared. In Fig. 3.6 the fraction of the total population remaining in the initial state as a function of the delay between the two HCP is shown for parallel polarity between the pump and probe HCP. The results for the experiment performed in a static electric field are plotted in Fig. 3.6a and for the experiment performed in zero field in Fig. 3.6b. In the case of opposite polarity between the pump and probe HCP, the fast oscillations have a phase shift of π, these results are not shown. Fast oscillations appear with a period of respectively 10 ps in Fig. 3.6a and 30 ps in Fig. 3.6b. In the experiment performed in a static electric

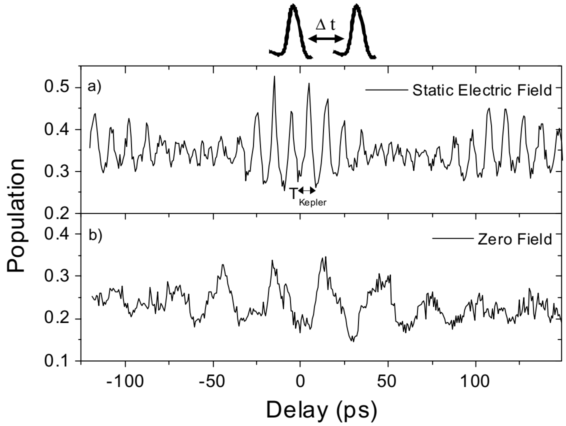

Figure 3.6: *The population in the initial state after exposure to THz radiation is shown as a function of the delay between the two HCP for a) in a static electric field and b) in zero field. The polarity of the two pulses was chosen parallel.*

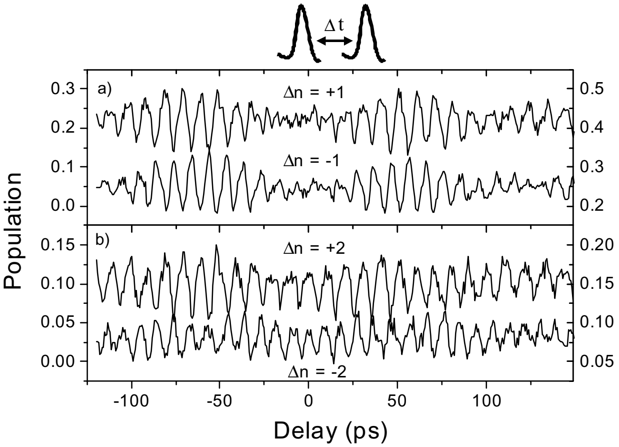

Figure 3.7: *The population of the neighbouring manifolds after the exposure of the THz radiation is presented as a function of the delay between the two HCP for a) $\Delta n = \pm 1$ and b) $\Delta n = \pm 2$. The polarity of the two pulses was chosen parallel. The states are plotted with an offset. Actually the plots overlap. The left axis shows the population for the higher-lying state and the right axis shows the population for the lower-lying state.*

field these fast oscillations equal the Kepler orbit time of the wavepacket; τ_{Kepler} = 9.7 ps. In the case of the field-free experiment the beat frequency is an average of the transition frequencies from the initial d state to neighbouring p and f states ($\Delta l = \pm 1$); 39f ($\frac{1}{22.2 \text{ ps}}$), 42p ($\frac{1}{39.2 \text{ ps}}$), 40f ($\frac{1}{31.8 \text{ ps}}$), 43p ($\frac{1}{16.8 \text{ ps}}$). The field-free result agrees with earlier observations [8]. In [8] the experiment was performed with strong HCP, so first order pertubation theory did not hold. In our case, for weak HCP only transitions are allowed when $\Delta l = \pm 1$. For weak HCP the first-order pertubation theory holds. In Fig. 3.6a, the results of the experiment performed in a static electric field, another effect is visible; the fast oscillations decay and revive again over a period of about 123 ps. This period agrees with the revival time of the wavepacket ($\tau_{revival}$ = 130 ps). For the static-electric-field experiment also the population of $\Delta n = \pm 1$ and $\Delta n = \pm 2$ have been measured as a function of the delay between the two HCP. These populations are respectively plotted in Fig. 3.7a for $\Delta n = \pm 1$ and Fig. 3.7b for $\Delta n = \pm 2$, again for parallel polarity between the pump and probe HCP. Fast oscillations, which equal the Kepler orbit time of the electron are visible. For $\Delta n = \pm 1$ these fast oscillations are out of phase at $\frac{1}{2}\tau_{revival}$. For $\Delta n = \pm 2$ the oscillations are in phase at zero delay, then get out of phase at $\frac{1}{2}\tau_{revival}$ and again in phase at $\tau_{revival}$.

3.3.2 Theoretical Description

The final state distribution for the static-electric-field case was also calculated by numerical integration of the Schrödinger equation. Starting in a stationary, highly excited Rydberg Stark state, two, in time delayed, HCP drive the initial state population to neighbouring states. The population redistribution as a function of the delay can be calculated by numerical integration of the Schrödinger equation:

$$\frac{\partial}{\partial t}\Psi(t) = -iH\Psi(t). \tag{3.5}$$

To simplify the problem we numerically solved equation 3.5 for the case of a hydrogen atom. In that case the Hamiltonian, H, in a pertubative electric field is:

$$H = -\frac{p^2}{2} - \frac{1}{r} + E(t)z. \tag{3.6}$$

The pertubation $E(t)$ is given by the electric field of the two HCP. We assume the HCP to be Gaussian in shape and a FWHM of 0.57 ps. Incorporating the observed echo at 11.7 ps (Fig. 3.5) in the theory might further improve the model but this refinement is beyond the scope of this chapter.

The lower, red, Stark states in a manifold couple with the corresponding Stark states in the neighbouring manifolds, i.e. the lowest Stark state of a manifold couples only to the lowest Stark states of the neighbouring manifolds. Applying the approximation that initially one Stark state is excited will reduce the amount of states involved in the wavefunction ($\sum c_n\psi_n$) to the amount of manifolds involved. The basis states ψ_n are independent. This requirement produces coupled but separated equations for each c_n, which can be written in matrix form:

$$\frac{d}{dt}\mathbf{c}_n = -i\hat{H}\mathbf{c}_n. \tag{3.7}$$

The diagonal elements of the matrix $\hat{H}$ are given by the eigenenergies in zero field and the coupling to the pertubative electric field, the Stark shift Δ_n, multiplied by the pertubative electric field.

$$\hat{H}_{n,n} = \frac{1}{2n^2} + \Delta_{n,k}E(t); \qquad \Delta_{n,k} = \frac{3}{2}nk. \tag{3.8}$$

The off-diagonal elements describe the coupling between the neighbouring states and are given by the semiclassical approximation for transitions between hydrogenic states [85]

$$\hat{H}_{n,n'} = \frac{2}{3\Delta n}J'_{\Delta n}(\Delta n)\sqrt{\Delta_{n,k}\Delta_{n',k'}}E(t), \tag{3.9}$$

with $J'_{\Delta n}$ the derivative of the Bessel function of the first kind, order Δn, $\Delta n = n - n'$. The ratio of the coupling constant for $\Delta n = 1$ is ~ 0.2 and for $\Delta n = 2$ this is ~ 0.07. The ratio continues to fall for increasing Δn.

This first-order differential equation 3.7 is solved numerically by the fourth-order Runga Kutta integration method. Suppose the initial state in the experiment is a single Rydberg Stark state, then as initial conditions a single amplitude c_i is put equal to one and all other amplitudes $c_{n\neq i}$ are put to zero.

The theoretical results are shown in Fig. 3.8. The polarity between the two HCP was chosen parallel. The electric field of the two HCP was chosen at 200 Vcm^{-1} to get the best quantitative agreement. The population of the initial state, the lowest Stark state of $n = 40$, the population of the lowest Stark states of the $\Delta n = \pm 1$ states and of the $\Delta n = \pm 2$ states are shown respectively in Figs. 3.8a, 3.8b, 3.8c as a function of the delay between the two HCP. In the calculation also the lowest Stark states of the $\Delta n = \pm 3$ states are included to avoid boundary effects. Both in the experiment and in the calculation we found less than 4% population in the $\Delta n = \pm 3$ states. In agreement with our experimental data we observe fast oscillations (9.8 ps) equal to the Kepler orbit period. The fast oscillations in the initial state decay and revive again over the revival time of the wavepacket ($\tau_{revival} \approx 125$ ps). At zero delay the oscillations in $\Delta n = \pm 1$ are in phase, near $\frac{1}{2}\tau_{revival}$ these oscillations are out of phase and get in phase again near one revival time. These results are in agreement with the experimental observations. The oscillations in $\Delta n = \pm 2$ are in phase at zero delay and at integer multiples of $\frac{1}{2}\tau_{revival}$, in between the oscillations are out of phase. In the final population of $\Delta n = \pm 2$ fast oscillations appear with a periodicity

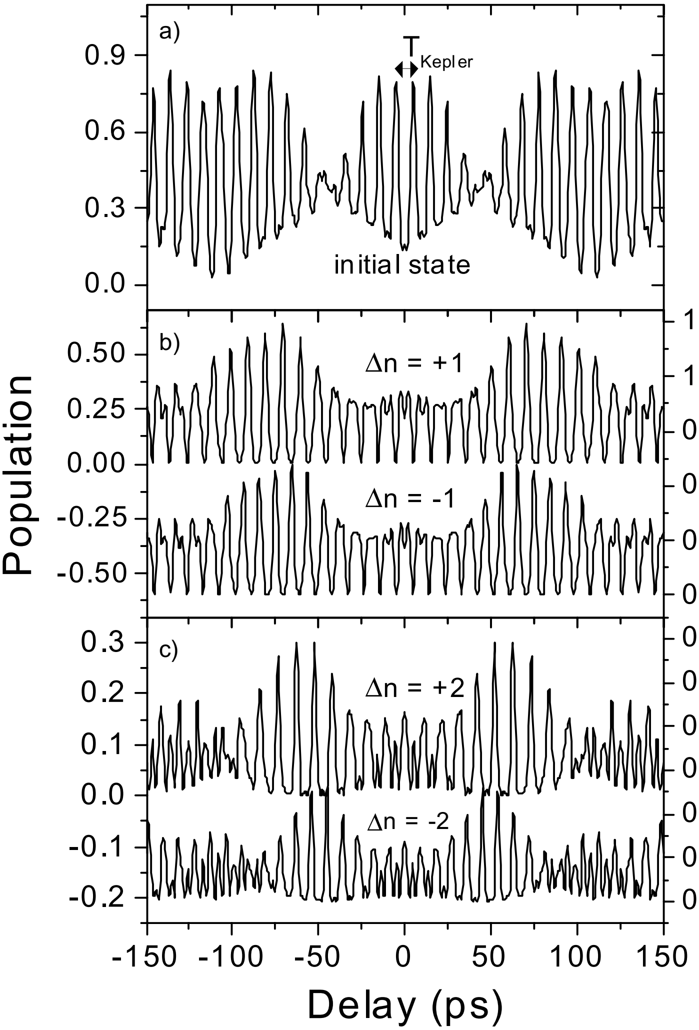

Figure 3.8: *Calculated populations shown as a function of the delay. In a) the initial state population is shown, in b) the population of* $\Delta n = \pm 1$ *and in c) the population of* $\Delta n = \pm 2$. *The polarity was chosen parallel. The higher and lower-lying state in Figs. b and c are plotted with an offset. Actually the plots overlap. The left axis shows the population for the higher-lying state and the right axis shows the population for the lower-lying state.*

of half the Kepler period ($\frac{1}{2}\tau_{Kepler}$), indicating direct, one photon, transition from the initial state to the $\Delta n = \pm 2$ states, besides the two transition steps of $\Delta n = \pm 1$. These direct $\Delta n = \pm 2$ transitions are also the reason that the oscillations in the $\Delta n = \pm 2$ states are in phase at half the revival time of the wavepacket. This does not agree with the experimental results where we observe only $\Delta n = \pm 1$ transitions. In the experimental results no indication is found for direct, one photon, transition to the $\Delta n = \pm 2$ states. The signal to noise ratio of the experiment is not sufficient to exclude any $\Delta n = 2$ one-photon transitions, but the theory clearly overestimates the contribution of this process.

In the calculations two equal HCP were used, while in the experiment the HCP might not be equal, since they were generated from different GaAs wafers. Taking this into account in the calculation, different pulse duration and electric field strength, did not improve the agreement. Small differences between the two HCP hardly affected the theoretical results, while for large differences the out and in phase time in $\Delta n = \pm 2$ became irregular. This tells us, that our two HCP are almost equal in shape. It does not give us an explanation for the difference between theory and experiment. The Fourier transform of the Gaussian HCP shows that the frequencies of both the $\Delta n = \pm 1$ transitions and $\Delta n = \pm 2$ transitions are present, indicating that both transitions should be allowed. Maybe the coupling constant for $\Delta n = \pm 2$ transitions is overestimated in the theoretical calculations. We compared the approximated matrix elements of equation 3.9 with exactly calculated matrix elements. First the eigenstates of rubidium in a static electric field of 10 Vcm^{-1} for $m = 0$ where determined. Next the coupling constants were calculated between every eigenstate. The ratios of the exactly calculated coupling constants to the coupling constant of $\Delta n = 0$ are the same as our simplified equation 3.9 predicts, namely ~ 0.2 for $\Delta n = \pm 1$ transitions and ~ 0.07 for $\Delta n = \pm 2$ transitions. This exact calculation also showed that lower, red, Stark states couple with the corresponding Stark states in the neighbouring manifolds, as already mentioned in the beginning of this section. In the experiment the bandwidth of the dye laser was not small enough to excite one Stark state, probably several Stark states were excited. Taking this into account in our theoretical calculation by defining the final state populations as a summation over several Stark states, did not improve the agreement. In conclusion our experimental and theoretical results agree, except for the direct $\Delta n = \pm 2$ transitions. The importance of these transitions as indicated by the theory is not confirmed in the experiment.

3.4 Semi-Classical Interpretation

3.4.1 Semi-Classical Picture

In this section we present an intuitive semi-classical picture to explain the measured and calculated results, illustrated in Fig. 3.9. Let us describe the initial Rydberg

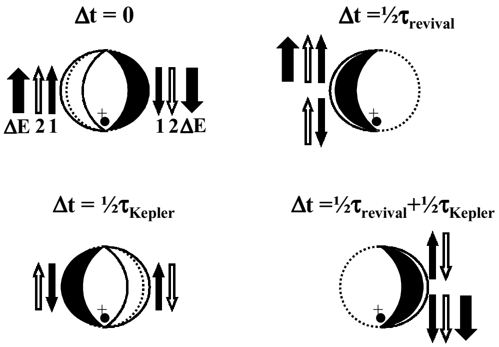

Figure 3.9: *Semi-classical picture describing the experiment. The initial state, a standing wave, is described by two counter propagating waves, illustrated by the white and black part. The situation is shown at four different delay times, respectively at delay* $= 0$ *s, delay* $= \frac{1}{2}\tau_{Kepler}$*, delay* $= \frac{1}{2}\tau_{revival}$ *and delay* $= \frac{1}{2}\tau_{revival} + \frac{1}{2}\tau_{Kepler}$*. The influence of the first half cycle on each wave is shown by the small black arrow, the influence of the second HCP by the white arrow. The big black arrow shows the net energy change.*

state, a standing wave, as two counter propagating waves. In Fig. 3.9 these two propagating waves, moving along the orbital, are illustrated by the white and black part. The black fraction represents the wave moving towards the nucleus and the white represents the outgoing wave. Suppose the direction of the momentum kick of the first HCP increases the energy of the white wave. Then the first HCP will decrease the energy of the other, black wave, because for this wave the momentum is opposite in sign. The effect of the first HCP is shown by the small black arrows. If the second HCP interacts with the atom at the same time as the first HCP (delay = 0 s) and has the same polarity, then the second HCP will have the same effect on the electron, illustrated by the white arrows. So it will also increase the energy of the white wave and decrease the energy of the black wave. The net energy change, shown by the big black arrows will be equal in magnitude for both waves, but opposite in sign. This will result in electron transitions from the initial manifold to both higher and lower n-manifolds. Let us now consider what happens if the second HCP arrives half a Kepler roundtrip time later than the first HCP (delay $= \frac{1}{2}\tau_{Kepler}$). The initial momentum of the electron will have changed sign in the meantime and the effect of the second HCP will be opposite to the effect of the first HCP. The kick of the second HCP cancels the energy change caused by the kick of the first HCP. So the energy change of both waves will be zero: The electrons stay in their initial state. When the delay is equal to one Kepler roundtrip time the situation will be almost equal again to zero delay. The electrons will move to both higher and lower states. In summary, if the delay between the HCP is small we will notice that respectively the electrons move to both higher and lower states and half a Kepler roundtrip time later they will stay in the initial state. The oscillations of the final population of the higher and lower states. This is what we also observe in our data (Figs. 3.6a and 3.7).

If the delay between the two pulses equals half the revival time of a wavepacket, the two initially counter-propagating waves are now co-propagating, i.e. the waves are at the same side of the orbit and propagate in the same direction. So their momentum will be equal. As a result the second HCP will have the same effect on both waves. Suppose that the second HCP increases the energy of the waves, then the net energy after exposure to both HCP will be increased for the white wave and for the black wave the energy change caused by the first HCP will be cancelled by the second HCP. A fraction of the population will move to higher manifolds and the rest will stay in the initial state. If the second half-cycle pulse arrives half a revival time plus half a Kepler roundtrip time later than the first HCP (delay $= \frac{1}{2}\tau_{revival} + \frac{1}{2}\tau_{Kepler}$) the second HCP will decrease the energy of both waves, because the initial momentum of the electrons has changed sign again. The net energy gain after exposure to both HCP will be zero for the white wave while decreased for the black wave. Again a part of the population stays in the initial state and the rest will move to lower manifolds. In summary, near $\frac{1}{2}\tau_{revival}$ the population in the initial state remains constant and a part of the population will move alternating to higher and lower manifolds. The oscillations in the final population of the higher and lower n-states are out of phase. This behavior we see in our data (Fig. 3.6a and Fig. 3.7).

The same semi-classical interpretation holds for antiparallel polarity of the HCP as well. The only difference is that for the same momentum of the electron the effect of the second HCP will be opposite to the effect of the first HCP. This will lead to a phase shift of π in the fast oscillations.

3.4.2 Calculation

We determined the expectation value of the z-coordinate (direction parallel to the electric field) of the wavepacket in time to support our semi-classical interpretation. When the wavepacket parts are counter-propagating, i.e. the wavepacket is delocalized, we expect to see an averaged, constant z-coordinate. When the wavepacket parts are co-propagating, i.e. the wavepacket is localized, the z-coordinate will oscillate between its extremes. The parabolic eigenfunctions ψ are, as determined by

Bethe and Salpeter [86]

$$\psi_{n_1,n_2,m}=\frac{e^{\pm im\varphi}}{\sqrt{\pi n}}\frac{n_1!^{\frac{1}{2}}n_2!^{\frac{1}{2}}\varepsilon^{m+\frac{3}{2}}}{(n_1+m)!^{\frac{3}{2}}(n_2+m)!^{\frac{3}{2}}}e^{-\frac{1}{2}\varepsilon(\xi+\eta)}(\xi\eta)^{\frac{1}{2}m}L^m_{n_1+m}(\varepsilon\xi)L^m_{n_2+m}(\varepsilon\eta) \tag{3.10}$$

$$n_1=\frac{n+k-1-|m|}{2}, n_2=\frac{n-k-1-|m|}{2}. \tag{3.11}$$

The amplitudes of the eigenstates after the first HCP kick, the kick which generates the wavepacket, can be determined in time as mentioned in section 3.3.2 by numerical integration of the Schrödinger equation, with one difference: The pertubation $E(t)$ is given by the electric field of one HCP.

Because of computation problems at high n-manifolds, the calculation is done around $n = 25$. The electric field $E(t)$ and the pulse duration of the HCP have to be scaled. To stay in the impulsive regime the ratio of the pulse duration of the HCP to the Kepler round trip time has to be constant. The electric field of the HCP is scaled to ensure an equivalent amount of population transferred to Δn. It turns out that the electric field of the HCP has to be proportional to $\overline{n}^{-4}$.

$$\tau_{HCP} \propto \tau_{Kepler} \propto \overline{n}^3 \tag{3.12}$$

$$E_{HCP} \propto E_{ionization} \propto \overline{n}^{-4} \tag{3.13}$$

So the electric field E_{HCP} and the pulse duration used in the calculation are respectively 1311 Vcm^{-1} instead of 200 Vcm^{-1} and 0.138 ps instead of 0.57 ps. The eigenstates involved are the lowest Stark states of the manifolds $n = 23 - 28$ instead of manifolds $n = 37 - 43$.

The expectation value of the z-coordinate is plotted in Fig. 3.10 as the wavepacket evolves in time. The maximum of the HCP is at 0 ps. At negative times the expectation value of the z-coordinate of the initial, stationary state is constant in time and of the order $\frac{3}{2}n^2a_0$, which we would expect for a standing wave. After exposure to THz radiation, at positive times a wavepacket is formed. The initially standing wave can be described as two counter-propagating waves. The wavepacket will be delocalized over the orbit and therefore the expectation value of the z is still constant in time. As we approach $\frac{1}{2}\tau_{revival}$ the two initially counter-propagating wavepacket parts are now co-propagating, the wavepacket is localized on the orbit. The z-coordinate starts to oscillate, with an oscillation period equal to the Kepler orbit time $\tau_{Kepler} = 2.37$ ps for $n = 25$). The oscillation amplitude increases until it reaches its maximum at $\frac{1}{2}\tau_{revival}$, where the population is fully localized. The localized wavepacket moves in and out the core region, causing large oscillations in the z-coordinate. Hereafter the oscillations decay as the wavepacket gets slowly delocalized. The expectation value of the z-coordinate is constant again at one revival time ($\tau_{revival} = 19.5$ ps). The wavepacket is fully delocalized again. In Fig. 3.11 we plotted the wavepacket

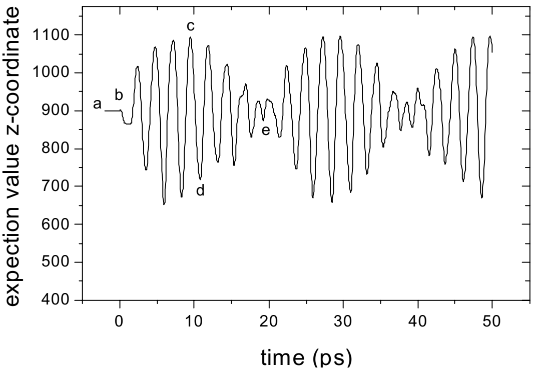

Figure 3.10: *The expectation value of the z-coordinate (direction parallel to the electric field) is plotted as a function of time. The maximum of the HCP is at zero ps. As can be seen the wavepacket is initially delocalized, no oscillations, and after $\frac{1}{2}\tau_{revival}$ localized.*

at specific times, denoted in Fig. 3.10 with the letters a-e, to make the dynamics of the wavepacket visible. The population $\left(\Psi^2\right)$ is plotted in the xz-plane (z-direction parallel to the electric field) after integration over the y-coordinate. The wavepacket is symmetric in the xy-plane ($m = 0$).

3.5 Summary

We investigated the dynamics of a THz wavepacket both experimentally and theoretically. Such a THz Rydberg wavepacket differs from conventional Rydberg wavepackets. In a THz wavepacket the initial state, out of which the coherent superposition of wavepacket states is populated, is part of the wavepacket. In the experiment a delayed, THz probe pulse, monitors the dynamics of the wavepacket. We found oscillations in the final population as a function of the delay between the two HCP. In the presence of a small static electric field these oscillations match the Kepler orbit frequency, while in absence of a static electric field the oscillation frequency is given by the dipole allowed transitions from the initial state. The calculations are performed by numerical integration on the Schrödinger equation. These calculations confirm our observations on the population redistribution, in particular when the population oscillations of the different Rydberg states are in and out of phase. Oscillations with a frequency matching a direct $\Delta n = \pm 2$ transition are predicted by theory but not found in the experiment. We have no explanation for this discrepancy.

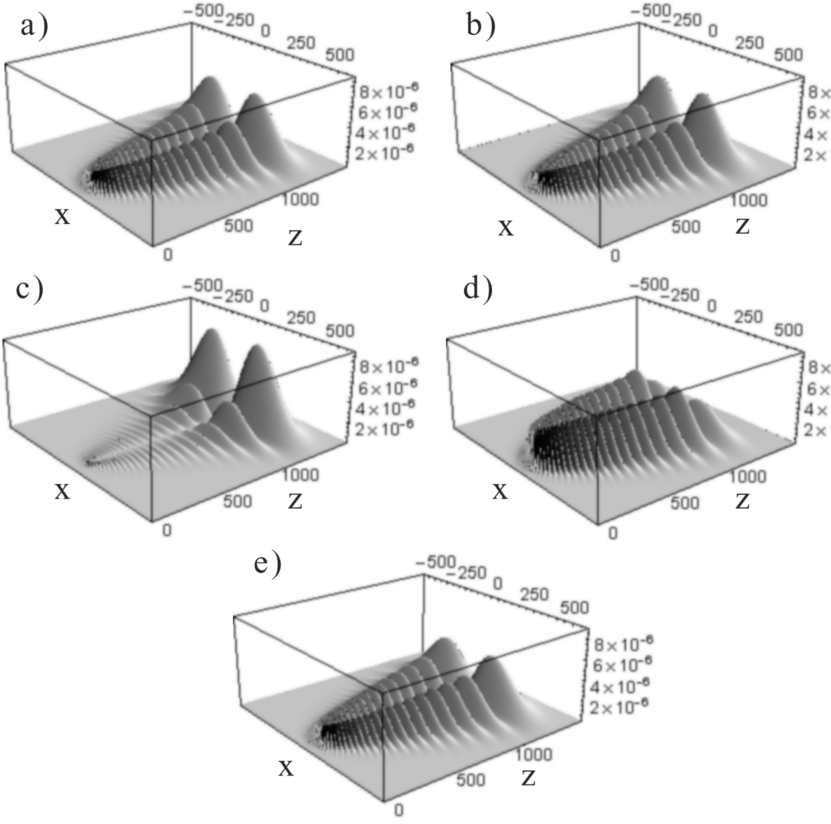

Figure 3.11: *The wavepacket is plotted at specific timepoints, denoted in figure 9 with the letters a-e, to illustrate the dynamics of the wavepacket. In figure a the standing wave is plotted. The population is distributed over the whole orbital. In figure b, during the interaction of the HCP with the Rydberg atom, the population is still distributed over the whole orbit (delocalized), which one can describe as two counter-propagating waves. In figure c+d the two initially counter-propagating waves are co-propagating. The population is localized on the orbit. In figure c the two co-propagating waves are at the outer turning point. In figure d the two co-propagating waves are at the inner turning point. In figure e the two former co-propagating waves are counter-propagating again and the population is distributed over the whole orbit.*

Further insight in the dynamics is obtained by a semi-classical picture, using that a standing wave can be described by two counter-propagating waves. We supported our semi-classical picture by calculating the expectation value of the z coordinate as the wavepacket evolves in time and by plotting the wavepacket at specific time points. The short-term evolution, the Kepler orbit motion, and the long-term evolution, the decay and revival of the wavepacket, of a THz wavepacket are comparable with the short-term and long-term evolution with a optical wavepacket. The large difference is that an optically excited wavepacket is initially localized, whereas a THz wavepacket is initially delocalized and becomes localized after $\frac{1}{2}\tau_{revival}$.

Chapter 4

Rydberg State Ionization by Half-Cycle Pulse Excitation: Strong Kicks Create Slow Electrons

The asymptotic velocity distribution of electrons ionized in half-cycle-pulse excitation of high Rydberg states ($n = 34$), placed in a static electric field, is studied using electron-velocity-map imaging. At weak half-cycle-pulse strengths, the electrons escape over the saddle point in the potential. For strong half-cycle pulses, the electrons are emitted in the direction of the field kick. The much slower and less intense half cycle of opposite polarity, which necessarily follows the main half-cycle pulse, strongly affects the momentum distribution and reduces the excess energy of the electrons significantly.

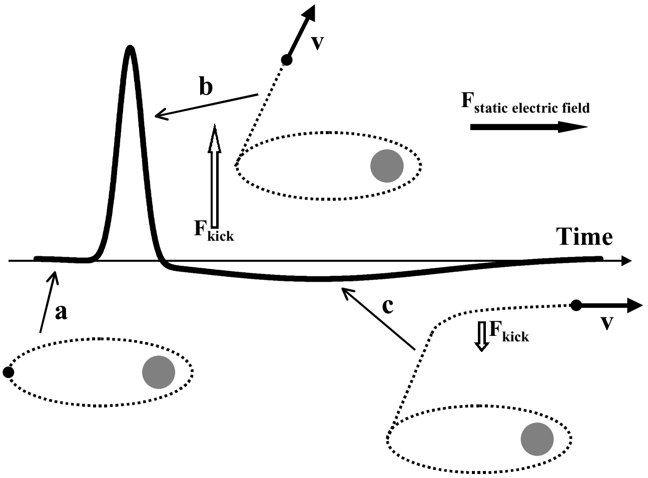

Figure 4.1: *Illustration of the influence of the weak tail of the HCP on the momentum distribution of the ionized electron. The kick of the HCP is shown by the white arrows. a) Initially the electron is in a high Rydberg state. b) The main HCP generates electrons with a high velocity in the direction of the kick (the velocity of the electron is shown by the black arrow). c) The tail of the HCP, which induces a weaker force on the electron but over a longer time range, reduces the velocity in the direction (anti)parallel to the kick to almost zero. The static electric field accelerates the electron towards the detector.*

4.1 Introduction

New developments in the generation of ultrashort pulses have enabled researchers to study a wide variety of new phenomena in Rydberg atoms. It has become possible to generate ultra-short so-called half-cycle pulses (HCP) with a frequency spectrum in the THz regime [41–43]. If the pulse duration of the HCP is much shorter than the classical round-trip time of the Rydberg electron the interaction of the HCP with the Rydberg electron can be described as a momentum kick [15, 25–28, 87]

$$\Delta \mathbf{p} = - \int \mathbf{E}_{HCP}(t) dt, \tag{4.1}$$

where $\mathbf{E}_{HCP}(t)$ is the electric field of the HCP. In this limit the resulting energy transfer is given by

$$\Delta E = \mathbf{p}_0 \cdot \Delta \mathbf{p} + \frac{1}{2} \Delta p^2, \tag{4.2}$$

where p_0 is the initial momentum of the electron. An HCP does not propagate freely in space, as the time integral of the electric field is zero in the far field. In fact, an HCP consists of a very short main half cycle, followed by a long half-cycle pulse of opposite polarity of much smaller amplitude such that the integral of both half-cycle parts is equal. The latter half-cycle pulse is called ‘the tail’ in the remainder. Tielking *et al.* [13] showed that this long negative tail can reduce the ionization efficiency. Wesdorp *et al.* [14] found suppression of ionization for very high Rydberg states ($n > 70$), if the electron orbit time is much longer than the duration of the full cycle pulse, further called FCP. In this regime the change in momentum equals $\Delta p \approx 0$. Otherwise, effects of the FCP have not been described. In this chapter we focus on the ionization of Rydberg states of xenon with energies very close to that of the saddle point in the potential created by the Coulomb field and an external static electric field. Excitation of the Rydberg states takes place in the n-mixing regime, where we excite an incoherent superposition of several k states. Classically, the external homogeneous electric field will make the Rydberg states undergo oscillations in the orbital angular momentum, l. Hence the HCP that follows the formation of the Rydberg state interacts with a mixture of electronic angular momentum states. Velocity-map imaging [33] is used to determine the asymptotic momentum distributions in the two directions perpendicular to the static electric field. The polarization of the half-cycle pulse is perpendicular to the static electric field. The experiments are complemented by classical calculations. The measurements and calculations show that the slow and weak tail following the HCP does not affect the ionization probabilities but influences the momentum and energy distribution of the free electrons, nullifying the energy gain from the main HCP. Our finding is illustrated in Fig. 4.1. The initial HCP, because of its short duration, creates electrons with significant momentum/velocity in the direction of the kick. The tail transfers the same amount of momentum but in the opposite direction and reduces the momentum of the free electrons.

4.2 Experimental Method and Theoretical Description

4.2.1 Experimental Setup

Figure 4.2 shows the experimental setup. In our experiment, metastable xenon atoms in the $^3\mathrm{P}_{J=2}$-state are produced in an electron-impact source [88]. The outer electron, an s-electron, is excited further using pulsed nanosecond UV radiation to Rydberg levels about 3 cm^{-1} below the saddle point in a static (220 Vcm^{-1}) electric field. The UV polarization is in the x-direction. The electric field is in the z-direction. After 500 ns, an HCP is generated by illuminating a GaAs wafer with intense light of 100 fs duration from a regeneratively amplified Ti-Sapphire laser. The strength of the HCP is changed using the bias-voltage over the GaAs wafer. The HCP is polarized along

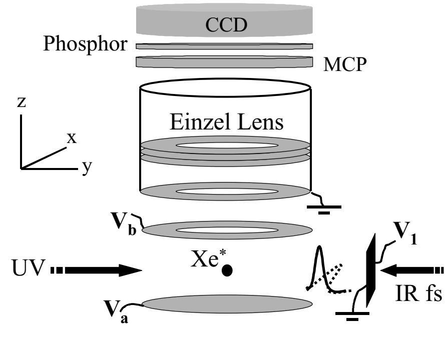

Figure 4.2: *Illustration of the experimental setup. See text for details.*

the x-axis, while its direction is changed by inverting the polarity over the wafer. The kick direction refers to the direction of the force as felt by the electron, which is opposite to the electric field vector of the HCP. The HCP measures about 1 ps, the tail has an estimated duration of 10 to 20 ps. The HCP excitation takes place in the source region of a velocity-map-imaging setup [33]. The imaging apparatus consists of an extraction region containing two electrodes, which create a static electric field to accelerate the electrons into a 50 cm long field free time of flight tube towards a microchannel-plate detector followed by a phosphor screen. The very-low-energy electrons are affected by the combined Coulomb and electric field. [37–39] The final perpendicular momentum may only be established as far as 10 μm away from the ionic core. Since the static electric field in this experiment has a significant effect on the xenon atoms as evidenced by the Stark structure, a symmetry axis parallel to the detector does not exist. As a consequence the velocity distribution of the z-component can not be reconstructed by, for example, a so-called Abel inversion procedure. A second electrostatic lens was installed to magnify the image of the very-low-energy electrons on the detector [34]. Individual electrons were detected using a point finding routine. Each image is the sum of 4000 shots. The strength of the HCP excitation and the momentum or velocity scale in the x- and y-direction of the images were calibrated in independent experiments. The strength of the HCP pulses was determined using field-free ionization of $n = 35$ Rydberg states. In the impulsive kick limit, at 50% ionization by the HCP the energy transferred, $\frac{1}{2}\Delta p^2$, equals the binding energy [26]. The observed displacements, Δx and Δy, of the electrons on the detector are expressed in the asymptotic (perpendicular) momentum, p_x and p_y, by performing near-threshold photo-ionization based on experiments by Nicole *et al.* [38, 39]. Analytical calculations provide the relation between the displacement of the photo-ionized electrons on the detector and their asymptotic perpendicular momentum [37]. In this chapter we present data at various strengths of the half-cycle pulse monitoring both the total ionization yields and the momentum distributions, as a function of the transferred momentum Δp.

4.2.2 Classical Calculations

In Rydberg state HCP ionization classical calculations agree well with quantum calculations, see Chapter 5 [15]. The quantum nature of the Rydberg system is taken into account in the choice of the initial conditions. The dye laser excites p-type states with $m_l = \pm 1$. We selected the initial angular momentum in the Rydberg state to be $l = 1$ with projections $-1 < l_z (= m_l) < 1$. The orientation of the major axis of the elliptic orbit is chosen randomly and the electron is launched at the inner turning point. The angular momentum l is not a conserved quantity in a static electric field and its value oscillates between $l = 1$ and $l = n - 1$. The HCP is chosen to interact with the Rydberg electron randomly in time covering a full oscillation of the orbital angular momentum. The calculations provide ionization efficiencies and velocity-map images.

4.3 Results

We will first discuss the dependence of the ionization yield on the HCP strength. Figure 4.3 shows the experimentally observed ionization yield along with the result of the classical calculations. The ionization yield, as determined by integration of each image, is plotted against the momentum transfer. Saturation of the ionization signal for values of Δp above 0.06 a.u., was used as evidence for 100% ionization. The experimental points are the average of kicks in the positive and negative x-direction, which gave the same result as expected from symmetry considerations. The measured curve does not show the S-curve dependence that is often seen [15,25]. Because of the very small binding energy of the Rydberg state in the present experiment ionization already starts at very small HCP strengths obscuring the S-curve behavior. The experimental data are compared with classical calculations. Electrons only ionize if their energy is above the saddle point energy ($E_{el} > E_{sp}$). These electrons can be subdivided into three categories: I) electrons found downstream from the saddle point ($z_{el} > 4z_{sp}$ with the origin at the nucleus) in the classical trajectory calculations; these so called direct electrons escape immediately: II) electrons which did not escape independent of the calculation time but had a magnetic quantum number $|l_z|$ with $|l_z| < 1$. We assume that these electrons, called delayed electrons, will still ionize after core scattering [79]: III) all other electrons, which did not escape over the saddle point and had $|l_z| > 1$. Figure 4.3 shows that the experimental curve is accurately described by the sum of direct electrons (I) and the delayed electrons (II). In a multi-electron system such as xenon, electrons with a small value of $|l_z|$ undergo core scattering,

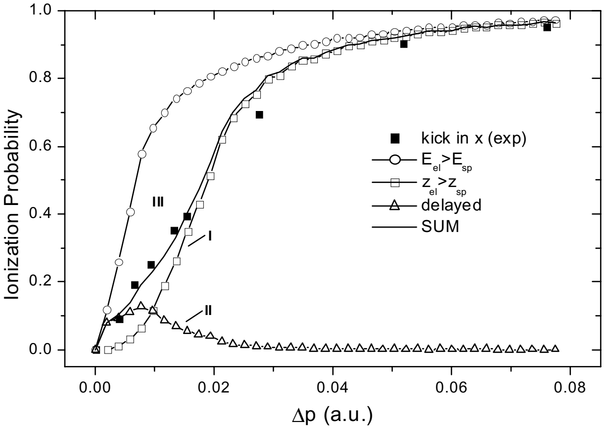

Figure 4.3: *Measured and calculated ionization curves versus momentum kick for polarization of the HCP perpendicular to the electric field. Three different contributions are shown in the calculation: I) electrons which ionize directly after the HCP kick, II) delayed ionized electrons, which ionize after scattering from the core in the direction of the saddle point and III) metastable electrons.*

conserving the value of $|l_z|$. This process may redirect the electrons towards the saddle point. The discrepancy between the observed ionization yield and the calculated yield based on the total energy of the excited atoms (open circles) leads us to conclude that some xenon atoms are formed in quasi-bound levels with lifetimes of several μs (III). The metastability is partially due to the excitation of large $|l_z|$ values, which enhances the centrifugal potential, keeping the electron away from the electric field axis and which raises the threshold field. Small variations in the assumed HCP width (1 ps full width at half maximum) have no effect on the calculated results. The relevant parameter is the integral over the electric field. Importantly, we find the calculated ionization curves to be identical using a HCP and a FCP.

The measured velocity-map images are symmetric at low kick strengths. The asymptotic electron momentum distributions are equal in the directions parallel and perpendicular to the kick. At high kick strength the images are elongated in the x-direction, showing that the electrons are ejected with a larger momentum parallel to the HCP polarization than perpendicular to it (see Fig. 4.4b). In the y-direction the images are symmetric. When the HCP is polarized in the z-direction, the p_x and p_y momentum distributions are symmetric and similar to the p_y-distribution in the case of perpendicular kick (Chapter 5). Figures 4.4a, b show experimental and calculated momentum distributions. In the inset the original images are shown. Mo-

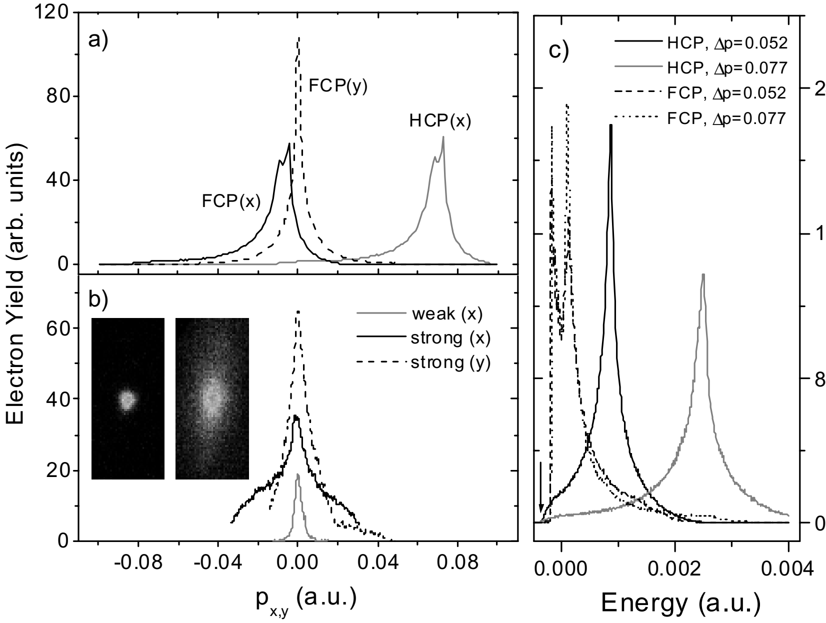

Figure 4.4: *a) Calculated momentum p_x-distributions for strong ($\Delta p = 0.077$ a.u.) kick of both a HCP and FCP and p_y-distribution for strong FCP. b) Measured momentum distributions in the x-direction for both a weak ($\Delta p = 0.004$ a.u.) and strong ($\Delta p = 0.076$ a.u.) kick and in the y-direction only for a strong kick. The images at low (left) and high (right) kick strengths are shown in the inset. c) Calculated energy distributions, for $\Delta p = 0.077$ a.u., and, additionally $\Delta p = 0.052$ a.u. The energy is related to the field-free ionization threshold. The saddle point energy is indicated by an arrow.*

mentum differences as small as $\Delta p = 0.005$ a.u. ($v = 1.1 \cdot 10^4$ m/s for an electron) can be resolved at these settings. At a small kick strength the asymptotic velocities in the x (and y) direction are small (Fig. 4.4b, gray solid line): $p_x < 0.007$ a.u. Figure 4.3 reveals that at this low kick strength, the ionization yield can only be explained invoking a delayed ionization involving core scattering (II). This process may well take at least an oscillation period of the angular momentum, about 35 ps under our circumstances. The resulting asymptotic momentum distribution does not reveal the direction of the momentum kick of the HCP. Electrons excited just above the saddle point escape through the small opening angle in the Coulomb potential if their momentum in the direction perpendicular to the electric field is small. The Coulomb potential still reduces some momentum from the x (and y) directions narrowing the distribution on the detector [38,39]. At higher kick strengths, to our initial surprise, the p_x-distribution is still centered close to zero perpendicular momentum. The maximum in the distribution seems to shift slightly to the direction opposite to the kick. The classical calculations reveal the origin of the small momentum change. A true HCP gives a significantly displaced momentum distribution (grey solid line in Fig. 4.4a). However, the tail shifts the distribution back without changing its shape. Hence, while the HCP gives the electron a substantial amount of kinetic energy, the tail of the FCP takes away the kinetic energy. Intense HCP ionization is a source of very low-kinetic-energy electrons. The momentum reduction by the tail is slightly larger than the momentum gain by the HCP, because during the second part of the pulse no kinetic energy has to be transformed into potential energy to ionize. This explains a shift opposite to the kick direction. Although we find that the observed shape is wider and less pronounced than the calculated shape, both the position and asymmetry are reproduced. The y-distribution is still symmetric. We noticed that at high kick strengths the images suffer some loss of resolution due to electronic noise from the HCP generation on the ion optics. Even in the absence of this noise the finite resolution of our detection system would hamper the observation of the splitting in the p_x-distribution. The effect of the FCP character is clearly revealed from the final total energy distributions for two high kick strengths, $\Delta p = 0.052$ a.u. and $\Delta p = 0.077$ a.u. (see Fig. 4.4c). The main HCP generates free electrons with a high kinetic energy depending on the kick strength, whereas subsequently the weak tail cancels this energy gain quantitatively and independently of the kick strength. The energy distribution after the FCP reflects the localization of the electrons in blue Stark states, located on the 'uphill' side of the potential, and electrons located on the 'downhill' side near the saddle point, near their turning points. The combination of high angular momentum, l, with small projection along the electric field, l_z results in this localization. After the kick electrons escape in the direction of the kick perpendicular to the electric field, not over the saddle point. During the ionization process electrons in the blue Stark states transform more of the gained kinetic energy into potential energy than the red Stark states. The combination of the Coulomb field and the static field results in a deeper potential well for 'blue' electrons. The tail effectively removes the kinetic energy, the difference in total energy equals the potential energy in to the static field. The distance between the turning points is about 5.10^3 a.u., which rationalizes the splitting of 5.8 meV in our field of 220 Vcm^{-1}.

4.4 Summary

In conclusion, we report on momentum distributions of electrons in HCP ionization studies starting from high-lying Rydberg states with an energy just below the saddle-point energy. At low kick strength, ionization involves a core-scattering process. At high kick strengths, the experiment and classical calculations reveal that ionization is determined by the first intense HCP excitation. The asymptotic properties of the electron are affected in a post-ionization process by the negative tail that follows the positive HCP. For most experiments the influence of the tail can be neglected. HCP excitation is still well suited for manipulating and controlling bound Rydberg electrons, with classical roundtrip times that are shorter then the duration of the tail. We show that the tail is dominating when it can interact with ionized, escaped electrons.

Chapter 5

Two-Dimensional Momentum Imaging of Rydberg States Using Half-Cycle Pulse Ionization and Velocity-Map Imaging

We describe the use of low energy electron velocity-map imaging in combination with half-cycle pulse ionization as a probe of two-dimensional momentum distributions in initial Rydberg States. The influence of the strength of the kick on the asymptotic velocity of the ionized electron has been studied for excited xenon atoms ($n^* = 34$) in the presence of a static electric field (220 Vcm^{-1}). The experiments have been complemented by classical and quantum mechanical calculations. HCP ionization combines near 100% ionization efficiency with an interaction time that is short with respect to the radial orbiting time. We find that the HCP does not change the momentum distribution in the directions perpendicular to the kick. The measured two-dimensional momentum distribution reflects the momentum distribution of the initial Rydberg state perpendicular to the electric field. This experiment constitutes a direct method to measure the momentum distribution of a Rydberg state. The properties of HCP ionization at small kick strengths are discussed.

5.1 Introduction

Since the beginning of quantum mechanics, matter is being described in terms of its wave function. Observable quantities are evaluated as expectation values of associated Hermitian operators. Details of the wave function itself mostly remain hidden. In electron-momentum spectroscopy (EMS) [89, 90] the wavefunction of an atom or molecule in their ground state is retrieved in momentum space. This technique is based on so-called $e, 2e$ experiments; An atom in the groundstate is ionized by collision with a high-kinetic-energy electron. At sufficiently high energy ($\sim$ 1 keV) the electron-electron collision is impulsive. From the final momentum and energy of both electrons (measured in coincidence) the binding energy of the ejected electron as well as its momentum at the instant of the collision can be retrieved. Two conditions determine the success of the $e, 2e$ method. The ionization cross section does not depend on the actual momentum of the electron. Secondly, the collision is sudden with respect to the classical motion of the electrons in the atom. These two conditions can be considered as general prerequisites for direct methods that measure details of the momentum distribution.

Here, we use of ultrafast, sub-picosecond half-cycle pulses (HCP) kicking electrons suddenly out of Rydberg atoms. The duration of the fast pulse is short with respect to the classical roundtrip time of the Rydberg atoms. In these circumstances, classically, the interaction of the HCP with the Rydberg electron can be described as a momentum kick

$$\Delta\mathbf{p} = -\int \mathbf{E}_{HCP}(t)dt, \tag{5.1}$$

where $\mathbf{E}_{HCP}(t)$ is the electric field of the HCP [24–26, 94]. In the short-pulse limit the resulting energy transfer is given by

$$\Delta E = \mathbf{p}_0 \cdot \Delta\mathbf{p} + \frac{1}{2}\Delta p^2, \tag{5.2}$$

where $\mathbf{p}_0$ is the momentum of the electron at the instant of the HCP interaction. Ionization can take places if the energy change exceeds the binding energy of the electron

$$E = -\frac{1}{2n^2} + 2\sqrt{F},$$

where n is the principal quantum number and F a possible applied static electric field. In practice, we can achieve 100% ionization of a sample of Rydberg atoms with one single HCP. Hence, the ionization probability does not depend on the actual momentum of the ionized electron in its orbit. The method proposed in this chapter builds on the aspect that a kick does not change the momentum in the directions perpendicular to the kick. The final electron momentum distribution may reflect the momentum distribution in the initial state perpendicular to the kick. Zobay and Alber [32] calculated angle- and energy resolved spectra resulting from the ionization of Rydberg atoms by HCP in a field-free condition. Their spectra showed that the final direction into which the electron is emitted is strongly correlated with the momentum in the orbit before application of the pulse. Jones [9, 31] used HCP ionization as a method to determine one-dimensional momentum distributions along the polarization direction of the HCP. Robicheaux [15] treated this process theoretically. Their technique measures the ionization probability as a function of the kick strength. The energy gain or loss by the electron depends on its initial momentum and on the strength of the HCP kick. For each kick strength, Δp, there exists a minimum value $\mathbf{p}_0$ of the Rydberg electron for which it will just ionize. Hence the probability of finding an electron with a momentum component $\mathbf{p}_0$ in the direction of the kick is equal to the increase in the ionization yield when increasing the HCP strength to Δp. Thus, the derivative of the ionization yield as function of HCP strength equals the fraction of the Rydberg electron as function of the initial momentum. The method requires a scan over different HCP strengths. In contrast, the present method uses only one strong HCP kick strength. Moreover, the 2D momentum maps are obtained directly without taking the derivative of experimental data.

In our experiment we create Rydberg states (with principal effective quantum number $n^* = 34$ and magnetic quantum number $m = 0$ or ± 1) in xenon in a static electric field (220 Vcm^{-1}) just below the saddle point created by the Coulomb field and external static electric field. Subsequently these Rydberg atoms are ionized with a HCP. The final momentum distribution of ejected electrons can be measured with a so-called velocity imaging technique [33]. In this technique, the position of the electrons on the detector only depends on the asymptotic x- and y-component of the velocity of the electrons. We will illustrate the potential of HCP ionization as a direct method looking at wave functions by first empirically comparing momentum images obtained with different HCP polarizations. Theoretical support is obtained by the use of classical trajectory simulations of our Rydberg states and of the HCP ionization process.

The experimental setup is described in section 5.2. The experimental results are simulated with classical and quantum mechanical calculations. The classical and quantum mechanical calculation methods are explained in section 5.3. In section 5.4 the experimental and theoretical data are compared. We note that in the far field a pulse is not a true HCP, instead it is followed by a much longer and weaker half cycle of opposite polarity. In Chapter 5 we have argued that this tail does not influence the ionization dynamics but only influences the asymptotically measured momentum in the direction of the kick.

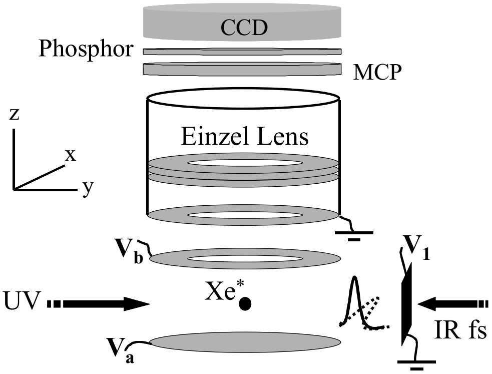

Figure 5.1: *Schematic representation of the experimental setup (for details see text).*

5.2 Experimental Setup and Rydberg state properties

In Fig. 5.1 a schematic drawing is shown of the experimental setup. In the experiment xenon atoms were prepared in the $^3P_2$, $J = 2$ metastable state in an electron impact source [88]. The metastable atoms consist of an s-electron around a $^2P_{3/2}$ core. If we ignore the spin of the Rydberg electron, the s-character of the electron results in magnetic quantum number $m = 0$. Single-photon excitation of this xenon atom results in a p-type Rydberg electron. Highly excited xenon Rydberg atoms (with principal effective quantum number $n^* = 34$ and electron roundtrip time $\tau_K = 6$ ps) were created in a static electric field of $\sim$ 220 V/cm by one photon excitation of the metastable xenon with the doubled frequency of a nanosecond dye laser. The UV beam was loosely focused into the metastable xenon beam. The presence of the electric field has two consequences. Firstly, the dye laser can be polarized both parallel to the electric field as well as perpendicular to the electric field. This choice directly affects the preparation of the p-orbital. When the dye laser was polarized parallel to the static electric field (z-direction), which was chosen as the quantization axis, p-type states with magnetic quantum number $m = 0$ were excited. When the dye laser was polarized in the x-direction (perpendicular to the static electric field) p-type states with magnetic quantum number $m = \pm 1$ were excited. Secondly, the electric field causes the orbital angular momentum, l, to be non-conserved and consequently, in classical terms, oscillates between its minimum and maximum value. In our experiment the static electric field was strong enough to reach the n-mixing regime.

The highly excited Rydberg states were ionized after a delay of 500 ns by an HCP, with the polarization either perpendicular to (along the x-direction) or (anti)parallel (along the z-direction) with the static electric field. The y-axis is the dye laser and HCP propagation direction. Wherever we speak of kick direction, we imply the direction of the force as felt by the electron. Hence the kick direction is opposite to the direction of the electric field vector associated with the HCP. Symmetry ensures that a kick in the positive and negative x-direction are equivalent. In the case of a kick in the negative or positive z-direction, the electrons are either kicked in the uphill direction of the electric field or in the downhill direction towards the saddle point. In the following we concentrate mainly on the results obtained with the HCP polarization parallel to the electric field. Some results with the HCP polarization perpendicular to the electric field have been described in Chapter 4.

The HCP was created by illuminating a biased GaAs wafer with pulses of ~ 100 fs duration and at 800 nm from a regeneratively amplified Ti:sapphire laser system. Illumination of the GaAs-wafer with photons of an energy above the band gap lifts electrons from the valence band to the conduction band, generating free charge carriers. These free charge carriers are accelerated by the bias field and radiate a short electromagnetic half-cycle pulse containing frequencies of up to some THz [41–43]. To increase the breakdown voltage of the GaAs wafer, we applied a pulsed high voltage up to 7 kV. We mounted an RC circuit directly on the semiconductor wafer to reduce the electronic noise involved with the HCP generation, see section 2.2.

The final velocity and angular distributions of the electrons were measured by velocity-map imaging [33]. The imaging setup consists of an extraction region containing two electrodes, which create the aforementioned static electric field and accelerate the electrons into a 50 cm long field free time-of-flight tube towards a microchannel plate assembly (MCP) backed by a phosphor screen. A μ-metal shield surrounds the extraction region and time-of-flight tube. The electron optics design includes an optical lens focusing the electrons with the same velocity on a single spot on the detector. Inside the time-of-flight tube an Einzel lens is present. The first lens system creates a velocity map at the entrance of the Einzel lens, which magnifies this map onto the imaging detector [34]. The electrons are registered by the microchannel plate (MCP). A computer controlled CCD camera is used to record the image from the phosphor screen behind the MCP. The images described in this chapter were collected averaging 4000 shots for each set of experimental conditions. Often, in velocity-map imaging, the two-dimensional images contain all information to retrieve the full three dimensional kinematics. The presence of a symmetry axis in the experiment parallel to the detector surface suffices for the applicability of a so-called Abel inversion procedure and the static electric field simply carries the ions/electrons to the detector [36]. In the present experiment such a symmetry axis does not exist since the static electric field in this experiment has a significant effect on the xenon atoms as evidenced by the Stark structure. As a consequence the velocity distribution of the z-component can not be reconstructed. Only the velocity components in the x- and y-direction, i.e.

perpendicular to the static electric field, reveal the effects of the HCP excitation in a displacement on the detector. Furthermore, in the case of very-low-energy electrons (<10 meV), the combined Coulomb and electric field exhibits a focusing effect depending on the ejection angle of the low energy electrons [37]. In fact the asymptotic perpendicular components of the momentum of the electron may only be established as far as 10 μm away from the ionic core.

The strength of HCP kick and the momentum or velocity scale in the x- and y-direction of the images were calibrated in independent experiments. The strength of the HCP was determined using field-free ionization of $n = 35$ Rydberg states. In the impulsive kick limit, at 50% ionization by the HCP the energy transferred, $\frac{1}{2}\Delta p^2$, equals the binding energy [26]. We note that the momentum kick is linear with the bias over the GaAs wafer. The displacement of the electrons on the detector is expressed in transferred (perpendicular) momentum, p_x and p_y, by performing near threshold photo-ionization [38, 39]. Analytical calculations provide the relation between the displacement Δx of the photo-electrons on the detector and their asymptotic perpendicular momentum [37]. In this chapter we present data at various strengths of the half-cycle pulse monitoring both the total ionization yields and the momentum distributions.

5.3 Classical and Quantum Mechanical Calculations

The classical calculations were performed by solving the three-dimensional classical equations of motion for an electron in a hydrogenic atom in an electric field using a 4th-order Runge-Kutta algorithm. The trajectories start at the inner turning point, with initial conditions derived from quantum mechanics. The initial state is a stationary Rydberg state given by the quantum numbers $n = 34$. The dye laser excites the Stark state through its p-character. Because of the presence of an electric field, the orbital angular momentum l is no longer a conserved quantity, but in classical terms l oscillates. The dye laser was either polarized parallel (along the z-axis) or perpendicular (along the x-axis) to the electric field, exciting Rydberg states with respectively magnetic quantum number $m = 0$ and $m = \pm 1$ Rydberg states. Xenon is a multi-electron system with a complex ion core with $J = 3/2$. The interaction with the multi-electron core results in a change in the direction of the long axis of the elliptic orbit each time when the electron penetrates the core, keeping both the angular momentum vector constant. In the case of excitation with the dye laser polarized along the x-axis (perpendicular to the static electric field) the directionality along the x-axis is assumed to disappear due to the interaction with the complex ion core and the 500 ns delay between the excitation dye laser and the HCP. Interaction with the core takes place at small angular momentum, and occurs every l-oscillation time (35 ps). At these small values of the angular momentum, the orientation of the orbit can rotate in the xy-plane and regains cylindrical symmetry again around the

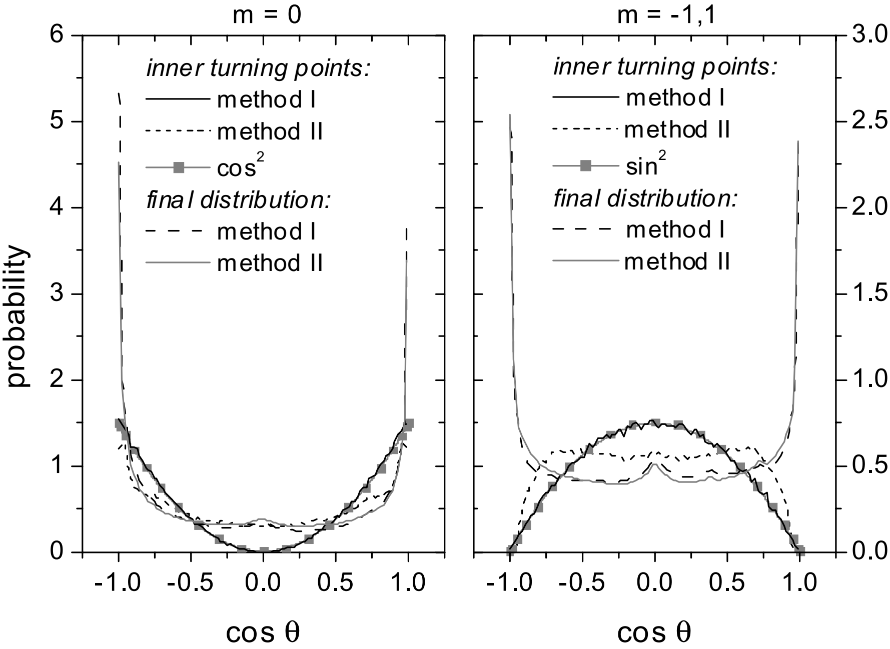

Figure 5.2: *Distributions of the inner turning points and the distribution averaged over the full l-oscillation are plotted as a function of cos θ for two different methods. Method I weigh the possible orientation of the orbits with the quantum mechanical angular probability distribution. Method II takes l_z randomly in a small interval instead of weighing with the square of the spherical harmonic.*

z-axis. Therefore the initial conditions in the classical trajectory calculations involve the principal quantum number, the angular momentum and the magnetic quantum number.

A realization of quantum states using classical trajectories is not unambiguous. The dye laser excites the p-character in the Stark state. However, due to the occurrence of l-oscillations most of the time the angular momentum is much larger. In the following we will argue how the initial conditions have been chosen for the classical trajectory simulations of the HCP ionization process. We show that different methods of selecting the starting conditions for the classical trajectories, that is the orientations of the elliptic Rydberg orbits results in nearly identical momentum distributions of the dye laser prepared states. One method is to represent the magnetic quantum numbers $m = 0$ or ± 1 by choosing respectively $l_z = 0$ or $l_z = \pm 1$, and with the magnitude of $|l| = 1.5$. The quantum angular distribution given by the square of the spherical harmonic Y_{lm} is imposed by weighing all orientations possible fixing l and l_z. The square of the spherical harmonic for a p-state with $m = 0$ and $m = \pm 1$ are given by

$$|Y_{10}(\theta,\varphi)|^2 = \frac{3}{4\pi}\cos^2\theta, \tag{5.3}$$

$$|Y_{11}(\theta,\varphi)|^2 = \frac{3}{8\pi}\sin^2\theta, \tag{5.4}$$

where θ is the angle with the quantization z-axis, and φ the rotation around the z-axis. An alternative method is to allow l_z to take random values in certain intervals, respectively $l_z \in [-0.5, 0.5]$ for $m = 0$ and $l_z \in [-1.5, -0.5], [0.5, 1.5]$ for $m = \pm 1$. Figure 5.2 shows probability distributions as function of the cosine of the polar angle with respect to the z-axis, $cos\theta$, both plotting the distribution of the starting points of the trajectories as well as the distribution averaged over the full trajectory including one full l-oscillation. Figure 5.2a shows the situation in the case of simulation $m = 0$ while Fig. 5.2b shows the results for $m = \pm 1$. As a reference the quantum distributions from Eqs. 5.3 and 5.4 are plotted in this Fig. 5.2. Although the angular distribution of the inner turning points is slightly different in both methods, the final distribution over θ averaged over a complete trajectory including a full l oscillation are nearly indistinguishable. Fig. 5.2 shows that the angular distribution peaks strongly at $cos\theta = \pm 1$. Since l_z is conserved during the increase in l, the angular momentum vector grows perpendicular to the z-axis. As a consequence, all orbits always come close to or cross the z-axis.

We calculate the trajectories for random HCP time points over one complete angular momentum oscillation period to take into account all possible l values starting at $l = 1$. (Classical) ionization is allowed if the final energy of the electron exceeds the saddle point energy ($E_{el} > E_{sp}$). However close to the saddle point quasi-bound levels exist, that are not directed towards the saddle point and that therefore do not escape over the saddle point [19, 20]. In the classical trajectory calculations atoms in a static electric field F are ionized if they are found downstream from the saddlepoint ($z_{el} > 4z_{sp} = 4/\sqrt{F}$ with the origin at the nucleus). To simulate the observed images, the trajectories of the directly ejected electrons were calculated further by solving the classical equations of motion numerically. The velocity distribution of the electron in the x, y-directions far away from the core, where the coulomb field is negligible, represents the velocity map. The work on threshold photoionization has made clear that electrons which have very low kinetic energies (<10 meV) maybe subject to focusing effects by the combination of the Coulomb field and the static electric field. This aspect has been checked by comparing the value of the x-,y-component at the saddle point with the value of the x-,y-component at large value of z. Indeed we see at a small kick strength of $\Delta p = 0.005$ a.u. (energy transfer $\frac{1}{2}\Delta p^2 = 0.34$ meV) a focusing effect of $\sim 35\%$ reduction of the velocity. At high kick strength, for example $\Delta p = 0.07$, the kinetic energy transfer $\frac{1}{2}\Delta p^2$ is equal to 67 meV, which is far away from the slow electron regime (<10 meV). Indeed classical calculations show that at high kick strength ($\Delta p = 0.07$) focusing effects do not play a role.

Quantum mechanical calculations were performed to prove the reliability of the classical calculations. We have used quantum-mechanical calculations to reproduce the classical calculated ionization curve and the momentum distribution of the initial, excited Rydberg state. To reproduce the ionization curve we used a special designed program by Muller [91]. The energy distribution after HCP ionization is calculated for each angular momentum state in $n = 34$. The static electric field determines the saddle point. An electron is ionized if its final energy is above the saddle point energy. In the course of this research we have also simulated momentum distributions using a quantum description of hydrogenic Stark states [92]. Being in the n-mixing regime and in accord with our classical calculation which simulates all k-states, we have determined the momentum distribution of the excited Rydberg state by adding the momentum distributions of all 34 k-states for $n = 34$.

5.4 Results

In the following we will first describe ionization curves measured with HCP polarization in the z-direction in order to increase our general understanding of this phenomenon. Thereafter, we will describe our images providing empirical evidence for velocity-map imaging and HCP ionization as a direct probe of momentum distributions in wave functions. We will compare our experimental data with classical and quantum mechanical calculations.

In Fig. 5.3 the experimentally observed ionization curve versus momentum kick of the HCP is shown for (anti)parallel polarization (z-direction) of the HCP. The dye laser was polarized parallel to the electric field, so an initial Rydberg state with magnetic quantum number $m = 0$ is excited. The ionization yield is plotted against the absolute momentum transfer provided by the HCP, which is calibrated as described

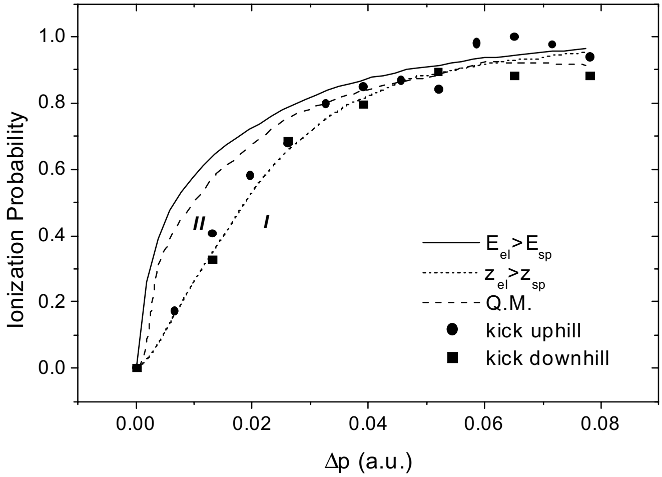

Figure 5.3: *Measured and Calculated ionization probability as function of the momentum transfer (*Δp*) for a HCP parallel/antiparallel to the external static electric field (z-direction). The symbols represent the measurement, The solid line represents classically calculated ionization yield using* $E_{el} > E_{sp}$*, the dotted line represents classical calculated ionization yield using* $z_{el} > 4z_{sp}$ *and the dashed line represents a fully quantum calculation as field free excitation.*

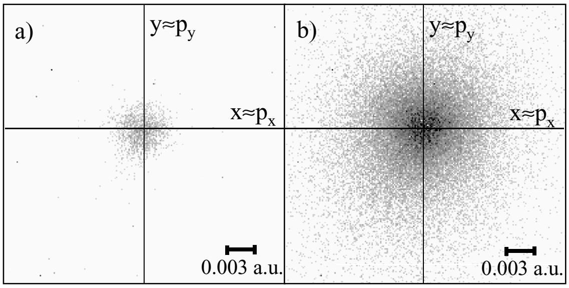

Figure 5.4: *Raw images taken at two different HCP kick strength, a) 10% ionization, b) 100% ionization using parallel kick. The momentum scale is indicated in the figure.*

before. Saturation of the ionization signal for values of Δp above 0.06 a.u. was used to fit the experimental curve with the calculated ionization curve. The electrons were kicked either uphill or downhill in the direction of the saddle point. To our surprise, in spite of this physical difference in kick direction the ionization curves are still the same within the experimental error. The measured data does not display the S-curve dependence that is often seen [15,25]. Because of the very small binding energy of the Rydberg state in the present experiment ionization already starts at very small HCP strengths obscuring the S-curve behavior. In Fig. 5.3 also the classical and quantum mechanical calculated ionization curves for polarization in the z-direction are shown. Small errors in the assumed HCP width (taken to be Gaussian with 1 ps FWHM in the calculations) cancel since the important parameter of the HCP pulse is the integral over the electric field. In the classical calculations opposite kick directions gave similar ionization curves, which are not included in Fig. 5.3. As mentioned before two ionization criteria are used in the classical calculations, $E_{el} > E_{sp}$ and $z_{el} > 4z_{sp}$. These criteria will divide the electrons which have enough energy to escape into two categories: *I*) Electrons, which escape actually over the saddle point in a hydrogenic model and *II*) metastable states. The quantum mechanical resulting ionization curve is very close to the classical ionization yield based on the final energy of the excited electrons. Fig. 5.3 provides support for the validity of trajectory calculations for the HCP ionization process. It is interesting to note that the agreement between the quantum and classical calculations suggests that at low kick strengths a significant amount of metastable atoms are formed, which have sufficient energy to go over the saddle point but never reach this point. We conclude that just above the saddle point quasi-bound levels exist which are not directed towards the saddle point and therefore the electrons can not escape over the saddle point and ionize [19,20]. We note finally that these states are not protected from ionization by an angular-momentum barrier as both the dye laser as the HCP polarization was chosen parallel to the electric field axis resulting in $m = 0$ final states.

Velocity distributions were measured at different kick strengths. In Fig. 5.4 the raw images are shown for a weak (10% ionization, $\Delta p = 3 \cdot 10^{-3}$ a.u.) and a strong (100% ionization, $\Delta p = 6 \cdot 10^{-2}$ a.u.) kick in the z-direction. The dye laser was polarized perpendicular to the electric field, exciting a Rydberg state with magnetic quantum number $m = \pm 1$. The momentum distributions in the x,y-plane are cylindrical symmetric over the whole intensity range, and become wider at stronger kicks. The experiment was repeated with the dye laser parallel to the electric field. Initially Rydberg states with magnetic quantum number $m = 0$ were excited. The momentum distributions in the x,y-plane were again cylindrical symmetric over the whole intensity range, but at high kick strengths narrower than in the case of $m = \pm 1$ states. By integrating the images along the x- and y-direction, we can look at the p_x- and p_y-momentum distributions individually. In Fig. 5.5 the measured p_x-momentum distributions for a kick in the z-direction are shown at low (10% and 30% ionization, $\Delta p = 3 \cdot 10^{-3}$ a.u. and $\Delta p = 1 \cdot 10^{-3}$) and high kick strength ($\sim$ 100% ioniza-

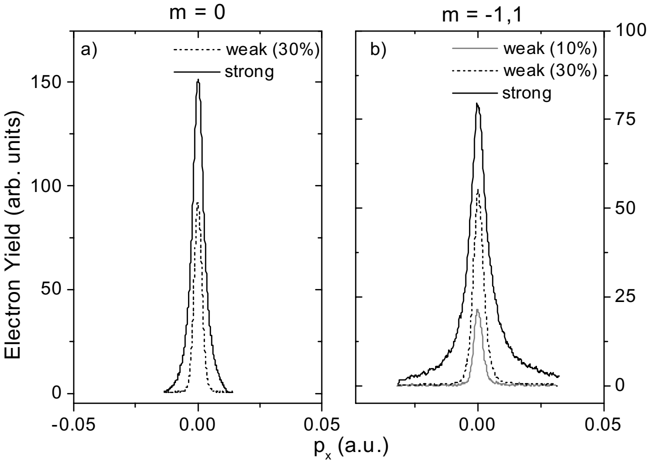

Figure 5.5: *Measured momentum distributions in the x-direction after HCP ionization of a) $m = 0$ Rydberg state and b) $m = \pm 1$ Rydberg state with the HCP polarized in the z-direction at low kick strength (10% and 30% ionization) and at high kick strength ($\sim$ 100% ionization).*

tion, $\Delta p = 6 \cdot 10^{-2}$ a.u.). In Fig. 5.5a an $m = 0$ Rydberg state was ionized and in Fig. 5.5b an $m = \pm 1$ Rydberg state. Note that the p_x axis was calibrated experimentally. Momentum differences as small as $\Delta p = 0.005$ a.u. can easily be resolved with the present imaging setup. Again, no difference was observed between a downhill or uphill kick. Therefore only the downhill kick is plotted. One clearly observes the broadening of the distribution upon larger kick strength. At low kick strength only the electrons escape with high momentum in the kick direction (z-direction), and therefore corresponding low momentum in the directions perpendicular to the kick (x- and y-direction). The measured momentum distribution is influenced by the focusing effect of the combined Coulomb potential and external static electric field. At high kick strengths we will show in this chapter that a HCP kick does not influence the momentum distribution in the directions perpendicular to the kick and that we measure the momentum distribution of the initial Rydberg state. The required kick strength has to be sufficiently strong such that the excited electron is little affected by the Coulomb force of the ionic core. This is true at high kick strength, where the energy transfer by the HCP is $\gg$10 meV. The sudden displacement of the electron in the direction of the kick (z-direction) reduces the long range influence of the Coulomb force. Therefore, although the measured p_x- and p_y-momentum are small, the long range influence of the Coulomb force can be neglected. In order to sample the whole

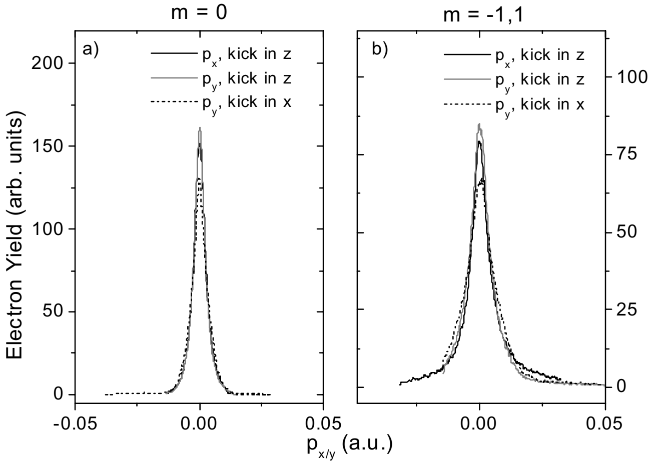

Figure 5.6: *Measured momentum distributions in the x- and y-direction for a HCP polarized in the z-direction and measured momentum distribution in the y-direction for a HCP polarized in the x-direction of a) $m = 0$ Rydberg state and b) $m = \pm 1$ Rydberg state. When a HCP kick changes the momentum of the electron only in the direction of the kick, these measured distributions should be equal.*

wave function without bias, the ionization probability has to be close to 100%.

An empirical method of corroborating the influence of the HCP in directions perpendicular to the kick in our experiment is to compare the momentum distribution in the x- and y-direction when kicking along the electric field in the z-direction with the momentum distribution in the y-direction upon kicking in the x-direction. In all of these cases the observed distributions should closely resemble each other as the same momentum distribution is being imaged. The p$_x$-, p$_y$-distribution after a parallel kick and the p$_y$-distribution after a perpendicular kick are compared in Fig. 5.6 ($\sim$ 100% ionization), in Fig. 5.6a for an $m = 0$ Rydberg state and in Fig. 5.6b for an $m = \pm 1$ Rydberg state. The measured momentum distributions are similar. We consider these observations to provide strong experimental indication that the HCP ionization process conserves to a large degree the momentum distribution perpendicular to the kick direction. Formally, the possibility exists that in all three cases a similar distortion takes place in going from the initial to the final observed momentum distribution. The fact that the results do not depend on the kick direction of electron ejection makes this unlikely. The momentum distributions of an $m = 0$ Rydberg state are narrower than the momentum distributions of an $m = \pm 1$ Rydberg state. A priori, the differ-

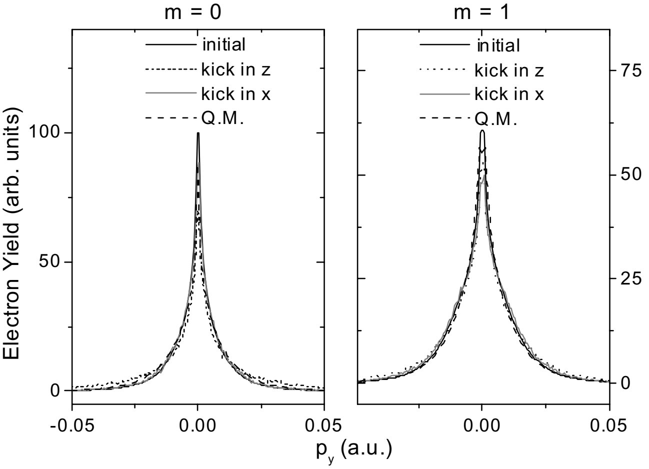

Figure 5.7: *Comparison of calculated initial momentum distributions in the y-direction with the calculated distribution after HCP ionization for a HCP kick in the z-direction and in the x-direction. For kicks in the z-direction the coulomb scattering has some influence on the final momentum distribution. Quantum mechanical calculations of the momentum distribution of the initial Rydberg state are included.*

ence in initial preparation ($m = 0$ versus $m = \pm 1$) with the dye laser was expected to be very small. Although initially at small angular-momentum values the difference is large, most of the time the atoms have much larger l-values (up to $l = 33$), for which a difference of one unit in the magnetic quantum number is expected to be insignificant. The increase in width of the $m = \pm 1$ momentum distribution is the influence of the centrifugal barrier in the potential keeping the electrons away from the z-axis. The incoherent superposition of many k-states results in the disappearance of the nodal structure, often associated with a wave function.

Both the initial momentum distribution of the Rydberg state and expected velocity map images after HCP ionization were calculated classically in order to prove that the HCP does not change the momentum distributions perpendicular to the kick. The calculated initial momentum distribution were taken equal in the x- and y-direction, as expected because of cylindrical symmetry around the electric field axis (z-axis). The calculated initial momentum distribution in the y-direction is plotted in Fig. 5.7 together with the momentum distribution after the HCP kick (polarized in the z- and x-direction) for both a) $m = 0$ and b) $m = \pm 1$. The calculated initial p_y-momentum distribution is equal to the calculated p_y-momentum distribution after

HCP ionization, corroborating that a HCP kick has no influence on the momentum distributions perpendicular to the kick direction. If the Coulomb force would affect the momentum distributions because of the long-range character of this interaction, this would show up in these calculations. One small distortion is observed in the classical calculations for the case of a kick in the z-direction. The classical calculations indicate that electrons present on the z-axis and that come close to the core after HCP interaction, undergo large angular scattering of the ionic core, enlarging significantly the momentum in the directions perpendicular to the z-axis. This effect is observed in Fig. 5.7a in the form of an increase in intensity in the wings of the distribution. This phenomenon is found to occur only for HCP polarization in the z-direction, and not for polarization in the x-direction. The absence of this phenomenon in our experiments may reflect that the impact of Coulomb scattering is an artifact of the classical calculations, where the ionic core is a point charge. Also the classical calculations show a clear difference in width between an $m = 0$ Rydberg state and an $m = \pm 1$ Rydberg state. Both experimental data and calculations show that the fact that the interaction is not sudden (1 ps FWHM of the HCP compared to 6 ps roundtrip time of the electron) does not influence the momentum distribution.

To check the classical calculations we have performed also a series of quantum calculations, determining the momentum distribution of a superposition of all possible k-states in one manifold ($n = 34$) in hydrogen. The quantum mechanical results are included in Fig. 5.7; these calculations agree very well with the classical calculations, proving the reliability of the latter calculations.

We conclude that our experiment yields reliable and accurate momentum maps of highly excited wavefunctions in a complex atom.

5.5 Discussion and Conclusion

In the description of the results, the HCP was assumed to be a true half-cycle pulse. However, it is well known that after some propagation, the main HCP peak is followed by a long weak tail with small amplitude. The impact of this tail has been studied in a small number of publications [13, 14]. It has been reported that the presence of this weak tail affects the ionization efficiency for very high Rydberg states ($n >> 80$) [14]. In Chapter 4 we have described the effect of the full-cycle character on the asymptotic velocity of the electrons. We showed that the tail does not affect the ionization behavior and yield. The tail only changes the velocity of the ionized electrons after ionization. Figure 5.8 shows results looking at momentum distributions after ionization in the direction of the kick and hence influenced by the kick. In Fig. 5.8a the experimental data are plotted for both an initial $m = 0$ and $m = \pm 1$ Rydberg state. In Fig. 5.8b the corresponding calculations are plotted using both a true half-cycle pulse and a full-cycle pulse. Clearly the influence of the tail is shown in Fig. 5.8b. A true HCP gives a significantly displaced momentum distribution.

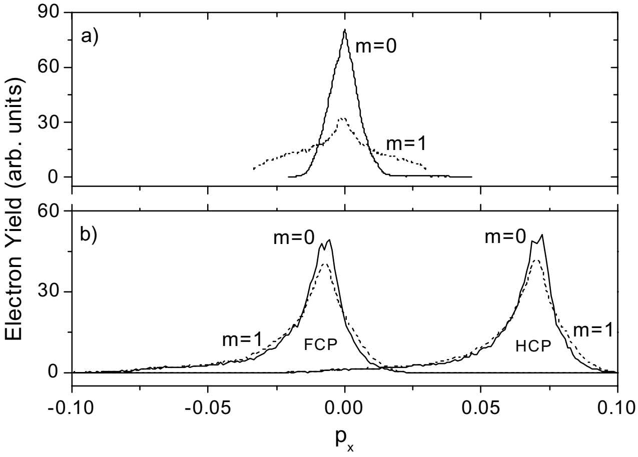

Figure 5.8: *Momentum distribution in the x-direction after ionization with the HCP polarized in the x-direction, in Fig. a) the measured data and in Fig. b) the calculated distribution.*

However, the tail shifts the distribution back without changing its shape (Chapter 4). The measured momentum distributions are centered around zero momentum, whereas the calculated distributions are shifted slightly opposite to the kick. The shift back in the experiment is slightly less than in the calculation because in the experiment the electron experiences a weaker tail when it moves out of the interaction region. The measured final momentum distribution is again significantly different starting from an $m = 0$ or $m = \pm 1$ Rydberg state. For kicks in the z-direction no influence of the tail could be observed, as the velocity changes occurred in the direction perpendicular to the detector.

Comparison of our experimental ionization curve with classical and quantum mechanical calculations suggest at low kick strengths metastable atoms having final energies in the ionization continuum that do not find the saddle point. Just above the saddle point quasi-bound levels exist which have enough energy to ionize, but avoid the saddle point in the three dimensional Coulomb potential. In Chapter 4 we noticed that for perpendicular kicks also metastable states exist at low kick strengths. This is partially due to the excitation of large m values. During the interaction with a HCP kick perpendicular to the electric field, m is not conserved and increases rapidly. Excitation of large m values enhances the centrifugal potential, keeping the electron away from the electric field axis and raises the threshold field. In Chapter 4 we saw that metastable electrons with low m values can reorient via core scattering their orbit in the direction of the saddle point and escape. At low kick strengths the measured ionization yield was higher than the calculated ionization yield. This 'extra' ionization yield agreed with $l_z < 1$ states which had enough energy to escape, but did not do in the classical hydrogen like calculation. In the interaction with a HCP kick parallel to the electric field, m is conserved. If core scattering would be efficient, we would expect all the metastable states to ionize. Maybe we overestimated the contribution of $l_z < 1$ states to core scattering. It can be possible that not all the metastable states with low angular momentum and energy above the saddle point ionize during the detection time. Lankhuijzen *et al.* [19,20] observed long-lived states for laser excitation just above the saddle point (1 meV) with lifetimes up to several microseconds. A more quantitative calculation involving core scattering would be necessary to simulate the measured ionization curves more precisely.

Comparing the calculated initial momentum distribution with the measured momentum distribution, we see that the latter is narrower than the calculated one. The observed momentum distribution has more a Gaussian shape as distinct from a Lorentzian shape in the calculated momentum distribution. Both the classical calculations and quantum mechanical calculations are done for hydrogen. The influence of the xenon core is neglected. For a precise quantitative comparison between calculations and measurement the exact composition of the initial state should be taken into account in the calculations. Experimentally an incoherent superposition of certain k-states in the n-mixing regime is excited, which is difficult to describe exactly in the calculations.

The present results indicate a novel way of obtaining two-dimensional momentum images using HCP ionization. HCP ionization has already been used in an indirect method to retrieve the one-dimensional momentum distribution by Jones and coworkers [9,31]. As described earlier, here the momentum distribution is obtained from the derivative of the ionization yield curve, which makes this method very sensitive to experimental noise. The present method is more direct and adds an extra dimension. It can be better compared to the electron momentum spectroscopy [89,90] that however as complicating factor requires the coincident detection of incident and ionized electron.

In the present experiment, we have imaged a mixture of k-states of xenon incoherently excited in a static electric field. It would be of great interest to use atomic hydrogen for this research. In the case of a hydrogen atom the orbit would not precess because of interaction between the core and the electron. Therefore the symmetry between the x-and y-direction as was observed in the present experiments would not exist. The advantage of the study of laser-generated Rydberg states is the possibility to image time-dependent wave functions in a time-resolved pump-probe experiment using a subpicosecond laser pulse in combination with the subpicosecond HCP as has been achieved by Jones and coworkers for the one-dimensional momentum distribution [9,31].

In this chapter we have determined momentum distributions of highly excited

Rydberg states in the n-mixing regime. It would be desirable to extend this method to field-free Rydberg states and to lower-lying states. Velocity-map imaging has been done for the much slower fragment ions of molecular fragmentation created in field-free conditions using delayed pulsed field extraction by Gebhardt *et al.* [93]. Hence, in principle, field-free electron momentum distributions may be measured. Recent developments in the generation of very few-cycle radiation [95] with a few femtosecond duration may open the possibility for the study of lower-lying Rydberg states.

In summary: we have shown that our two-dimensional maps directly reflect the momentum distributions in two dimensions. This has become possible because of the advent of ultrafast HCP in combination with the imaging techniques. Consistency is found when comparing different measurement geometries and when comparing the calculated initial momentum distributions with the expected velocity map images. The system used in the present experiment showed a large amount of symmetry because of the presence of core scattering associated with the complex nature of the xenon core.

Bibliography

[1] J.C. Maxwell, *A Treatise on Electricity and Magnetism,* (1873).

[2] T.W. Hänsch, *Appl. Opt.*, **11**, 895 (1972).

[3] E. Schrödinger, *Die Naturwissenschaften* **28**, 664 (1926).

[4] G. Alber, H. Ritsch, and P. Zoller, *Phys. Rev. A* **34**, 1058 (1986).

[5] J. Parker and C.R. Stroud, Jr., *Phys. Rev. Lett.* **56**, 716 (1986).

[6] J.A. Yeazell and C.R. Stroud Jr., *Phys. Rev. Lett.* **60**, 1494 (1988).

[7] A. ten Wolde, L.D. Noordam, A. Lagendijk, and H.B. van Linden van den Heuvell, *Phys. Rev. Lett.* **61**, 2099 (1988).

[8] N.E. Tielking and R.R. Jones, *Phys. Rev. A* **52**, 1371 (1995).

[9] R.R. Jones, *Phys. Rev. Lett.* **76**, 3927 (1996).

[10] C.O. Reinhold, J. Burgdörfer, M.T. Frey, and F.B. Dunning, *Phys. Rev. A* **54**, R33 (1996).

[11] C.O. Reinhold, J. Burgdörfer, M.T. Frey, and F.B. Dunning, *Phys. Rev. Lett.* **79**, 5226 (1997).

[12] M.T. Frey, F.B. Dunning, C.O. Reinhold, S. Yoshida, and J. Burgdörfer, *Phys. Rev. A* **59**, 1434 (1999).

[13] N.E. Tielking, T.J. Bensky, and R.R. Jones, *Phys. Rev. A* **51**, 3370 (1995).

[14] C. Wesdorp, F. Robicheaux, and L.D. Noordam, *Phys. Rev. Lett.* **87**, 083001 (2001).

[15] F. Robicheaux, *Phys. Rev. A* **56**, R3358 (1997).

[16] T.F. Gallagher, *Rydberg Atoms*, (Cambridge University Press, Cambridge, UK, 1994).

[17] R.F. Stebbings and F.B. Dunning, *Rydberg States of Atoms and Molecules*, (Cambridge University Press, Cambridge, USA, 1983).

[18] J.R. Rydberg, *Phil. Mag.* **29**, 331 (1890).

[19] G.M. Lankhuijzen and L.D. Noordam, *Phys. Rev. A* **52**, 2016 (1995)

[20] G.M. Lankhuijzen and L.D. Noordam, Phys. Rev. Lett. **76**, 1784 (1996).

[21] L.D. Noordam, A. ten Wolde, A. Lagendijk, and H.B. van Linden van den Heuvell, *Phys. Rev. A* **40**, 6999 (1989).

[22] C. Raman, W.S. Conover, C.I. Sukenik, and P.H. Bucksbaum, *Phys. Rev. Lett.* **76**, 2436 (1996).

[23] M.T. Frey, F.B. Dunning, C.O. Reinhold, and J. Burgdörfer, *Phys. Rev. A* **55**, R865 (1997).

[24] M.T. Frey, F.B. Dunning, C.O. Reinhold, and J. Burgdörfer, *Phys. Rev. A* **53**, R2929 (1996).

[25] R.R. Jones, D. You, and P.H. Bucksbaum, *Phys. Rev. Lett.* **70**, 1236 (1993).

[26] C.O. Reinhold, M. Melles, H. Shao, and J. Burgdörfer, *J. Phys. B* **26**, L659 (1993).

[27] A. Bugacov, B. Piraux, M. Pont, and R. Shakeshaft, *Phys. Rev. A* **51**, 1490 (1995).

[28] I. Bersons and A. Kulsh, *Phys. Rev. A* **59** 1399 (1999).

[29] R.R. Jones, N.E. Tielking, D. You, C. Raman, and P.H. Bucksbaum, *Phys. Rev. A* **51**, R2687 (1995).

[30] A. Bugacov, B. Piraux, M. Pont, and R. Shakeshaft, *Phys. Rev. A* **51**, 4877 (1995).

[31] M.B. Campbell, T.J. Bensky, and R.R. Jones, *Phys. Rev. A* **58**, R514 (1998).

[32] O. Zobay and G. Alber, *Phys. Rev. A* **60**, 1314, (1999).

[33] A.T.J. Eppink and D.H. Parker, *Rev. Sci. Instrum.* **68**, 3477 (1997).

[34] H.L. Offerhaus, C. Nicole, F. Lépine, C. Bordas, F. Roşca-Prună, and M.J.J. Vrakking, *Rev. Sci. Instrum.* **72**, 3245 (2001).

[35] C.J. Dasch, *Appl. Opt.* **31**, 1146 (1992).

[36] M.J.J. Vrakking, *Rev. Sci. Instrum.* ***72**, 4084 (2001).*

[37] C. Bordas, *Phys. Rev. A* **58**, 400 (1998).

[38] C. Nicole, I. Sluimer, F. Roşca-Prună, M. Warntjes, M. Vrakking, C. Bordas, F. Texier, and F. Robicheaux, *Phys. Rev. Lett.* **85**, 4024 (2000).

[39] C. Nicole, H.L. Offerhaus, M.J.J. Vrakking, F. Lépine, and C. Bordas, *Phys. Rev. Lett.* **88**, 133001 (2002).

[40] J.T. Darrow, B.B. Hu, X.-C. Zhang, and D.H. Auston, *Opt. Lett.* **15**, 323 (1990).

[41] B.B. Hu, J.T. Darrow, X.-C. Zhang, and D.H. Auston, *Appl. Phys. Lett.* **56**, 886 (1990).

[42] D. You, R.R. Jones, and P.H. Bucksbaum, *Opt. Lett.* **18**, 290 (1993).

[43] B.B. Hu, X.-C. Zhang, and D.H. Auston, *Phys. Rev. Lett.* **67**, 2709 (1991).

[44] X.-C. Zhang, B.B. Hu, J.T. Darrow, and D.H. Auston, *Appl. Phys. Lett.* **56**, 1011 (1990).

[45] X.-C. Zhang, X.F. Ma, Y. Jin, and T.-M. Lu, *Appl. Phys. Lett.* **61**, 3080 (1992).

[46] Q. Wu and X.-C. Zhang, *Appl. Phys. Lett.* **67**, 3523 (1995).

[47] A. Nahata, D.H. Auston, T.F. Heinz, and C. Wu, *Appl. Phys. Lett.* **68**, 150 (1996).

[48] P.U. Jepsen, C. Winnewisser, M. Schall, V. Schyja, S.R. Keiding, and H. Helm, *Phys. Rev. E* **53**, R3502 (1996).

[49] B.I. Greene, J.F. Federici, D.R. Dykaar, A.F.J. Levi, and L. Pfeiffer, *Opt. Lett.* **16**, 48 (1991).

[50] P.R. Smith, D.H. Auston, and M.C. Nuss, *IEEE* **24**, 255 (1988).

[51] B.I. Greene, J.F. Federici, D.R. Dykaar, R.R. Jones, and P.H. Bucksbaum, *Appl. Phys. Lett.* **59**, 893 (1991).

[52] Z. Jiang and X.-C. Zhang, *IEEE* **36**, 1214 (2000).

[53] Z. Jiang, F.G. Sun, and X.-C. Zhang, *Opt. Lett.* **24**, 1245 (1999).

[54] Z. Jiang, F.G. Sun, Q. Chen, and X.-C. Zhang, *Appl. Phys. Lett.* **74**, 1191 (1999).

[55] T.R. Sliker and J.M. Jost, *J. Opt. Soc. Am.* **56**, 130 (1966).

[56] M. Schall and P.U. Jepsen, *Opt. Lett.* **25**, 13 (2000).

[57] M. Exter, C. Fattinger, and D. Grischkowsky, *Opt. Lett.* **14**, 1128 (1989).

[58] P.U. Jepsen and S.R. Keiding, *Opt. Lett.* **20**, 807 (1995).

[59] A.J. Alcock, P.B. Corkum, and D.J. James, *Appl. Phys. Lett.* **27**, 680 (1975).

[60] P.B. Corkum, A.J. Alcock, D.F. Rollin, and H.D. Morrison, *Appl. Phys. Lett.* **32**, 27 (1978).

[61] S.A. Jamison and A.V. Nurmikko, *Appl. Phys. Lett.* **33**, 598 (1978).

[62] C. Rolland and P.B. Corkum, *J. Opt. Soc. Am. B* **3**, 1625 (1986).

[63] A.Y. Elezzabi, J. Meyer, M.K.Y. Hughes, and S.R. Johnson, *Opt. Lett.* **19**, 898 (1994).

[64] H. Salzmann, T. Vogel, and G. Dodel, *Opt. Commun.* **47**, 340 (1983).

[65] T. Vogel, G. Dodel, E. Holzhauer, H. Salzmann, and A. Theurer, *Appl. Opt.* **31**, 329 (1992).

[66] M.C. Nuss, D.H. Auston, and F. Capasso, *Phys. Rev. Lett.* **58**, 2355 (1987).

[67] F.A. Hegmann and M.S. Sherwin, *SPIE* **2842**, 90 (1996).

[68] N.W. Aschcroft and N.D. Mermin, *Solid State Physics*, (Saunders College, Philadelphia, 1976).

[69] S.M. Sze, *Physics of Semiconductor Devices*, (John Wiley & Sons, New York, USA, 1981).

[70] G.M.H. Knippels, M.J. van de Pol, H.P.M. Pellemans, P.C.M. Planken, and A.F.G. van der Meer, *Opt. Lett.* **23**, 1754 (1998).

[71] Z. Jiang and X.-C. Zhang, *Appl. Phys. Lett.* **72**, 1945 (1998).

[72] Z. Jiang and X.-C. Zhang, *Opt. Lett.* **23**, 1114 (1998).

[73] F.G. Sun, Z. Jiang, and X.-C. Zhang, *Appl. Phys. Lett.* **73**, 2233 (1998).

[74] Y. Cai, I. Brener, J. Lopata, J. Wynn, L. Pfeiffer, J.B. Stark, Q. Wu, X.-C. Zhang, and J.F. Federici, *Appl. Phys. Lett.* **73**, 444 (1998).

[75] G.M.H. Knippels, X. Yan, A.M. MacLeod, W.A. Gillespie, M. Yasumoto, D. Oepts, and A.F.G. van der Meer, *Phys. Rev. Lett.* **83**, 1578 (1999).

[76] A.M. MacLeod, X. Yan, W.A. Gillespie, G.M.H. Knippels, D. Oepts, A.F.G. van der Meer, C.W. Rella, T.I. Smith, and H.A. Schwettman, *Phys. Rev. E* **62**, 4216 (2000).

[77] J.R. Fletcher, *Optics Express* **10**, 1425 (2002).

[78] P.C.M. Planken, H.-K. Nienhuys, H.J. Bakker, and T. Wenckebach, *J. Opt. Soc. Am. B* **18**, 313 (2001).

[79] R.B. Vrijen, G.M. Lankhuijzen, and L.D. Noordam, *Phys. Rev. Lett.* **79**, 617 (1997).

[80] C. Raman, T.C. Weinacht, and P.H. Bucksbaum, *Phys. Rev. A* **55**, R3995 (1997).

[81] M.B. Campbell, T.J. Bensky, and R.R. Jones, *Phys. Rev. A* **59**, R4117 (1999).

[82] J.A. Yeazell, M. Mallalieu, and C.R. Stroud Jr, *Phys. Rev. Lett.* **64**, 2007 (1990).

[83] Z.D. Gaeta and C.R. Stroud Jr., *Phys. Rev. A* **42**, 6308 (1990).

[84] J. Bromage and C.R. Stroud Jr., *Phys. Rev. Lett.* **83**, 4963 (1999).

[85] J. Picart, A.R. Edmonds, and N. Tran Minh, *J. Phys. B* **11**, L651 (1978)

[86] H.A. Bethe, and E.E. Salpeter, *Quantum Mechanics of One- and Two-Electron Atoms*, paperback edn. (Plenum, New York, 1977).

[87] I. Bersons, and A. Kulsh, *Phys. Rev. A* **60**, 3144 (1999).

[88] A. Kohlhase and S. Kita, *Rev. Sci. Instrum.* **57**, 2925 (1986).

[89] E. Weigold, S.T. Hood, and P.J.O. Teubner, *Phys. Rev. Lett.* **30**, 475 (1973).

[90] S.T. Hood, I.E. McCarthy, P.J.O. Teubner, and E. Weigold, *Phys. Rev. A* **8**, 2494 (1973).

[91] H.G. Muller, *Laser Phys.* **9**, 138 (1999).

[92] F. Robicheaux (*private communication*).

[93] C.R. Gebhardt,T.P. Rakitzis,P.C. Samartzis,V. Ladopoulos , and T.N. Kitsopoulos, *Rev. Sci. Instrum.* **72**, 3848 (2001).

[94] C.O. Reinhold, J. Burgdörfer, R.R. Jones, C. Raman, and P.H. Bucksbaum, *J. Phys. B* **28**, L457 (1995).

[95] A. Baltuska, T. Udem, M. Uiberacker, M. Hentschel, E. Goulielmakis, C. Gohle, R. Holzwarth, V.S. Yakoviev, A. Scrinzi, T.W. Hänsch, and F. Krausz, *Nature* **421**, 611 (2003).

Summary

This thesis deals with the impulsive interaction between half-cycle radiation and Rydberg atoms. In most situations, the photon picture is used in describing the interaction between radiation and matter; radiation is considered as a stream of photons with an energy determined by the wavelength. During the interaction photons are absorbed or emitted.

Our matter is a Rydberg atom. In a Rydberg atom the outer electron is excited to a highly excited state. One of the most important aspects of Rydberg states is their rapid increase in size when higher lying states are excited. Due to the large average distance between the Rydberg electron and the nucleus these atoms are sensitive to relative small laboratory fields, which can influence the dynamics of Rydberg electrons significantly. Also the roundtrip time of the Rydberg electron around the core is large. The roundtrip time of a typical ground state is less than one femtoseconds, whereas the roundtrip time of a Rydberg electron is in the picosecond regime.

Our radiation is the so-called half-cycle pulse. This electromagnetic radiation propagates freely in space as a single half-cycle with a frequency spectrum in the terahertz regime. The pulse duration of this half-cycle is 0.5-1 picoseconds. Due to diffraction of the slow components, the strong main peak is followed by a second much longer and weaker half-cycle. This 'tail' is often longer (10 - 100 picoseconds) than the roundtrip time of an electron, and can therefore be neglected. The interaction between a half-cycle pulse and a Rydberg atom can be described as impulsive. The half-cycle pulse kicks the electron in the direction opposite to its electric field. The energy absorbed or emitted is determined by the field strength and the direction of the kick compared with the velocity direction of the electron at the moment of the kick. In the case of the interaction between a half-cycle pulse radiation and matter, the electric field strength is crucial and not the photon energy. This impulsive character often makes a classical description of the interaction of a half-cycle pulse with a Rydberg electron possible. The effect of the impulsive interaction can be calculated by Newton's laws.

Rydberg atoms are easily created by laser excitation since the development of the dye laser in the beginning of the 1970s. The generation of half-cycle pulses is only developed since the beginning of the 1990s. The technique to generate and detect

half-cycle pulses is described in Chapter 2. The most common method to generate half-cycle radiation is by illumination of a semiconductor with a femtosecond infrared laser pulse. The photon energy of this laser is above the band gap energy. Upon illumination electrons and holes are created, which are accelerated by an applied bias. The radiated electric field is proportional to the change in carrier density, which is proportional to the incident optical intensity of the femtosecond laser. This results in radiation of a half cycle electric field oscillation. The generation of half-cycle pulses involves strong electronic noise, which disturbs the signal of many experiments. We found a method to suppress this electronic noise. By putting a RC circuit over the wafer, which acts as a local power supply, the electronic noise is reduced significantly. In Chapter 2 we also describe the generation of few cycle radiation. Few cycle radiation would be very useful to investigate the regime between multi-cycle optical light and half cycle radiation, i.e. the transition from the 'photon' picture to the regime where the electric field strength is crucial. In Chapter 2 we show preliminary results of few-cycle pulse generation. To generate few-cycle radiation we sliced the back part from a multi-cycle optical pulse using a fast switchable mirror. Our multi-cycle optical pulse source was the Free Electron Laser at the FOM Institute for Plasmaphysics in Rijnhuizen. The mirror, which is a semiconductor waver, is switched by illumination of a short, intense femtosecond pulse. The intense femtosecond pulse creates an electron plasma by which the mirror turns from transparent to reflective.

Wavepackets are generated by coherent excitation of several eigenstates with a short laser pulse. Often femtosecond radiation from a Ti:Sapphire laser is used, but half-cycle pulses can also be used to generate a wavepacket. Chapter 3 describes to the properties of a wavepacket generated with a half-cycle pulse. A wavepacket evolves in time. In contradiction with a wavepacket generated with a multi-cycle optical pulse, the wavepacket is initially delocalized and becomes localized after half a revival time. A multi-cycle optical pulse excites the population near the core, whereas a half-cycle pulse can excite the population along the whole orbit. A second half-cycle pulse is used to manipulate the populations of the eigenstates in the wavepacket. Because of the evolution in time of the wavepacket the population change involved with the second half-cycle pulse depends on the time difference between the two half-cycle pulses. The whole population change could be described with a semi-classical picture.

In the last two chapters we used a specially designed detector, the velocity-map imaging detector. This detector registers the momentum of the electron in the plane of the detector. Due to the insertion of an electrostatic lens the detector can measure the electron momentum associated with very low kinetic energies of only a few meV. With this detector we measured the momentum distribution of the electrons after HCP ionization. In a static electric field Rydberg states just below the saddle point were ionized by a HCP. The half-cycle pulse was polarized either perpendicular or parallel to the detector. In Chapter 4 we focused on the detection of the momentum of the electron in the kick direction. In this case the presence of the slow tail of the HCP was clearly visible. Before the tail of the HCP was often neglected and indeed no influence on the ionization yield was observed. However the influence of the tail on the final momentum distribution was large. To our surprise the measured momentum of the ionized electrons was very low, much lower than the momentum kick given by the half-cycle pulse. Classical calculations were necessary to explain the measurements. These calculations showed that indeed high kinetic electrons were generated if the tail of the half-cycle pulse was neglected. When this tail was taken into account very low kinetic energy electrons were generated. The kick of the tail is in opposite direction than the main kick and much weaker, but the electron experiences the kick much longer. Therefore, the energy gained by the interaction of the main half-cycle pulse was reduced during the interaction with the tail.

In Chapter 5 we proved experimentally and theoretically that the combination of half-cycle pulse ionization together with the velocity imaging detector is a good tool for momentum spectroscopy of the wavefunction of a Rydberg atom. During the interaction the half-cycle pulse only changes the momentum in the direction of the kick, the momentum in the other two directions is conserved during the interaction and can be measured with the velocity imaging detector. Two conditions are important for its success. The ionization cross section does not depend on the momentum of the electron, 100% ionization yield can be easily achieved. Secondly the interaction can be viewed as a sudden process. In a Rydberg state the pulse duration is much shorter than the roundtrip time of the electron around the core. To prove that the HCP only changes the momentum of the electron in the direction of the kick, we compared the momentum distributions perpendicular to the kick direction for two different HCP polarizations. Classical calculations also proved that the HCP interaction only changes the momentum of the electron in the kick direction. Due to the complicated initial state, an incoherent superposition of different k-states in the n-mixing regime, it was not possible to calculate the exact initial distribution. Therefore some differences existed between the measured and calculated momentum distributions. But both the experimental data as the theoretical data showed that an initial state with magnetic quantum number $m = 0$ is narrower than an initial state with magnetic quantum number $m = 1$, although most of the time the electron is in a high angular momentum state, for which a difference of one unit in the magnetic quantum number is expected to be insignificant.

This work has contributed to a better understanding of the interaction with specially designed radiation, ultrashort half-cycle pulses, and Rydberg atoms. The combination has provided new tools for manipulation of electron motion in atoms and for the mapping of the electron wave function, the important and non-intuitive aspect of modern quantum mechanics.

Samenvatting

In dit proefschrift wordt de wisselwerking tussen ‘speciale electromagnetische straling’ en een Rydberg atoom beschreven. In de meeste situaties wordt een fotonbeeld gebruikt om de wisselwerking tussen straling en materie te beschrijven; straling wordt dan beschouwd als een bundel energetische deeltjes (= fotonen) waarvan de energy bepaald wordt door de golflengte van de straling. Tijdens de wisselwerking tussen electromagnetische straling en materie worden fotonen geabsorbeerd of gegenereerd (= uitgezonden door materie).

Onze materie is het zogenaamde Rydberg atoom. In een Rydberg atoom bevindt het buitenste electron zich in een hoog aangeslagen toestand. Eén van de meest belangrijke aspecten van een Rydberg toestand is hun snelle toename in grootte wanneer een hoger aangeslagen toestand wordt bezet. Door de grote afstand tussen het Rydberg electron en de kern zijn deze atomen gevoelig voor relatief kleine electrische velden, die de dynamica van de Rydberg electronen aanzienlijk kunnen beïnvloeden. Ook de rondlooptijd van het electron rond de kern is groot. Een typische grondtoestand heeft een rondlooptijd in de orde van grootte van minder dan één femtoseconde (een miljoenste van een miljardste van een seconde). De rondlooptijd van een Rydberg electron is daarentegen in de orde van een paar picoseconde (een miljoenste van een miljoenste van een seconde).

Onze straling is de zogenaamde ‘halve golf’. Deze electromagnetische straling bestaat uit slechts één halve oscillatie. De golf plant zich in de vrije ruimte voort. Het frequentie bereik ligt in het Terahertz gebied (een miljoen keer een miljoen hertz). De pulsduur van zo’n halve golf is 0.5 tot 1 picoseconde. Door de diffractie van de langzame componenten wordt de sterke hoofdpiek gevolgd door een tweede veel langere en zwakkere halve golf. Deze ‘staart’ (10 tot 100 picoseconde) is vaak langer dan de rondlooptijd van het electron, en kan daardoor genegeerd worden. De wisselwerking tussen een halve golf en een Rydberg atoom kan gezien worden als een plotselinge verstoring of ‘trap’. De halve golf trapt het electron in tegengestelde richting van het electrisch veld van de golf. De geabsorbeerde of vrijgekomen lichtenergie wordt bepaald door de veldsterkte en de richting van de trap ten opzichte van de richting waarin het electron beweegt op het moment van de trap. In het geval van de wisselwerking tussen de halve golf en de materie is de electrische veldstrekte van belang en niet de energy van de fotonen. Dit botsingskarakter maakt een klassieke beschrijving van de wisselwerking van een halve golf met een Rydberg electron mogelijk. Het effect van de botsing kan berekend worden met behulp van de klassieke bewegingswetten van Newton.

Rydberg atomen kunnen sinds de ontwikkeling van de kleurstoflaser in het begin van de zeventiger jaren makkelijk gecreëerd worden. Het maken van halve golven is pas aan het begin van de negentiger jaren ontwikkeld. De techniek om halve golven te maken en te meten wordt beschreven in Hoofdstuk 2: De meest gebruikte methode om halve golven te maken is het belichten van een halfgeleider met een femtoseconde infrarood laser. De fotonenergie van deze laser is groot genoeg om de afstand tussen de geleidingsband en valentieband te overbruggen. Belichting van de halfgeleider met een infrarood laser genereert dan ook electronen en gaten in deze banden. Deze electronen en gaten worden versneld door een electrisch veld, dat aangelegd is over de halfgeleider. De verandering in de dichtheid van de ladingsdragers is rechtevenredig met de inkomende intensiteit van de femtoseconde laser en genereert nieuwe straling. Dit resulteert in straling die uit een halve oscillatie bestaat. Het maken van een halve golf veroorzaakt sterke ruis, die het signaal van vele experimenten verstoort. Wij hebben een methode ontworpen om deze electronische ruis te onderdrukken. Door het plaatsen van een RC circuit over de halfgeleiderplaat werd de electronische ruis aanzienlijk verminderd. Het RC circuit doet dienst als lokale voeding. In Hoofdstuk 2 beschrijven we ook de generatie van straling bestaande uit een paar, in aantal varieerbare, golven. Deze straling bestaande uit enkele golven zou erg nuttig zijn om het gebied tussen straling bestaande uit een halve golf en uit ‘veel’ golven, dat wil zeggen de overgang van het fotonenbeeld naar het gebied waar de veldsterkte van belang is, te onderzoeken. Deze straling bestaande uit enkele golven wordt gemaakt door de achterkant van een lange golftrein af te knippen met behulp van een snelle schakelaar. De stralingsbron van de IR golftreinen is de Vrije Electronen Laser op het FOM Instituut voor Plasmafysica in Rijnhuizen, bekend onder de naam FELIX . Als schakelaar wordt een halfgeleiderplaat gebruikt die door belichting met een korte femtoseconde puls spiegelend wordt gemaakt. De intense femtoseconde puls creëert een electronenplasma waardoor de halfgeleider van transparant opeens spiegelend wordt.

Golfpakketten worden gecreëerd door het tegelijkertijd aanslaan van een aantal eigentoestanden met een korte laserpuls. Vaak wordt de femtoseconde straling van een Ti:Saffier laser gebruikt, maar ook halve golven zijn geschikt om een golfpakket te maken. Hoofdstuk 3 beschrijft de eigenschappen van een golfpakket gemaakt met behulp van een halve golf. Binnen een golfpakket zijn grootheden als plaats en momentum niet meer stationair, ze veranderen in de tijd. Straling bestaande uit veel golven slaat de populatie bij de kern aan, hierdoor is de populatie in het begin op één plek geconcentreerd en verspreid zich later in de tijd. Een halve golf, daarentegen, slaat de populatie over de gehele baan aan. Hierdoor is het golfpakket allereerst verspreid over de gehele orbit en pas later op één plek geconcentreerd. In Hoofdstuk 3 wordt een tweede halve golf gebruikt om de populatie van de eigentoestanden in het golfpakket te manipuleren. Door de ontwikkeling in de tijd van het golfpakket zal de populatieverandering teweeggebracht door de tweede halve golf afhangen van het tijdsverschil tussen de twee halve golven. De veranderingen in populatie kunnen kwalitatief beschreven worden op grond van klassieke mechanica van de Rydberg electronen.

In de laatste twee hoofdstukken gebruiken we een speciaal ontworpen snelheidsmeter, die de snelheid van electronen kan meten. De snelheidsmeter kan electronen meten met heel lage kinetische energiën van slecht een paar milli-electronvolt (een duizendste van een volt). Met deze snelheidsmeter kunnen we de momentumverdeling van de electronen na ionisatie met een halve golf meten. In een statisch electrisch veld worden Rydberg toestanden die net onder het zadelpunt liggen geïoniseerd door een halve golf. In Hoofdstuk 4 richten we ons op snelheden van electronen gemeten in de traprichting. In dit geval was de aanwezigheid van de staart volgend op de halve golf zeer duidelijk. Vroeger werd deze staart vaak genegeerd. De staart had, zoals in de meeste experimenten bleek, geen invloed op de ionisatie opbrengst. Maar de invloed op de uiteindelijke momentumverdeling was erg groot. Tot onze verbazing was de gemeten momentumverdeling van de geïoniseerde electronen veel lager dan het momentum dat overgedragen werd door de halve golf tijdens de wisselwerking. Klassieke berekeningen waren nodig om deze metingen uit te leggen. De berekeningen lieten zien dat de halve golf inderdaad hoog kinetische electronen maakte wanneer de staart niet werd meegenomen. Wanneer de staart wel werd meegenomen in de berekeningen dan werden er laag kinetische electronen gemaakt. De trap van de staart is in tegengestelde richting aan de trap van de hoofdpiek. Ondanks dat deze trap zwakker is, ervaart het electron de trap langer, waardoor de energie gewonnen bij de wisselwerking met de hoofdpiek teniet wordt gedaan door de wisselwerking met de staart.

In Hoofdstuk 5 hebben we experimenteel en door middel van berekeningen laten zien dat de combinatie van ionisatie door een halve golf met een snelheidsdetector een nieuwe manier is om momentumspectroscopie te doen van de golffunctie van Rydberg atomen. Gedurende de wisselwerking verandert de halve golf alleen de snelheid van het electron in de richting van de trap, de snelheden in de andere twee richtingen loodrecht op de trap blijven onveranderd na de wisselwerking en kunnen gemeten worden met de snelheidsdetector. Twee voorwaarden zijn belangrijk voor het succes van deze methode. De ionisatie kans hangt niet af van de snelheid van het electron, 100% ionisatie wordt makkelijk bereikt. Ten tweede kan de wisselwerking als een plotseling proces worden gezien. De pulsduur van de halve golf is veel korter dan de rondlooptijd van het electron om de kern. Om te bewijzen dat de halve golf alleen de snelheid van het electron in de trap richting verandert vergelijken we de snelheden loodrecht op de trap richting voor twee verschillende polarisaties van de halve golf. Klassieke berekeningen bevestigen dat de wisselwerking met de halve golf alleen de snelheid van het electron in de trap richting verandert. Door de complexiteit van de begintoestand, een opsomming van verschillende k toestanden in een gebied waar de k toestanden van verschillende n's al mengen, en door het niet tegelijkertijd aanslaan van de toestanden, was het niet mogelijk de precieze beginverdeling te reconstrueren. Daardoor waren er kleine verschillen tussen de gemeten en berekende snelheidsverdelingen te zien. Zowel de experimentele data als de berekeningen lieten zien dat een begintoestand met magnetisch kwantum nummer $m = 0$ smaller is dan een begintoestand met magnetisch kwantum nummer $m = 1$, alhoewel het electron de meeste tijd in een baan met een hoog hoekmoment is, waarvoor een verschil van één in het magnetisch kwantum nummer onbelangrijk behoord te zijn.

Dit werk draagt bij tot een beter begrip van de wisselwerking van speciaal ontwikkelde straling, een zogenaamde halve zeer korte golf, met Rydberg atomen. De combinatie heeft bewezen goed gereedschap te zijn om de electronenbeweging in een atoom te manipuleren en om de momentumverdeling van de electronengolffunctie, een zeer belangrijk aspect van de kwantummechanica, te meten.

Acknowledgment

Aan het einde gekomen van dit proefschrift, is ook een einde gekomen aan mijn promotieonderzoek. Graag wil ik alle mensen bedanken die hebben bijgedragen aan het tot stand komen van dit proefschrift. Een aantal mensen wil ik in het bijzonder bedanken.

Allereerst Wim bedankt. Na het vertrek van Bart heb jij de begeleiding van mijn promotie overgenomen, en, heel belangrijk, tot een goed einde gebracht. Als mijn begeleider heb je je de afgelopen jaren intensief en met je alom bekende enthousiasme ingezet om dit proefschrift te verwezenlijken. Het ging niet altijd even gemakkelijk maar uiteindelijk hebben wij toch een mooi proefschrift afgeleverd.
De eerste jaren van mijn promotie heb ik in de groep van Bart gewerkt. Bart bedankt voor al je hulp aan het begin van mijn promotie. Je kennis van Rydberg atomen was daarbij van onschatbare waarde.
Theoretical support came from the other side of the ocean, from Francis. The world seems to become smaller and smaller but it is still hard to discuss scientific stuff by email. Francis thanks for all your effort and patience to understand my emails and to answer all my questions.
Nog meer theoretische kennis en de benodigde apparatuur voor het uitvoeren van experimenten kwam vaak uit andere groepen. Harm bedankt voor je eindeloze uitleg. Geen enkele vraag blijft bij jou onbeantwoord. De experimenten beschreven in Hoofdstuk 4 en 5 zijn uitgevoerd op de Hoohar- en Xtra-opstelling van Marc. Florentina en Sebastien hebben enorm geholpen met het uitvoeren van het experiment op Xtra. Catalin bedankt voor je berekeningen.
Een gedeelte van mijn promotieonderzoek heb ik uitgevoerd in Rijnhuizen. Hier heb ik nauw samengewerkt met Giel. Giel bedankt voor je medewerking, enthousiasme en hulp tijdens de Felix shifts die wel eens tot in de vroege uurtjes konden duren.
De samenwerking met de medewerkers van het programma Qdams heb ik als bijzonder prettig ervaren.

Naast de wetenschappelijke bijdrage zou zonder de technische ondersteuning dit proefschrift niet tot stand zijn gekomen.
Hinco en Rob bedankt. Jullie hulp was van onschatbare waarde. Behalve voor technische ondersteuning kon ik altijd bij jullie terecht voor de nodige mentale ondersteuning als het even tegen zat. Ook zorgden jullie voor de nodige dagelijkse afleiding.
Een groot gedeelte van de experimenten bestond voornamelijk uit lasers. Anton en Ad maakten en hielden deze lasers werkend. Bedankt voor jullie inzet.
E&I en de werkplaats bedankt voor jullie bijdrage aan dit proefschrift.
Tijdens mijn promotie heb ik de kamer gedeeld met Andreas en Afric. Naast wetenschappelijke discussies werd over van alles en nog wat gediscussieerd en gelachen. De sfeer op de kamer was dan ook altijd erg gezellig. Na werktijd werd nog wel eens verder gepraat tijdens een etentje onder het genot van een door Hinco verzorgd wijntje.

Het grootste gedeelte van mijn promotie heb ik deel uitgemaakt van de Atmosferische fotofysica groep. De sfeer binnen de groep was altijd erg vriendelijk en behulpzaam. Tijdens de koffie- en lunchpauzes werd dan ook heel wat afgelachen samen met Annemieke, Ben, Hester, Jason, Laura en Rüdiger.
Tijdens het begin van mijn promotie maakte ik deel uit van de voormalige femtofysica groep. De oud-leden Chris, Marcel en Kees waren altijd bereid om te helpen.
Met veel plezier heb ik samen met de andere pv-bestuursleden altijd graag activiteiten op Amolf georganiseerd. De pv-activiteiten waren een goede gelegenheid om de andere ‘amolfers’ te leren kennen.
Mijn paranimfen, Sietske en Elena, bedankt voor jullie steun en betrokkenheid tijdens mijn promotie. Jullie waren altijd op de hoogte van alle ups en downs en volgden alles op de voet. Met Sietske werden alle details besproken tijdens een partijtje squash met aansluitend een etentje. Bij Elena kon ik altijd terecht voor een korte theepauze.
Naast mijn promotie zorgden mijn vrienden voor de nodige afwisseling, bedankt.
Mijn ouders bedankt voor jullie interesse en pogingen om enigszins te volgen wat ik allemaal daar in Amsterdam deed.
Tenslotte stond iemand dagelijks klaar om mijn hele werkdag aan te horen, mij te blijven steunen en aan te moedigen, Pascal bedankt.

Anouk Wetzels, mei 2003

Curriculum Vitae

The author of this thesis was born on October 20, 1975, in Sittard, The Netherlands. From 1988 to 1994 she studied at the Gymnasium of the College of Sittard. In 1994, she started studying chemistry at the University of Utrecht. During this period she worked for three months at Philips Research. She performed her undergraduate project at the FOM Institute for Atomic and Molecular Physics in the group of Prof. dr. L.D. Noordam. From 1998 till 2003, she did her Ph.D. at the FOM Institute for Atomic and Molecular Physics, in the groups of Prof. L.D. Noordam and Prof. dr. W.J. van der Zande. The work performed during the Ph.D. period is the subject of this thesis.